SAPIENZA
UNIVERSITÀ DI ROMA

# Production of positrons for a muon collider

**Facoltà di Scienze Matematiche Fisiche e Naturali**
**Corso di laurea in Fisica**
Candidato
Andrea Allegrucci
n° matricola 1654402

Relatore
Prof. Gianluca Cavoto
Dott. Francesco Collamati

A/A 2018/2019

# Contents

# Introduction

In this work, the hypothesis of a positron based muon collider will be considered.

The realization of a muon collider could be a great opportunity for enlarging particle physics boundaries, as will be presented in Chapter 1. The advantages of a positron based scheme, as well as the technical and physical limitations, will be also presented.

This scheme is now under proof of concept by the LEMMA group (Low EMittance Muon Accelerator). According to this scheme, an intense positron beam of 45 GeV or more will be used to impinge on a target and produce muons by positron annihilation on an electron target. Possible schemes of the accelerator complex and details on muon production are described in Chapter 2.

In an accelerator facility, the beam has to be continuously regenerated to compensate for the losses on the targets, in order to maintain a high luminosity (the number of collisions per unit time and surface), so a high rate of interesting events.

The main goal of this work is to consider the possibility of an embedded source of positrons to obtain this compensation. As will be presented in Chapter 3, this source can be obtained by exploiting the high number of gamma rays produced by the positrons in the muon target (or targets) for electromagnetic interaction with the nuclei or the electrons of the medium. These photons can then be used to produce new positrons in a second target or regenerator, by pair production. Otherwise, the positron beam itself can be used, and new positrons can be obtained by the electromagnetic shower that the beam produces in the regenerator.

These solutions have been implemented in a Geant4 simulation code, and the results of these study, which could be a reference for new studies and experiments, will be discussed in Chapter 3.

Finally, in Chapter 4, results of the introduction of an AMD (Adiabatic Matching Device) in the simulation as a positrons capture system will be presented.

# Chapter 1

# A Muon Collider

The search for new particles and their physical interactions requires always more energy, in order to produce high-$Q^2$ events and to investigate the infinitely small components of the universe with a better and better resolution. In order to explain this, let's consider the interactions $e^-p$ (fixed-target) or $e^+e^-$ (head-on collision), shown Figure 1.1(a)). By measuring the properties of the initial and final state particles, one can evaluate the four-momentum transfer $Q^2$, which is the four-momentum of the particle that describes the interaction (a virtual photon in the example). It represents both the energy and the momentum transferred to the final state particles. The quantity:

$$\lambda = \frac{1}{\sqrt{Q^2}} \tag{1.1}$$

has the unit of a length ($\hbar c = 1 \simeq 200$ MeVfm) which represents the resolution power of the probe (a virtual photon in this case). For instance, in order to probe the nucleus with $\lambda = 1\,\mathrm{fm}$, it must be $Q \sim 200\,\mathrm{MeV}$. Hence, in order to increase the spatial resolution, larger values of $Q^2$, which is proportional to the beam energy, are needed.

The main advantage of a muon collider is that muons are, as far as we know, point-like particles, as electrons, but about 200 times heavier.

Since are point-like, the energy of the muon is not distributed to further point-like components, as it happens for protons. Protons' parton distribution functions describe, at least at high energy, the fraction of proton momentum $x$ carried by each parton inside the proton as a random variable. At TeV energies, which is the present limit for proton circular colliders, the fraction $x$ of valence quarks is about 1/6 in average (see Figure 1.1(b)), so only a little fraction of energy used for accelerating protons is available for point-like interactions.

So a huge fraction of proton energy, obtained by an expensive chain of accelerators, is essentially lost in accelerating its center of mass, distributed in many partons, and this limits the possibilities of discovery of the machine, ever more while increasing energy.

Lepton colliders, in this view, are intrinsically more efficient for high energy physics, since the interactions are between two bunches of particles per time, and not two bunches of many partons. Thanks to this, cleaner events are produced, and this is also important for background control during event analysis. However, hadron colliders, thanks to proton's composition, can produce a richer variety of interactions, at different energies at the same time, and this can result in a richer physics.

Cleaner events produce also more interesting challenges in the comparison between theory and

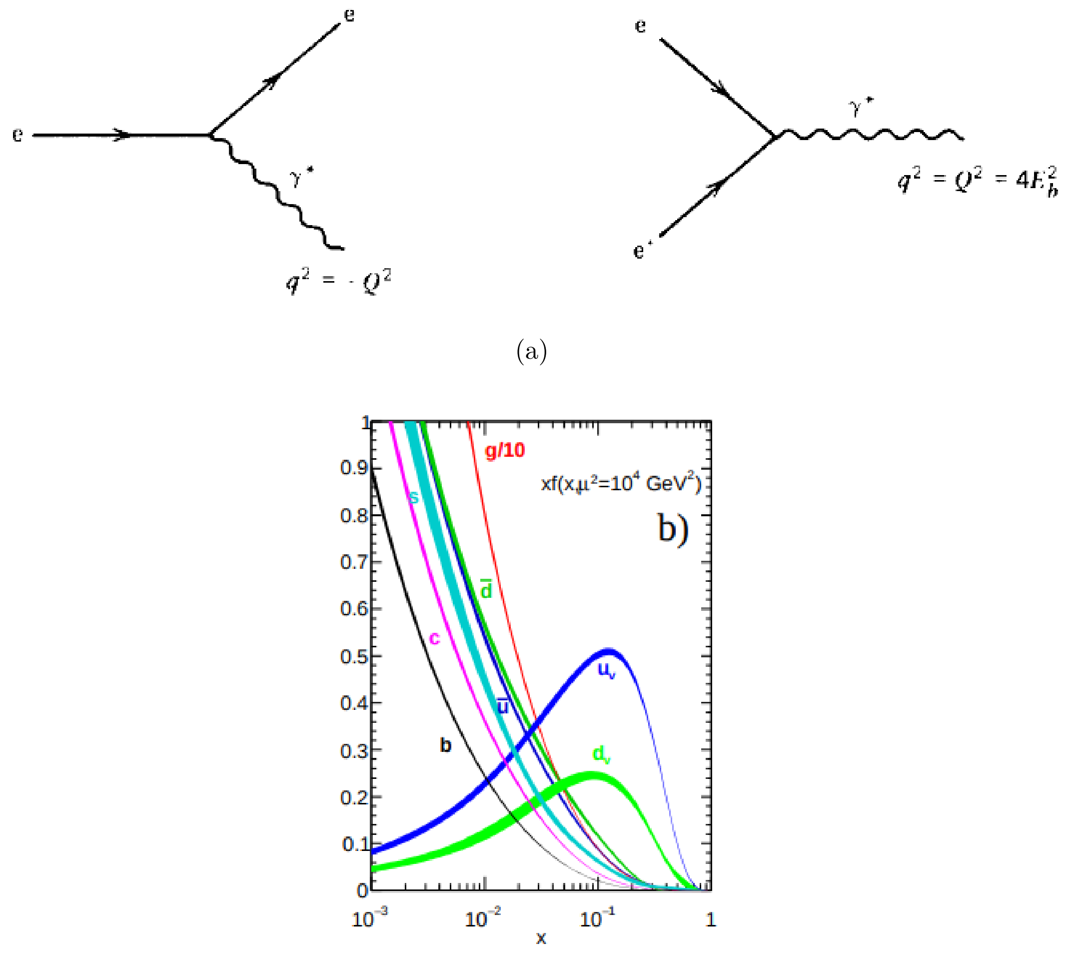

(a)

(b)

**Figure 1.1:** (a) Virtual photon probes in deep inelastic scattering $e^-p$ (left), and $e^+e^-$ head-on collisions with beam energy $E_h$ (right). (b) $f(x)$ parton distribution functions for different partons inside the proton, at a scale $Q^2 \sim 10$ TeV$^2$.

experiments, since low background means also more accuracy, and thus test of the Standard Model theory with a better precision and better measurements of physical quantities. This could allow an indirect search for new physics.

Another advantage of a muon collider, with respect to an $e^+e^-$ collider, is about synchrotron radiation. The main limitation of a circular collider is the synchrotron radiation emitted by the accelerated charged particles. Synchrotron radiation prevents to reach higher energy when the total amount of energy lost in one turn is greater or equal to the energy given by the machine for the acceleration. The fraction of energy lost by a particle in one turn at light speed is proportional to $1/M^4$, where $M$ is the mass of the particle (see (1.11) ), so it is very high for electrons and positrons, but for muons, due to the larger mass, is about a factor $2 \cdot 10^9$ lower at the same energy.

From a technical point of view, the main challenge for the realization of a muon collider is the muon decay with a lifetime of $2.2\,\mu$s [1]. It is not so easy to have a large number of muons ready to be accelerated, as will be clear in a while, and the decay limits even more the luminosity. Moreover, the muon decay background gives also a problem both for the machine and the detectors, since electrons interacting with the beamline components will produce electromagnetic showers. As a result, a large number of low-energy photons and soft neutrons may reach the accelerator elements and the detectors. Large heat deposition from the showers induced by decay electrons requires the use of large-aperture magnets to accommodate the thick high-Z absorbers needed to protect the superconducting coils. Radiation protection systems to shield the magnets apertures and interconnections by radiation damage must be designed [1].

However, at least in principle, this could be also an advantage, since electron and neutrinos are produced with a well known flux and energy spectrum. These neutrinos could serve as the source for a Neutrino Factory, which would constitute the ideal complement to Long Base Line Facilities, as for the DUNE or T2K experiments.

## 1.1 Physics at muon collider

The potentialities of muon colliders can be compared to those of proton colliders, since the achievable energy is similar (tens of TeV).

One of the main consequences of the fact that muons are point-like particles is that processes of a fixed cross section can be achieved at a much smaller center of mass energy.

Let us consider the production of a resonance with mass $M$, at threshold energy, so that $\sqrt{\hat{s}} \simeq M$. $s$ is the *center of mass energy* and is defined as $s = \underline{p}_{\text{tot}}^2$, where $\underline{p}_{\text{tot}}$ is the sum of all four momenta in the initial state. $\hat{s}$ is the same variable considering only point like components, so it is different from $s$ in proton-proton collisions.

In a muon collider, the total cross section $\sigma_\mu$ is equal to the cross section for point-like components $\hat{\sigma}_\mu$ and they scale as $1/s$ [2]. So, once the cross section $\hat{\sigma}$ of a given process at $\hat{s}$ is measured, the cross section $\sigma_\mu$ at any $s_\mu$ can be obtained by simply scaling for the $1/s$ factor:

$$\sigma_\mu(s_\mu) = \frac{1}{s_\mu}[\hat{s}\hat{\sigma}]_\mu. \tag{1.2}$$

The $1/s$ scaling can be explained by the fact that the transverse cross section is a relativistic invariant quantity, measured in $\mathrm{E}^{-2}$ units, and $s$ is the only relativistic invariant quantity available if all masses are neglected and no resonance of high mass is considered.

In a proton collider, since the real colliding objects are partons, the factorization has to be invoked:

$$\sigma_p = \sum_{i,j} \int_0^1 dx_1 dx_2 f_i(x_1, \sqrt{\hat{s}}) f_j(x_2, \sqrt{\hat{s}}) \hat{\sigma}_{ij}, \tag{1.3}$$

where $x$ is the Feynmann variable of the quark parton model, that is the fraction of longitudinal proton momentum carried by the parton, $f$ is the parton distribution function (pdf) at a given $x, \sqrt{\hat{s}}$ and $\hat{\sigma}$ the cross section at parton level. The *differential parton-parton luminosity* [3] is:

$$\frac{dL_{ij}}{d\hat{s}dy} = \frac{1}{s}\frac{1}{1+\delta_{ij}}[f_i(x_1, \sqrt{\hat{s}}) f_j(x_2, \sqrt{\hat{s}}) + (1 \leftrightarrow 2)], \tag{1.4}$$

where $y$ is the rapidity. The *rapidity* represents the velocity of the center of mass at parton level along $z$. It is defined for the interaction of two partons as $y = \frac{1}{2}\log\frac{E+p_z}{E-p_z}$, where $E$ and $p_z$ are the sum of energy and momentum of the two parton, with four momentum $\underline{p_1} = \frac{\sqrt{s}}{2}x_1(1,0,0,1)$ and the same for the second parton in the opposite direction.

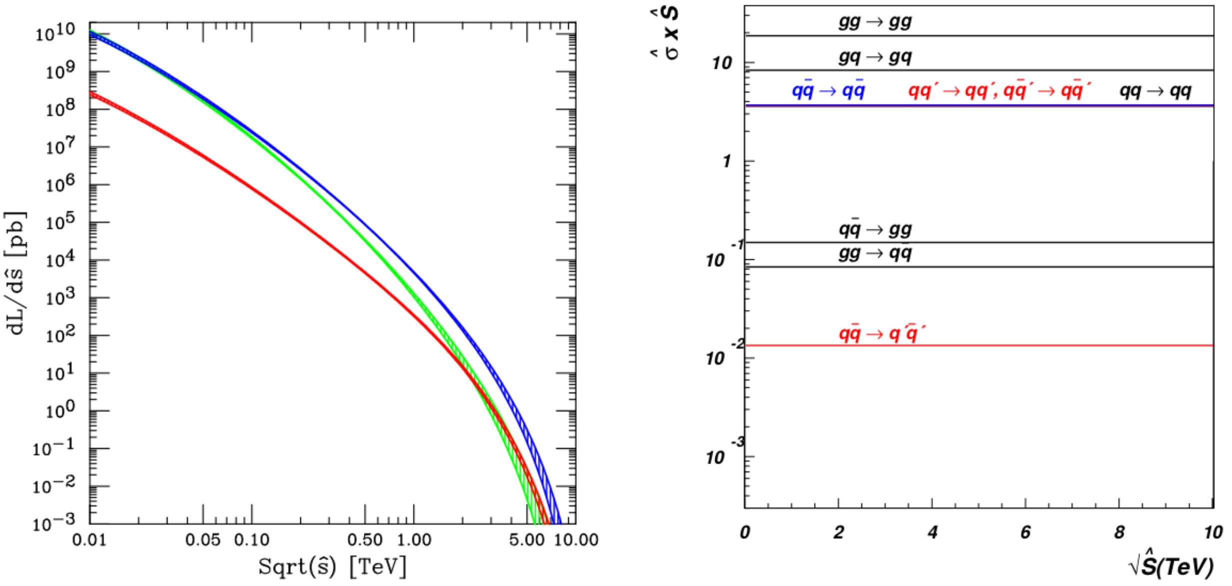

(a) (b)

**Figure 1.2:** (a) The parton-parton luminosity in pb, integrated over rapidity y. Green=$gg$, Blue = $\sum_i(gq_i + g\bar{q}_i + q_i g + \bar{q}_i g)$, Red = $\sum_i(q_i\bar{q}_i + \bar{q}_i q_i)$, where the sum runs over $d$, $u$, $s$, $c$, $b$. (b)Parton level cross sections ($\hat{s}\hat{\sigma}_{ij}$ ) for various processes involving massless partons in the final state.

By considering the integral over rapidity of the parton-parton luminosity, $\frac{dL_{ij}}{d\hat{s}}$, the (1.3) can be rewritten as:

$$\sigma = \sum_{i,j} \int \frac{d\hat{s}}{\hat{s}} dy \frac{dL_{ij}}{d\hat{s}dy} [\hat{s}\hat{\sigma}_{ij}] \,. \tag{1.5}$$

By introducing $\tau = x_1 x_2 = \frac{\hat{s}}{s}$, the cross-section for a proton collider is:

$$\sigma_p(E, s_p) = \frac{1}{s_p} \int_{E^2/s_p}^{1} \frac{d\tau}{\tau} \frac{dL}{d\tau} [\hat{s}\hat{\sigma}]_p \tag{1.6}$$

In Figure 1.2(a) the parton-parton luminosity for different partons is shown. It is decreasing with $\sqrt{\hat{s}}$, so the total cross section does not scale as 1/s, but decreases more quickly. We used the fact that, as one can see in Figure 1.2(b), the product $\hat{\sigma}\hat{s}$ is almost independent from $\sqrt{\hat{s}}$ (1).

As a consequence, equal muon and proton collider cross-sections are obtained for $\sqrt{s_\mu} \ll \sqrt{s_p}$, as presented in Figure 1.3. Hence, a 14 TeV muon collider with sufficient luminosity, can have a potential and a physics motivation similar to that of a 100 TeV proton collider.

In Figure 1.4 the cross sections of some Beyond Standard Model (BSM) processes with heavy particles and Standard Model (SM) processes at high energy are reported.

Discoveries by direct exploration can be achieved, for instance, thanks to the very large vector-boson fusion (VBF) cross section. New particles coupled with the Higgs boson can be searched in this way.

For instance with an integrated luminosity of 10 ab$^{-1}$, a 10 TeV muon collider would produce 8 million Higgs bosons.

---

(1) Even if for final states involving massive particles a threshold behaviour is present, see [3].

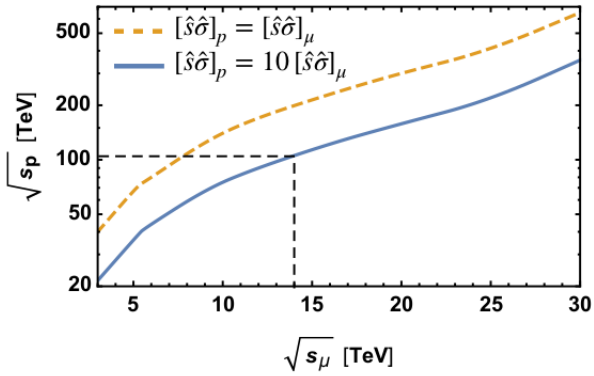

**Figure 1.3:** The energy at which the proton collider cross-section equals that of a muon collider. The dashed line assumes comparable Feynman amplitudes, while the continuous line considers a factor ten enhancement of proton production cross section, possibly due to strong interaction enhancement with respect to electroweak interaction.

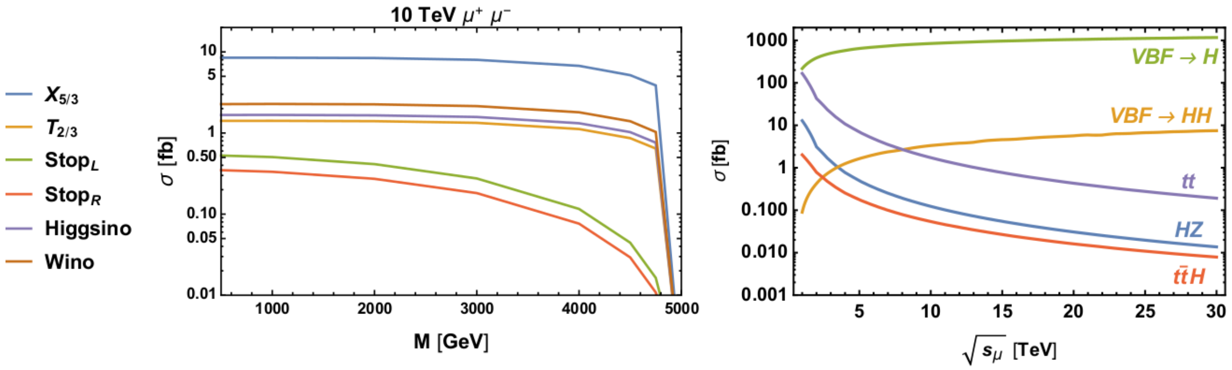

**Figure 1.4:** Left panel: cross sections for the production of some supersymmetric particles for a 10 TeV muon collider. The lines represents the production cross sections of hypothetical particles, predicted by different theoretical models, not yet confirmed or rejected. Right panel: cross sections of some processes at high energy in a muon collider.

By performing precision measurements, thanks to relatively low background with respect to hadron colliders, it is also possible to probe New Physics indirectly, by means of comparison of the theory with radiative corrections.

Since it is not clear what to look for, and at which energy, a simple, non-exhaustive estimation of the minimal useful luminosity of such a collider can be obtained by electroweak interactions as $\mu^+\mu^- \to \gamma^* \to e^+e^-$ process (with no mass dependence). The cross section is:

$$\sigma \sim \frac{4\pi}{3}\frac{\alpha^2}{s}, \tag{1.7}$$

where $\alpha$ is the electromagnetic constant. So at 10 TeV the cross section is of the order of 1 fb. Whit an instantaneous luminosity of $10^{34}$ cm$^{-2}$s$^{-1}$, the total number of events with a 5 years run (assuming $1\text{ y} = 10^7$ s) is 500:

$$N = \frac{\text{time}}{5\text{ years}}\left(\frac{10\text{ TeV}}{\sqrt{s_\mu}}\right)^2 \frac{\text{luminosity}}{10^{34}\text{cm}^{-2}\text{s}^{-1}} \cdot 500. \tag{1.8}$$

The (1.8) gives the luminosity that must be reach in order to have a significant number of events at a given center of mass energy for a muon collider. For instance, in order to discover new particles with easily identifiable decay products, such as Stops and Top Partners, 100 events might be sufficient [1]. Then, assuming 5 years of operation at 10 TeV, the luminosity must be greater than $2 \cdot 10^{33}\text{cm}^{-2}\text{s}^{-1}$.

## 1.2 Basics of colliders and beam dynamics

### 1.2.1 Luminosity

Luminosity is one of the most important parameters in accelerator physics, as it represents the total number of collisions, per unit time and per unit cross section, that occurs between the two interacting beams, in the case of colliders, or between the beam and the target, in the case of fixed target experiments.

So, when a physical process is given, characterized by its cross section $\sigma$, the rate of events of such a process is given by:

$$\frac{d\mathcal{N}}{dt} = \mathcal{L} \cdot \sigma \tag{1.9}$$

where $\mathcal{L}$ is the instantaneous luminosity, expressed in $[\text{cm}^{-2}\text{s}^{-1}]$.

A basic expression of luminosity can be given in terms of emittances $\epsilon$ and amplitude functions (or beta functions) at collision points, $\beta^*$, as

$$\mathcal{L} = f n_b \frac{N_1 N_2}{4\pi\sqrt{\epsilon_x \beta_x^* \epsilon_y \beta_y^*}} F \tag{1.10}$$

where $f$ is the revolution frequency, $n_b$ the number of bunches, $N_1$ and $N_2$ the number of particles inside the bunches, respectively in the first and in the second beam. A *bunch* is a moving region of space in which particles are stored together when injected in an accelerator. In general the number of particles that can be stored in a bunch is around $10^{11}$. Typically, they are described by a distribution with a Gaussian profile, so that $2\sigma$ contains 68% of particles (both longitudinally and laterally). $F$ is a factor lower than one, that takes into account effects that reduce luminosity (such as crossing angle of the beams and beam-beam interactions). The *crossing-angle* effect is due to the fact that, in order to reduce the pile-up (too many events in the same period of time), the beams are inclined by an angle before the interaction region, but this reduces the number of collisions.

Then there are time effects (particles that interacts are lost, hence the luminosity goes down until the collider is re-filled with new bunches) and pinches (particular points in the accelerator where particles impinge on the tube and are lost). The *emittance* $\epsilon$ and the *beta function* $\beta$ can be related to the accelerator optics and will be defined later in Section 1.2.3.

So, in order to achieve high luminosity, one has to make high population bunches of low emittance collide at high frequency at locations where the accelerator optics provides as low values of the amplitude functions as possible.

### 1.2.2 Synchrotron radiation

One of the main limitation in both luminosity and maximal energy in electron or positron colliders is given by synchrotron radiation. These losses must be compensated by Radio Frequency

(RF) power, however the population of bunches, to which luminosity is proportional, must be limited because high power and beam currents are technical limits.

The energy loss per turn, per electron (or positron) is [4]:

$$U\,[\text{GeV}] = \frac{1}{3\epsilon_0}\frac{e^2E^4}{M^4R} = C_\gamma\frac{E^4}{R}, \tag{1.11}$$

where $\epsilon_0$ is the vacuum permittivity, $e$ is the electron charge, $E$ the beam energy, $M$ the mass of the beam particles and $R$ the radius of the collider. For electrons $C_\gamma = 0.8846 \cdot 10^{-4}$ m/GeV$^3$, while for protons $C_\gamma = 0.7783 \cdot 10^{-17}$ m/GeV$^3$. For muons it can be obtained by $C_\gamma(\mu) = C_\gamma(e)(m_e/m_\mu)^4 = 0.485 \cdot 10^{-13}$. $C_\gamma$ is known as the "Sands constant".

Corresponding to energy loss $U$, the radiated power from the beam having $n_b$ bunches of $N_p$ particles, in GW units, is given by:

$$P_{\text{rad}} = Un_bN_pfe \tag{1.12}$$

where $f$ is the revolution frequency ($f = \frac{c}{2\pi R}$ for particles travelling at light speed) and $e$ the electron charge in Coulomb.

The spectrum of radiated photons is characterized by a "critical energy" $u_c$, defined starting from the classical *critical frequency* $\omega_c$, which is the frequency after which the radiation is negligible at all angles [5], given by:

$$u_c\,[\text{GeV}] = \hbar\omega_c = 10^{-9}\frac{3}{4\pi}hc\frac{\gamma^3}{R} = 2.96 \cdot 10^{-16}\,\text{GeV}\,\text{m}\,\frac{\gamma^3}{R[\text{m}]} \tag{1.13}$$

For radiated photons of energy $u$, the average energy value is related to the critical energy by:

$$< u >= 0.31u_c \tag{1.14}$$

The total number of particles in the beam, $N_{\text{tot}} = n_bN_p$ is finally limited by the relation:

$$P_{\text{rad}} = P_{\text{rf}} \rightarrow fN_{\text{tot}}eU\,[\text{MeV}] = I[\text{A}]V[\text{MV}] = P_{\text{rf}}[\text{MW}] \tag{1.15}$$

and hence, once the energy and the radius of the ring are fixed, by the RF power.

For instance, in the Large Hadron Collider (LHC) ring at full power, $I = 0.58\,\text{A}$ and there are 8 RF cavities of 2 MV per beam, hence $P_{\text{rf}} = 9.3$ MW. The number of protons stored in each bunch is $N_p = 1.15 \cdot 10^{11}$ p/bunch and there are 2808 bunches per ring. Hence, $P_{\text{rad}} \simeq 2.5$ kW. Since $P_{\text{rad}} \ll P_{\text{rf}}$, LHC is not limited by synchrotron radiation (2).

This argument gives the second reason to make rings with large $R$ (the first one is to reach higher energies, see (1.22)), that is to reach higher luminosities. In fact, once the RF power is limited by technical issues, in order to increase $N_{\text{tot}}$ (and hence luminosity) at fixed energy the ring radius must be increased.

### 1.2.3 Basic principles of beam dynamics

To discuss the basic principles of beam dynamics, a synchrotron machine will be considered, as its dynamics can be described by assuming a linear approximation [7]. A synchrotron machine,

---

(2) Notice that $N_{\text{tot}}$ cannot be further increased for practical reasons.

shown in Figure 1.5, is a circular, ring-shaped machine, characterized by a constant radius. The charged particles move in a doughnut-shaped evacuated channel. A proper magnetic field, applied by dipole magnets, is needed to maintain the ions in an orbit of the proper radius. In this approximation the machine is composed only by dipoles, quadruples, used to focus the beam and limit the beam divergence, and Radio Frequency (RF) cavities. The accelerating electric field is sinusoidal ($\mathbf{E} = \mathbf{E}_0 e^{i\omega t}$) and is provided by the RFs of the proper frequency, typically $\sim 10-100\,\text{MHz}$ (400 MHz for LHC). This is the frequency at which the voltage inside the RF cavity oscillates, and it must be reasonably greater than the revolution frequency, in order to accelerate several bunches of particle in the same turn, and an integer multiple of it, in order to make sure that the particles always see an accelerating voltage at the gap.

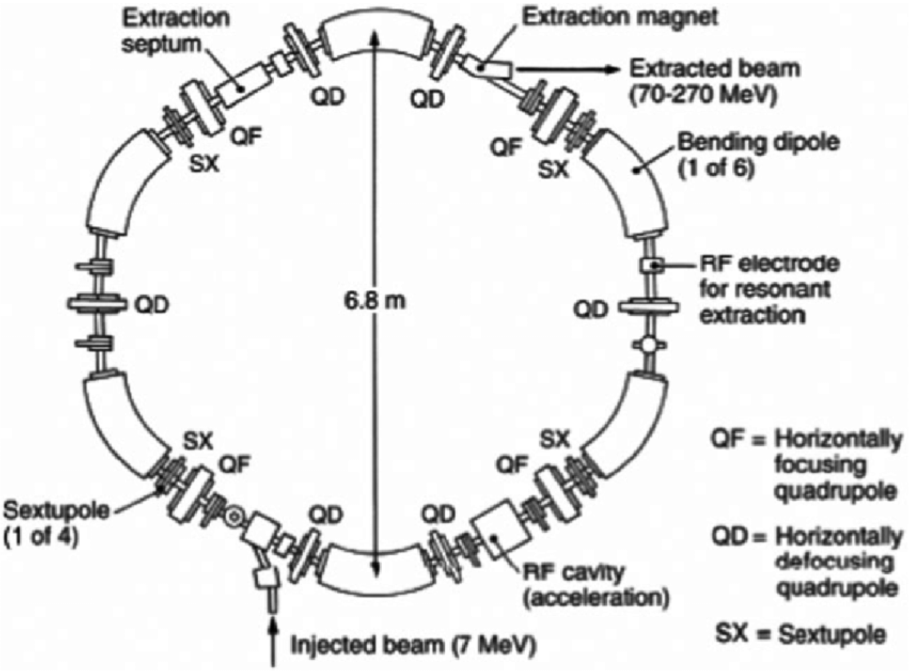

**Figure 1.5:** Schematic diagram of HITACHI 250 MeV proton synchrotron. It consists of one RF cavity for acceleration and six bending dipole magnets to drive the particle in circular orbit. Quadruple magnets are used for focusing.

For electrons, which are extremely relativistic, the acceleration is provided by slowly increasing the magnetic field, keeping the frequency of the electric field constant. For protons or muons, which are not as light, it is necessary to increase the frequency as the magnetic field increases, as they do not travel immediately at light speed [8].

Two important issues to maintain all particles in the correct orbit are the principle of *phase stability* and *strong focusing* techniques.

In any accelerator operating on the multiple-acceleration principle, it is essential that the successive impulses be imparted at the proper time, otherwise the circulating particles are rapidly lost. There is a mechanism that makes it possible. With suitable arrangements of fields the particles tend automatically to cross the accelerating gap at a proper time, in which they receive the amount of energy necessary to keep them in resonance with the electric field. This is the principle of phase stability [8].

To understand the phenomenon, let us consider first a particle circulating in an orbit through a spatially constant magnetic field and passing a gap with an applied alternating electric field.

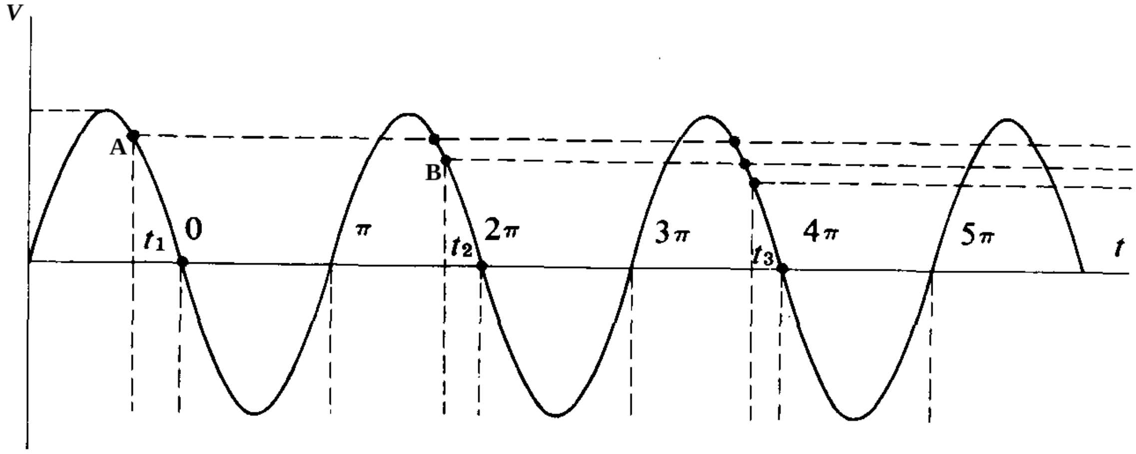

**Figure 1.6:** Variation of accelerating potential with time, showing the origin of phase oscillation.

The so called *synchronous particle* is the one with velocity such as to cross the gap when the electric field is 0 (we assume to neglect radiation and other losses). The particle will circulate indefinitely in this orbit, at a constant velocity. Also the energy $E$, the momentum $p$, the angular velocity $\omega$ and the radius of the orbit $r$ are denoted by the adjective *synchronous*. Moreover, the synchronous particle is the one that moves with frequency $\omega_s$ equal to the frequency of the resonant cavity. So, it is not accelerated nor decelerated.

To illustrate the principle, let us consider Figure 1.6.

If another particle arrives at the gap a little earlier than a synchronous particle, for instance in the point **A** at time $t_1$, it will be accelerated by the positive voltage, hence it will gain energy. Since in a circular motion, due to a bending magnetic field $B$, the frequency of the orbit is linked to the energy $E$ by

$$\omega = \frac{eBc}{E}, \tag{1.16}$$

the frequency of the particle will be decreased. Hence, its period will be elongated, and at the next crossing it will be in the point **B** with $V_{\mathbf{B}} < V_{\mathbf{A}}$, and so on. The particle will receive a lower acceleration, and this process continues until the gap is crossed at the time when there is no electric field. On the contrary, if the particle crosses the cavity when the voltage is negative, its energy decreases and the frequency increases.

A particle thus performs oscillations in the longitudinal direction with respect to a synchronous particle. The consequence is that it is not necessary to adjust all parameters in strict synchronism (which is a practically impossible task) for any particle, but that the motion itself takes care of keeping the particle in phase. This is the phase stability concept.

Also by slowly increasing $B$ or decreasing $\omega$ we cause the synchronous energy $E_s$ to increase (by 1.16), and hence the particles that are locked in the synchronous orbit are accelerated.

More quantitatively, let us consider the RF potential difference at a gap

$$\Delta V = V \sin \omega_s t, \tag{1.17}$$

where $V$ is the maximum value of the RF potential and $\omega_s$ the frequency of the resonant cavity. Then, let us define the *phase* $\phi$ of a particle as the angle

$$\phi = \theta - \omega_s t, \tag{1.18}$$

where $\theta = \omega t$ is the angular position of the particle in the ring. $\omega = 2\pi/T$ is the instantaneous angular velocity of the particle.

If it remains $\omega = \omega_s$, the phase is constant and the particle is synchronous. Its energy, after a gap crossing, will increase by

$$\Delta E = eV \sin\phi(t). \tag{1.19}$$

This equation shows the importance of the phase concept: the phase determines the increase of energy per revolution. For a synchronous particle, having $\phi = 0, \pi$, $\Delta E = 0$.

It can be proved that, for a particle having the parameters $r$, $p$, $\omega$, etc., near synchronism, the phase oscillates around a fixed value $\phi_s$, that is the phase of the particle that moves along the ideal orbit, the synchronous particle [8].

It can be showed that similar oscillations, called betatron oscillations, happen also in vertical and radial directions when some conditions in the magnetic optics are satisfied. In particular, this happens when the field index $n$, used to describe the $z$ component of the magnetic field as $B_z = B(r/R)^{-n}$, satisfies the condition $0 < n < 1$ [3] [8]. These oscillations are harmonic, in first approximation. Thus a group of particles forms a "bunch" in the orbit, and each particle migrates back and forth within the bunch.

Only particles with small deviation from reference momentum could be stable in the synchrotron motion. In the phase space $(E, \phi)$ a stable and an unstable region can be identified, as shown in Figure 1.7(a). The limit of the stable region is called *separatrix*, which is defined by the full width at half maximum of the RF bucket.

This definition fixes the energy acceptance of the machine as:

$$\Delta E_{\max} = k\sqrt{2\cos\phi_s + (2\phi_s - \pi)\sin\phi_s} \tag{1.20}$$

where $\phi_s$ is the phase of the synchronous particle, and $k = \beta_s\sqrt{\frac{eVE_s}{\pi h \eta}}$ is a constant, where $h = f_{\mathrm{RF}}/f$, $\eta = \frac{p_s}{\omega_s}\left(\frac{d\omega}{dp}\right)_s$ and $\beta_s$ the velocity of the synchronous particle [9]. The energy acceptance is largest for $\phi_s = 0, \pi$. Outside the separatrix, particles can lose energy at every passage through the RF, and get lost uncontrolled around the machine.

*Strong focusing* is used to keep the amplitudes of the radial and vertical oscillations small, in order to minimize the number of particles that strike the wall of the accelerator ring and are hence lost. Moreover, by keeping the cross section of the tank small, the size and the required power for the magnets are smaller.

This requirement can be achieved by keeping the oscillation frequencies high. In fact, if at injection the ions start with $z = 0$, $\dot{z}(0)$ different from 0, the maximum amplitude is $z_{\max} = \frac{\dot{z}(0)}{\omega_z}$. Now, according to betatron oscillations, obtained by resolving the equation of motion of a relativistic particle in a field $B_z = B(r/R)^{-n}$, the oscillation frequency is $\omega_z = \omega_s n^{1/2}$, hence a large $n$ is required. This is, however, a problem, since $0 < n < 1$ is required for radial stability.

The solution has been found in the use of successive magnet segments having, alternately, $n$ large and positive and $n$ large and negative. The first one focuses vertically but defocuses horizontally. The opposite happens with the second segment. The somehow unexpected experimental fact is that the total effect is focusing in both directions, and the radial excursions

---

[3] Such that the frequencies obtained as solution for the motion, $\omega_z = \omega_s n^{1/2}$ and $\omega_{\mathrm{radial}} = \omega_s(1-n)^{1/2}$, where $\omega_s$ is the frequency of the ideal particle, are both defined.

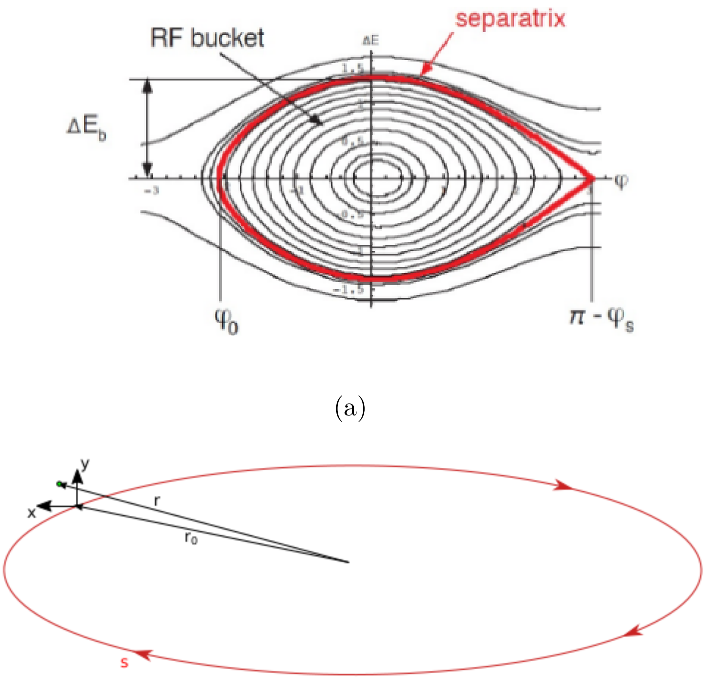

(a)

(b)

**Figure 1.7:** (a) Longitudinal motion in Energy-Phase Advance phase space. The limit of stable motion, the separatrix, is shown in red. (b)Frenet-Serret reference system.

due to momentum differences are reduced. This is the strong focusing or alternating-gradient effect [8].

### 1.2.4 The equation of motion in the transverse plane

In an accelerator, a particle is subjected to the Lorentz Force and the equation of motion is:

$$\mathbf{F} = q(\mathbf{E} + \mathbf{v} \times \mathbf{B}) = \frac{d\mathbf{p}}{dt} = \frac{d}{dt} m\gamma\mathbf{v} \tag{1.21}$$

If projected in the radial direction, assuming the magnetic field along $\hat{y}$ and the velocity along $\hat{s}$, it becomes:

$$qvB_y\hat{r} = p\omega\hat{r} = p\frac{v}{R}\hat{r} \rightarrow p = qRB_y \tag{1.22}$$

This equation describes the relationship between the beam energy and the required magnetic field for all accelerators. Once the radius $R$ is fixed, the magnetic field has to be increased in order to increase the beam energy.

In general,

$$p_\perp[\text{MeV}] = 300B[\text{T}]R[\text{m}], \tag{1.23}$$

where $p_\perp$ is the transverse momentum with respect to the magnetic field direction.

In a circular collider, it is useful to define the Frenet-Serret reference system. The closed orbit of a reference particle is defined as the curvilinear abscissa ($\hat{s}$), and the distance from the orbit is defined in the transverse plane ($\hat{x}, \hat{y}$) as shown in Figure 1.7(b).

Hence, the variables $x$ and $y$ represent the horizontal and vertical displacements of a particle with respect to the ideal orbit of radius $\rho$. In an ideal circular orbit the radius has to remain constant, but we consider $\rho = \rho(s)$. The total horizontal distance of a particle with respect to the centre is then $r(s) = \rho(s) + x(s)$ with $x \ll s$.

Since this reference system is rotating, particles are subjected also to a centrifugal force $F_c = -m\frac{v^2}{r}$ in the horizontal direction. The equations of motion are then:

$$\begin{aligned} m\frac{d^2x}{dt^2} - \frac{mv^2}{\rho}\left(1 - \frac{x}{\rho}\right) &= qvB_y \\ m\frac{d^2y}{dt^2} &= -qvB_x \end{aligned} \tag{1.24}$$

For small variations in the transverse plane, the magnetic field can be expanded as:

$$\begin{aligned} B_x &= \frac{\partial B_x}{\partial y}y \\ B_y &= -B_y^0 + \frac{\partial B_y}{\partial x}x \end{aligned} \tag{1.25}$$

where the coefficient at zero order is the dipolar term, and the coefficient at first order is the quadrupolar term. Since no currents are involved in the vacuum of the doughnut, $\nabla \times \mathbf{B} = 0$ and $\frac{\partial B_y}{\partial x} = -\frac{\partial B_x}{\partial y} \equiv B_1$.

Passing now from $t$ to $s$ as independent variable and defining $k(s) \equiv \frac{B_1}{B_y^0 \rho}$, the final result is:

$$\begin{aligned} x''(s) + x(s)\left(\frac{1}{\rho^2(s)} - k(s)\right) &= 0 \\ y''(s) + k(s)y(s) &= 0\,. \end{aligned} \tag{1.26}$$

This set of equations is known as Hill equations, and they are defined pseudo-harmonic because of the dependence of $k$ (the elastic constant) from $s$. Their solution, equal for both $x$ and $y$, is:

$$x(s) = A\sqrt{\beta_x(s)}\sin(\phi_x(s) + \phi_0) \tag{1.27}$$

where $\beta$ is an amplitude modulator.

By substituting the solution (with $\beta$ and $\phi$ depending on $s$) in the second order equation, it can be shown that the phase advance is related to $\beta$ by [10]:

$$\phi(s) = \int_0^s \frac{ds'}{\beta(s')} \tag{1.28}$$

In the case of a standard oscillation, $\phi(s) = \omega t = \omega s/v$, hence:

$$\frac{d\phi}{ds} = \frac{1}{\beta(s)} = \frac{\omega}{v} \tag{1.29}$$

which is constant. Therefore, this definition makes $\beta(s)$, the *beta function*, interpretable as the local (spatial) amplitude of the betatron oscillation.

In this case, $x'(s) = \frac{dx}{ds}$, which represents the transversal variation of the beam along the orbit, is:

$$x'(s) = \frac{A}{\sqrt{\beta}}\cos(\phi_x(s) + \phi_0) \tag{1.30}$$

and, in general, $\beta$ can be defined as $\beta_x = \frac{\sigma_x}{\sigma_{x'}}$, where $\sigma_x = A\sqrt{\beta}$ is called beam size and $\sigma_{x'} = \frac{A}{\sqrt{\beta}}$ the beam divergence.

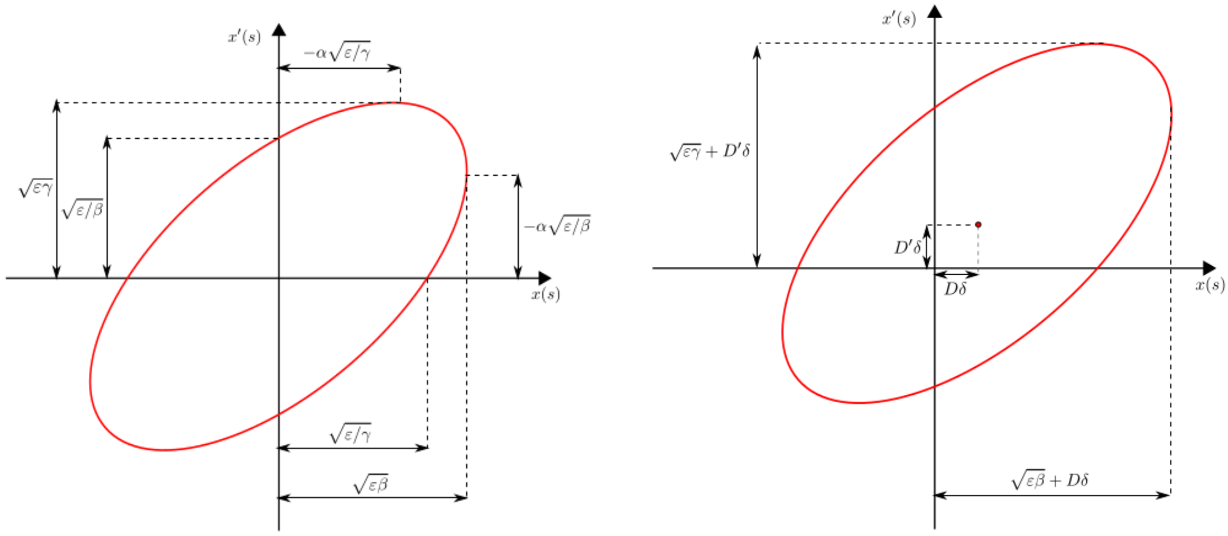

(a) (b)

**Figure 1.8:** (a)Phase space of transverse betatron oscillation. The relations with the emittance and the beta function are shown. (b)Phase space of transverse betatron oscillation for a particle with momentum offset $\delta$.

Now it is possible to introduce two quantities:

$$\begin{aligned} \alpha(s) &= -\frac{\beta'(s)}{2} \\ \gamma(s) &= \frac{1+\alpha^2(s)}{\beta(s)} \; . \end{aligned} \tag{1.31}$$

$\alpha(s)$, $\beta(s)$ and $\gamma(s)$ are called Twiss parameters and are useful to describe the particle motion in a phase space defined at any machine point. As for a classic harmonic oscillator, the solution in the phase space $(x, x')$, where $x'(s) = \frac{dx}{ds}$, is represented by an ellipse which represents the single particle trajectory. In Figure 1.8(a) the phase space and the main dependences from Twiss parameter are shown.

The number of oscillations in the phase space for one revolution in the machine is given by the betatron *tune*, and it is equal to the phase advance in one turn divided by $2\pi$:

$$Q = \frac{\Delta\phi}{2\pi} = \frac{1}{2\pi}\oint \frac{ds}{\beta(s)} \tag{1.32}$$

If this number is an integer or a rational number, the motion could be unstable due to the fact that the trajectory of the particles is periodic, and this will result in an accumulation of defects and finally in beam loss. Thus, the tune has to be as close as possible to an irrational number in order to have non-periodic trajectories. This condition ensures the phase space to be dense, which means that at any location $s$ in the machine, the particles will cover all the possible $(x, x')$ positions on their ellipse.

Liouville's theorem establishes that the area of the phase space is a conserved quantity in a conservative system. In that case, if we define the emittance $\epsilon$ as $A = \sqrt{\epsilon}$, emittance should be conserved. However, an accelerator is not a conservative system. Several mechanisms lead to emittance growth [11]. The single particle emittance is defined as:

$$\epsilon = \gamma x^2 + 2\alpha x x' + \beta x'^2 \tag{1.33}$$

If we assume, in a statistical approach, a beam with a Gaussian shape in the transverse plane, the beam size and its divergence can be defined as:

$$\begin{aligned} \sigma(s) &= \sqrt{\epsilon\beta(s)} \\ \sigma'(s) &= \sqrt{\epsilon\gamma(s)} \end{aligned} \tag{1.34}$$

where now $\epsilon$ refers to the beam emittance that is defined as the single particle emittance that contains one $\sigma$ of the particles in the beam. With this definition, the beam core can be defined as the particles within $\pm 3\sigma(s)$ and the beam halo as the particles outside this region. In the simplest case, where $\gamma = 1/\beta$, the emittance can be defined as $\epsilon = \pi\sigma_x\sigma_{x'}$, but this definition is usually adopted in general, as the $\beta$ definition.

Concerning the beam divergence, since the angles are small, the following approximation can usually be adopted:

$$x' = \frac{dx}{ds} = \tan\theta \simeq \theta \simeq \frac{p_x}{p} \tag{1.35}$$

so that the beam divergence spread can be evaluated looking for the momentum spread in the transverse directions, normalized to the total momentum.

### 1.2.5 Matrix formalism

The Twiss parameters can be used to define a matrix formalism to describe the evolution of particles in the phase space. The system given by the general solution:

$$x(s) = a\sqrt{\beta_s(s)}\sin\phi_x(s) + b\sqrt{\beta_s(s)}\cos\phi_x(s) \tag{1.36}$$

and its derivative $x'(s)$ can be solved to evaluate the coefficients $a$ and $b$.

Then, it is possible to build the structure:

$$\begin{pmatrix} x(s_1) \\ x'(s_1) \end{pmatrix} = M(s_1|s_2)\begin{pmatrix} x(s_2) \\ x'(s_2) \end{pmatrix} \tag{1.37}$$

where $M$ is the *transport matrix.* This formalism is of particular interest when the full lattice optics is known (i.e. $\alpha(s)$, $\beta(s)$ and $\gamma(s)$). It allows evaluating the evolution of a given particle from one point to another in the machine. The passage through a dipole, a quadruple or any element can be represented by a matrix acting on the state vector.

For instance, free transport by $l$ is described by:

$$\begin{pmatrix} 1 & l \\ 0 & 1 \end{pmatrix} \tag{1.38}$$

in such a way that $x(s_2) = x(s_1) + x'(s_1)l\,;\ x'(s_2) = x'(s_1)$.

### 1.2.6 Dispersion function

A slight difference between the momentum of a particle and the reference momentum can induce a contribution in the transverse plane. The momentum deviation can be defined as:

$$\delta = \frac{\Delta p}{p_0} \tag{1.39}$$

where $p_0$ is the reference momentum. A particle, while travelling both in a dipole or in a quadruple, experiences a different bending or focusing which are proportional to $\delta$.

This effect is known as *chromaticity* and is solved in circular accelerators using sextupoles. Sextupoles induce a coupling of the two transverse axes, making the machine non-linear. Hence, the set of equations derived before are not exact for such a machine.

The equation of motion (1.26), considering only the effect of a dipole, is then modified as follows:

$$x''(s) + \left[\frac{1-\delta}{\rho^2(s)(1+\delta)} - \frac{B_1(s)}{B\rho(s)(1+\delta)}\right] x(s) = \frac{\delta}{\rho(s)(1+\delta)} \tag{1.40}$$

which is solved by a solution like:

$$x(s) = x_\beta(s) + D(s)\delta \tag{1.41}$$

where $x_\beta(s)$ is the usual solution, while $D(s)$ is called *dispersion function*, and solves the problem with an additional perturbation $\delta$.

By substituting Equation (1.41) in Equation (1.40), two different equations for the usual solution and the dispersion function can be obtained:

$$\begin{aligned} x''_\beta(s) + (k_x(s) + \Delta k_x(s))x_\beta(s) &= 0 \\ D''(s) + (k_x(s) + \Delta k_x(s))D(s) &= \frac{1}{\rho(s)} \end{aligned} \tag{1.42}$$

where $\Delta k(s)$ represents the additional perturbation term to the oscillator strength, due to chromaticity, and can usually be neglected.

Particles with different $\delta$ induce a shift to the orbit, which is proportional to $\delta$:

$$\begin{aligned} x(s) &= x_\beta(s) + D(s)\delta \\ x'(s) &= x'_\beta(s) + D'(s)\delta \end{aligned} \tag{1.43}$$

In the transverse phase-space, this shift can be represented by a shift in the ellipses, as shown in Figure 1.8(b).

## 1.3 Proton or positron drive schemes

The concept of proton driver scheme was mainly developed by the US Muon Accelerator Program (MAP). In this scheme, muons are generated as tertiary particles. A multi-GeV proton beam impinges on a heavy, high Z material target (a liquid Hg-jet production target is under R&D [12]) to produce mainly pions and kaons. It follows a decay channel in which the decays of kaons ($K^\pm \to \mu^\pm + \nu_\mu/\bar{\nu}_\mu$) and pions ($\pi^\pm \to \mu^\pm + \nu_\mu/\bar{\nu}_\mu$) produce muons. The number of low energy muons produced per year is $\sim 10^{21}$ starting with $\sim 10^{22}$ protons per year [12].

The majority of pions and kaons have few hundred MeV momenta, with a large longitudinal and transverse momentum spread. Hence, the initial muons are produced at low energy and with large longitudinal and transverse phase space. Therefore, the beam has to be cooled and captured, and the manipulations must be done quickly, before the muons decay.

In the upper part of Figure 1.9 the main elements of this scheme are presented.

The proton driver produces an high power, multi-GeV and multi-MW bunched beam of H$^-$

(then electrons are stripped away to make a proton beam). The buncher, made of an accumulator and a compressor, forms intense and short proton bunches.
In the target, inserted in a shielded enclosure to withstand the high proton beam power, pions are produced and then captured thanks to an high field solenoid.
A front-end, made of a solenoid decay channel equipped with RF cavities, captures the muons longitudinally into a bunch train, and then applies a time-dependent acceleration, to increase the energy of the slower bunches and decelerate the faster high energy bunches.
Muons are then cooled with the *ionization cooling* technique, that reduces the 6D phase space by a factor 50. The ionization cooling is an alternative way to obtain this phase space compression, still under study and optimization by the MICE (Muon Ioniziation Cooling Experiment) collaboration. The basic idea is to let the muon beam pass through a material, the absorber, in which it loses energy through ionization. Subsequently, the energy is restored in accelerating cavities. Transverse and longitudinal momentum are lost in equal proportions in the absorber, while RF cavities restore only the longitudinal momentum component. The combined effect of energy loss and re-acceleration reduces the ratio of transverse to longitudinal momentum, thereby decreasing the transverse emittance of the beam (transverse cooling) [13]. In an ionization-cooling channel the cooling time is short enough to allow the muon beam to be cooled efficiently with modest decay losses (4).

This technique has never been demonstrated experimentally and such a demonstration is essential for the development of future high luminosities muon accelerators in the proton driver scheme. Both the material of the absorber and beam properties that determine the performance of an ionization-cooling lattice have to be studied.
Finally, the beam is accelerated by a series of Recirculating Linacs Accelerators (RLA) or Fixed Field Alternating Gradient (FFAG) and Rapid Cycling Synchrotron (RCS), before the injection in the muon collider ring.

In the proton driver scheme, the limited capacity to cool the initial large emittance of muon beams, mainly due to the multiple scattering that also occurs in matter together with ionization, makes large muon beam currents mandatory to reach high luminosity. This enhances muon decay, that produces large background in the detector and surface radiation, that eventually limit the energy and the luminosity that can be reached.

To overcame these limitations, the LEMMA scheme aims at generating very small emittance muon beams, thus avoiding the need for muon cooling. This would allow to reach high luminosities with much smaller beam currents and consequently reduced detector background and surface radiation.

As shown in the lower side of Figure 1.9, LEMMA scheme is based on the production of muons from a positron beam, annihilating with electrons of a target. The energy of the positron beam is around 45 GeV, close to threshold for $\mu^+\mu^-$ pair production, that is:

$$E_{e^+} > E_{\mathrm{th}} \sim \frac{2m_\mu^2}{m_e} \simeq 43\,\mathrm{GeV} \tag{1.44}$$

In this way, the muon pair is produced almost at rest in the center of mass frame. Hence both muons are boosted in the laboratory frame nearly in the same direction, thus a good emittance

---

(4) Notice that typical cooling times in the electron-cooling technique, that is a cooling technique used mainly in proton accelerators, are between seconds and hours, long compared with the muon lifetime.

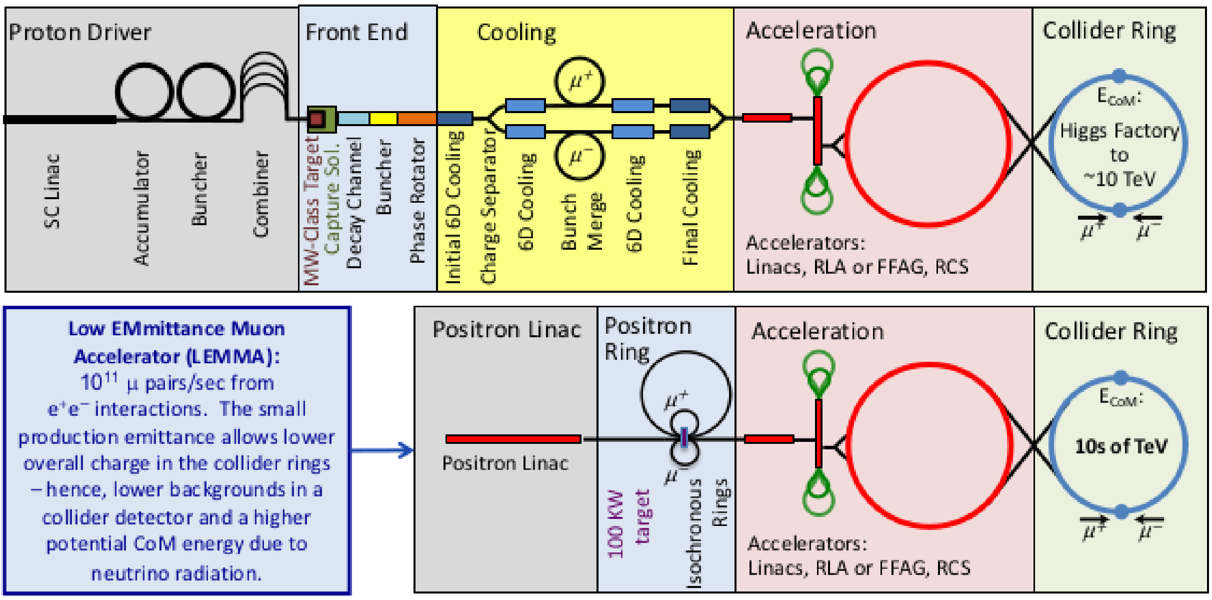

**Figure 1.9:** Schematic layouts of two Muon Collider accelerator complexes. The proton drive scheme is shown upside, the positron scheme downside.

is obtained since the very beginning.

The muon conversion efficiency is small, as shown in Figure 1.10 ($\sim 1.3 \cdot 10^{-6}$ muons per positron using a $0.3X_0$ Beryllium target [14]), so the production scheme has to be optimized. Different schemes will be presented in the next chapter.

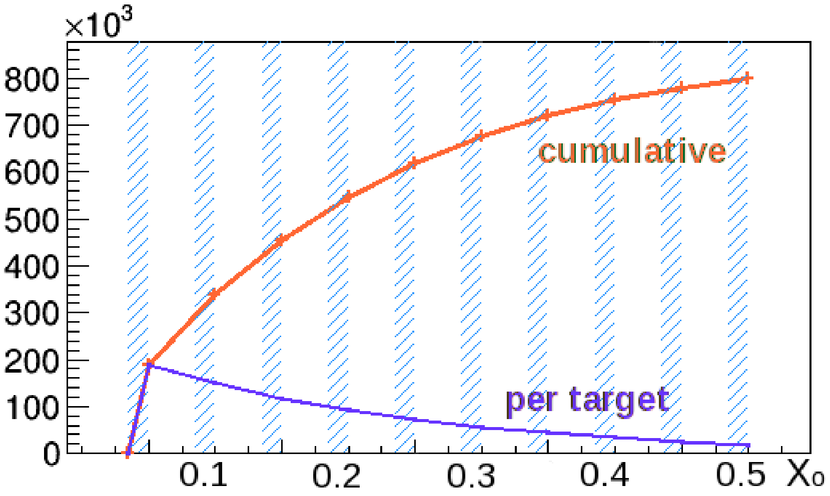

**Figure 1.10:** Number of muon pairs produced by $5 \cdot 10^{11}$ $e^+$ vs ten Beryllium targets of 5% radiation length each. The positron beam population above 43.7 GeV is reduced by bremsstrahlung.

Notice that in the proton scheme, due to the higher cross section of $\pi^+\pi^-$ or $K^+K^-$ production ($\sim 10^2$ mb), the muon production efficiency (after beam cooling) is much higher, of the order of 0.1 muons per incident 8 GeV proton [15].

# Chapter 2

# Regeneration of positrons for muon production in LEMMA

The main idea for muon production in the LEMMA scheme is the following. A positron beam is stored in a ring with high energy acceptance and low emittance. It is extracted and driven to a multi-target system to produce muon pairs at thresholds. This procedure will be repeated allowing for muons produced in this way to be accumulated before acceleration and injection in the muon collider.

The main properties of the produced muons are the following: low and tunable momentum in the center of mass frame (they are produced almost at threshold in this frame) and large boost, being $\gamma_\mu \simeq 213$ (the average energy of the muons in the laboratory frame has been considered, see Figure 2.2(b)). The resulting average laboratory lifetime is $\tau_{\text{lab}} = \tau\gamma_\mu \sim 470\,\mu$s.

The number of $\mu^+\mu^-$ pairs produced per positron bunch on the target is:

$$n(\mu^+\mu^-) = n^+\rho^- l\sigma(\mu^+\mu^-) \tag{2.1}$$

where $n^+$ is the number of positrons per bunch, $\rho^-$ the electron density in the target, $l$ the target thickness and $\sigma(\mu^+\mu^-)$ the muon pair production cross section.

The cross section is shown in Figure 2.1, and reaches its maximum value of about 1 $\mu$b at $\sqrt{s} \simeq 0.23$ GeV ($E_{e^+} \simeq 53$ GeV).

The main alternative process with respect to $\mu$ pairs production is the collinear radiative Bhabha scattering, which has a cross section of about 150 mb [14] (1).

This process sets the value of the positron beam interaction length for a given pure electron target density value. Using as reference value for the positron beam degradation the position in which its current (thus the number of positrons per second, $n(x) = n_0 e^{-x\rho^-\sigma_{\text{radBhabha}}}$) is decreased by $1/e$, the maximum value of the target density and length is $(\rho^- l)_{\max} = 1/\sigma_{\text{radBhabha}} \simeq 10^{25}$ cm$^{-2}$.

Now, the *muon conversion efficiency* can be defined as:

$$\epsilon(\mu^+\mu^-) = \frac{n(\mu^+\mu^-)}{n(e^+)}. \tag{2.2}$$

The previous value puts an upper limit to this efficiency:

$$\epsilon(\mu^+\mu^-)_{\max} = (\rho^- l)_{\max}\sigma(\mu^+\mu^-) \simeq 10^{-5} \tag{2.3}$$

---

(1) The simple Bhabha scattering has a lower cross section ($\sigma_{\text{Bhabha}} \sim 0.6$ mb).

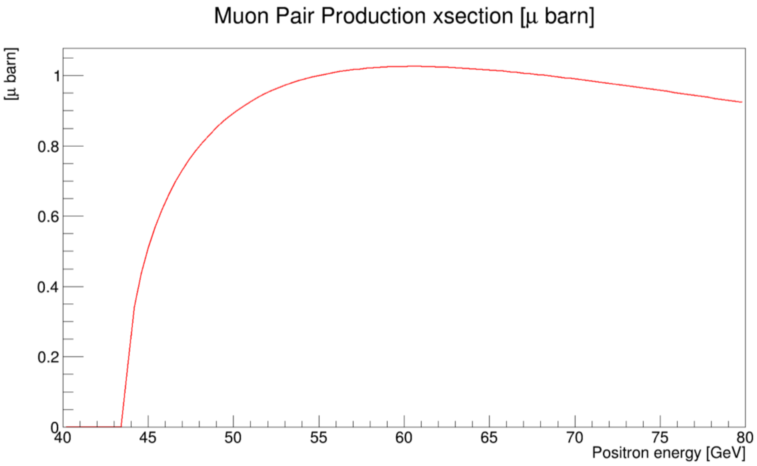

**Figure 2.1:** $e^+e^- \to \mu^+\mu^-$ cross section as a function of the positron beam energy.

The production angle of the outgoing muons, $\theta_\mu$, is maximum for the muons emitted orthogonally to the positron beam in the rest frame. In the approximation $\beta_\mu = 1$, its value can be easily obtained:

$$\theta_{\mu,\text{max}} = \frac{4m_e}{s}\sqrt{\frac{s}{4} - m_\mu^2} \tag{2.4}$$

However, in conventional targets, electromagnetic interactions with nuclei are dominant. Assuming a uniform distribution in the transverse $x$-$x'$ plane, the emittance contribution due to target thickness can be expressed by the variance of the distribution [14]

$$\epsilon_\mu = \frac{xx'_{\text{max}}}{12} = \frac{l(\theta_{\mu,\text{max}})^2}{12} \tag{2.5}$$

Multiple scattering effect increases the muon beam emittance because of the angular diffusion, characterized by [14]:

$$\sigma(x') \sim \frac{0.0136}{P[\text{GeV}]}\sqrt{l} \tag{2.6}$$

with $l$ in radiation length units.

The bremsstrahlung process reduces the positron beam population above muon production threshold, governing the $e^+$ beam degradation. The energy loss due to this process also increases with the radiation length, hence, to avoid large beam losses, the target thickness must be limited (and this also limits the number of muon pairs that can be produced).

In order to maximize the muon production efficiency and to reduce the emittance, light materials have better performances with respect to heavier materials. Through simulation studies, LEMMA collaboration found out that liquid Hydrogen, Beryllium, Carbon and Diamond are the best options [14].

In this study, as presented in Section 3.2, Beryllium has been chosen. In fact, even if liquid Hydrogen has better performances, Beryllium targets in practice represent the best option among solid targets (even if R&D is needed to demonstrate its feasibility).

Once muons have been produced, they have to be accumulated in a Muon Accumulator (MA) to form bunches of at least $O(10^8)$ muons. These bunches can be stacked in the same phase space by intercepting the positron beamline in the interaction points where muons are produced.

The stacking has to be fast because of the short muon laboratory lifetime of about 470 $\mu$s. At turn $N_T$, the number of bunches $n_b$ effectively accumulated is:

$$n_b = \sum_{i=1}^{N_T} e^{-\Delta t(N_T - i)/\tau_\mu^{\text{lab}}} \tag{2.7}$$

where $\Delta t$ is the positron bunch time spacing, synchronized with the time of a revolution in the muon ring. A saturation effect appears after $\sim 2\tau_\mu^{\text{lab}}$.

## 2.1 Production of low emittance muons

The properties of the muon source have been verified by the simulation (see Section 3.2). Here the main results are reported, in order to justify the LEMMA scheme and its advantages with respect to the classical proton driven scheme.

Notice that the cross section of positron annihilation into a muon pair is very small (maximum value 1 $\mu$b), and as the simulation pointed out only $\sim 1$ muon pair is produced with $\sim 1$ million initial positrons in the full target line. To enhance this factor without increasing too much the number of particles and hence the computing power, a bias factor of $10^5$ has been put to the process.

In Figure 2.2(a), the muon energy as a function of the production angle, for muons produced by a 45 GeV positron beam with small energy spread (0.1%) and divergence (see Section 3.3), is shown. The positron beam impinges on a single Berillium target of 3 mm length. The energy distribution is shown separately in Figure 2.2(b).

Thanks to the bias factor in the muon production, starting with one million positrons, the number of muons (both $\mu^+$ and $\mu^-$) produced in a single Beryllium target is around $10^4$ (see entries in the figures), so the full target line (composed by ten Be targets) produces around $10^5$ muons.

The muon production efficiency (number of muon pairs produced per incident positron) of the full target line is then around $6.8 \cdot 10^{-7}$. This is quite in agreement with the number evaluated by LEMMA [14] and derived by Figure 1.10.

The beam sizes and divergences of the muon beam in the transverse directions are shown in Figure 2.3(a) and Figure 2.3(b).

Following the definitions given in section 1.2.4, the emittances and $\beta$ can be calculated as:

$$\epsilon_x = \pi \sigma_x \sigma_{x'} \simeq 217\,\text{nm} \; ; \; \beta_x = \frac{\sigma_x}{\sigma_{x'}} \simeq 0.3\,\text{m} \tag{2.8}$$

and the same values in the y direction. See Section 3.3 for the characteristics of the positron beam from which these results are derived.

The muons are produced with a low emittance with respect to the proton-based scheme. First results of the MICE collaboration concerning the production emittance of $\sim 200$ MeV muons are shown in Figure 2.4 [16]. The emittance is of the order of 4 mm, more than four orders of magnitude larger. After cooling in the 6D phase space, the estimated emittance could be of the order of 20 $\mu$m [17].

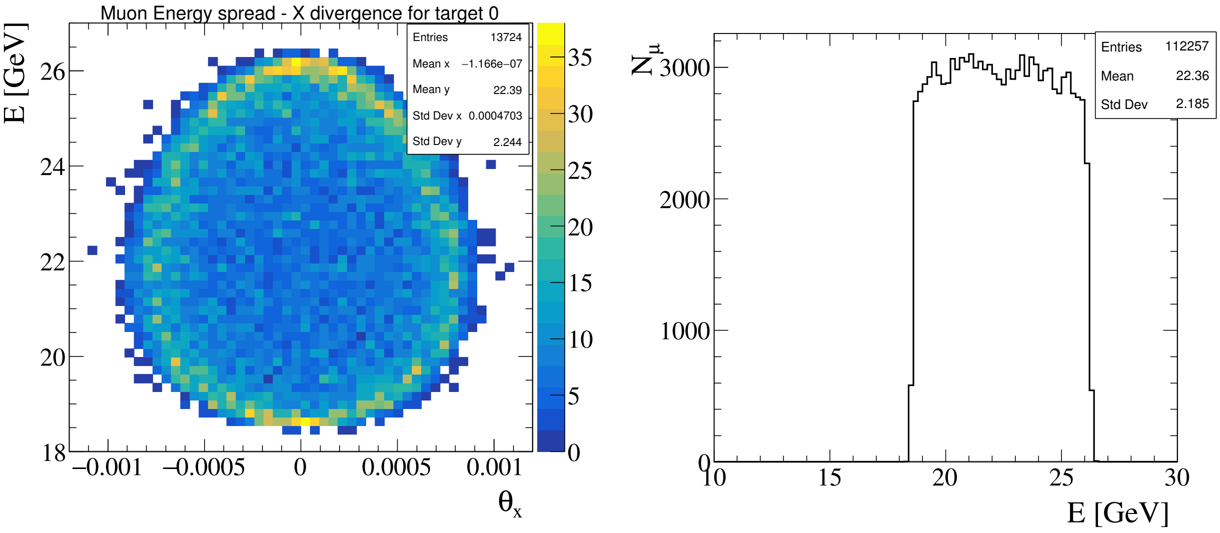

(a) (b)

**Figure 2.2:** (a) Energy versus angle of muons produced from a positron beam with a small energy spread and divergence. (b)Energy distribution of muons exiting the Beryllium target.

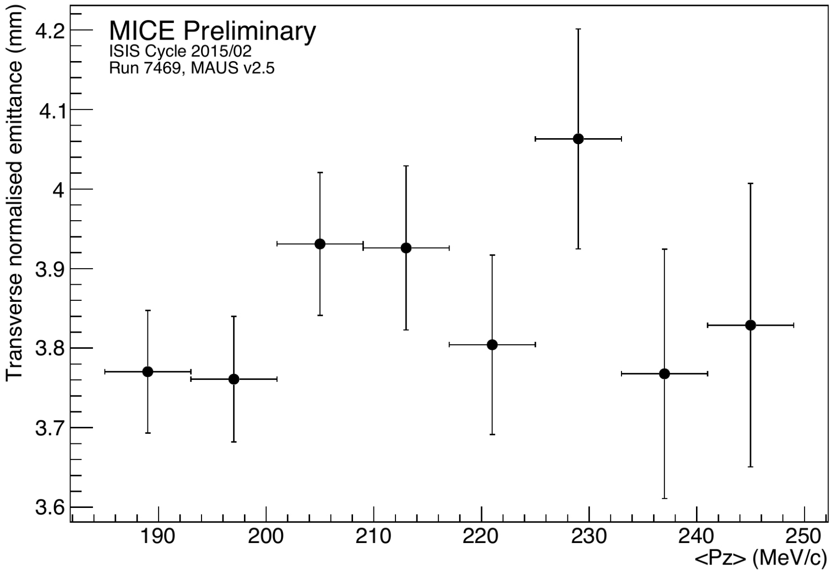

**Figure 2.4:** First direct measurements of the transverse emittance of the muon beam produced in MICE experiment (proton based scheme).

## 2.2 Muon source schemes

The main technical constraints to design a muon accelerator are imposed by muon physics and technological limits. The full muon production cycle should last less than a fraction of the muon lifetime, that is $\sim 470\ \mu$s, for instance 410 $\mu$s, in order to reduce the beam losses with respect to the accumulated intensity.

After the production cycle, muon bunches must be immediately re-accelerated to increase

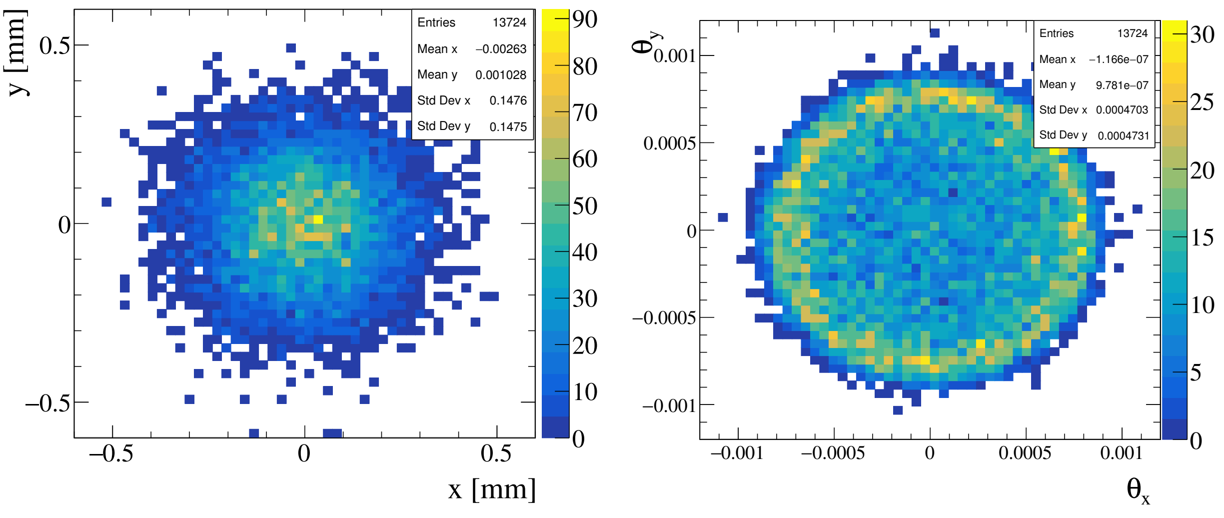

(a) (b)

**Figure 2.3:** (a) Beam size of the muon beam in the x and y directions. (b) Beam divergence of muons in the x and y directions.

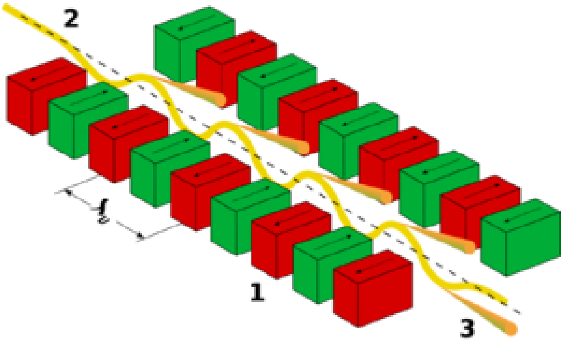

**Figure 2.5:** Working scheme of an undulator (1: magnets, 2: electron or positron beam, 3: synchrotron radiation exiting forward).

the lifetime and freeze the losses.

Moreover, the full cycle must take into account the time for the positron source production and cooling, either in the main positron ring or in a dedicated damping ring.

A damping ring is a circular accelerator designed to reduce (damp) the emittance of the particles (obtaining a “cooling” in the 6D phase space) by the emission of synchrotron radiation. In particular, this emission reduces the momentum of the particles. While in the longitudinal direction the loss is replaced by accelerating RF cavities, this does not happen in the transverse direction, so that at equilibrium the transverse emittance will be lower that without large radiation losses. However, transverse emittance is also increased by quantum effects (heating), so that the horizontal ring emittance is established by the equilibrium between quantum fluctuation heating and synchrotron radiation damping [4].

To increase the radiation losses, thus reducing the emittance of the particle beams, *undulators* or *wigglers* are used. These devices (see Figure 2.5) consist of a series of dipole magnets, whose magnetic field alternates along the length of the undulator with a wavelength $\lambda_0$. Electrons or positrons are forced to a fast oscillation (approximately sinusoidal with the same period of the magnetic oscillation), and thus radiate synchrotron power. The radiation produced in an undulator is very intense and concentrated in narrow energy bands in the spectrum. It is also collimated on the orbit plane of the particles. A useful parameter to characterize the two devices is:

$$K = \gamma\psi_0,\ \psi_0 = \left(\frac{dx}{dz}\right)_{z=0} = \frac{2\pi a}{\lambda_0} \tag{2.9}$$

where $\gamma$ is the relativistic factor, $\psi_0$ is the maximum angular deviation from the forward direction ($z$) and $a$ the maximum amplitude of the oscillation in the transverse ($x$) direction. For $K \ll 1$ the oscillation amplitude of the motion is small and the radiation displays interference patterns which lead to narrow energy bands. If $K \gg 1$ the oscillation amplitude is bigger, leading to a broad energy spectrum. The difference between undulators and wigglers is that wigglers work in this second regime [5].

The damping time must be compatible with a reasonable amount of synchrotron power emitted. For instance, it can range from 10 ms (in a low energy damping ring) to 80 ms (in a high energy positron ring).

Once a $e^+$ bunch has been spent it is mandatory to take into account a new $e^+$ bunch for the muon accumulation cycle. Having this large number of bunches in a high energy positron beam, limited by synchrotron radiation, is not easy, as shown in Section 1.2.2. To obtain this large number without drastically increase the beam current and hence the beam power, a very large positron ring is required. For instance, the LHC 27 km ring can be an option, while in a second phase the FCC 100 km ring could be used. Schemes presented below are based on the 27 km LHC ring.

A schematic table which summarizes the main technical challenges and possible solutions is presented in Figure 2.6. The following schemes represent some proposals (by LEMMA group) to overcome these challenges, and further studies are needed on them.

### 2.2.1 Scheme I

In the Positron Ring (PR), 1000 bunches with $5 \cdot 10^{11}$ $e^+$/bunch are stored at 45 GeV. After extraction, the positron bunches are sent to a multiple targets straight section, where muons are produced. After production, the $\mu^+$ and $\mu^-$ bunches are re-circulated in separate rings sharing the production line. Here they will circulate synchronously with the incoming “fresh” $e^+$ bunches in the target line, until two bunches of $\sim 10^9$ muons are produced.

Since the $e^+$ beam will be degraded at the end of the target line, an Energy Compressor Linac (ECL) will be needed to compress the longitudinal energy spread before the re-injection in the PR. The compression mechanism of this system is illustrated in Figure 2.7, which shows the transformations in the longitudinal phase space during energy compression [18].

The original bunch, with energy spread $y_0$ and phase spread $\delta\phi_0$, is represented by the vertical contours. The beam phase space is rotated after it passes through a magnetic chicane or similar device, emerging with a phase extent $\Delta\phi$. It applies a longitudinal dispersion, and must have no transverse dispersion and be non-focusing in both vertical and horizontal planes. Then, an RF accelerating system applies the compression. The horizontal contours show the bunch after compression. The goal is to recover at least 90% of the original $e^+$ bunch intensity.

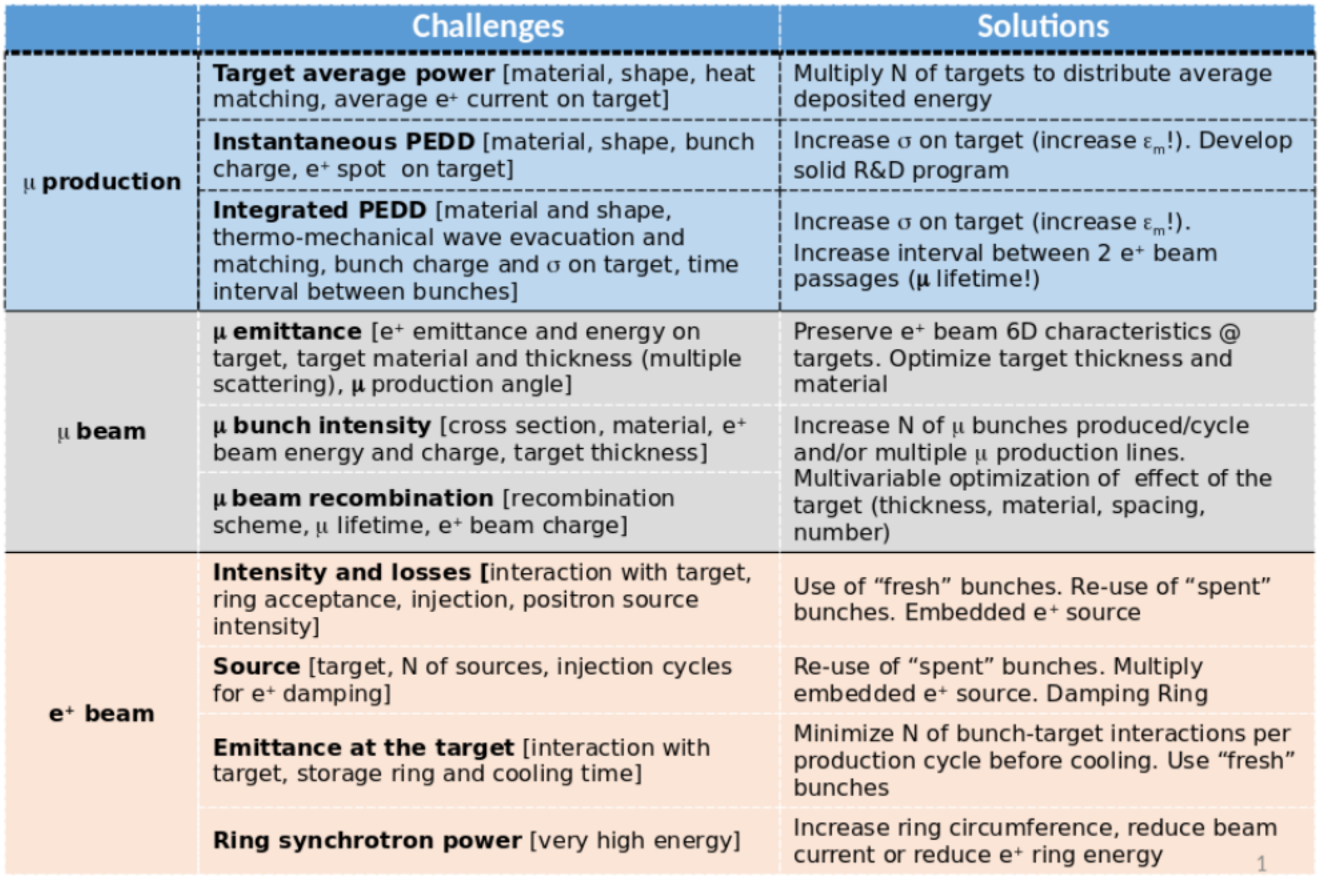

| | Challenges | Solutions |
|---|---|---|
| **μ production** | **Target average power** [material, shape, heat matching, average e⁺ current on target] | Multiply N of targets to distribute average deposited energy |
| | **Instantaneous PEDD** [material, shape, bunch charge, e⁺ spot on target] | Increase σ on target (increase $\varepsilon_m$!). Develop solid R&D program |
| | **Integrated PEDD** [material and shape, thermo-mechanical wave evacuation and matching, bunch charge and σ on target, time interval between bunches] | Increase σ on target (increase $\varepsilon_m$!). Increase interval between 2 e⁺ beam passages (μ lifetime!) |
| **μ beam** | **μ emittance** [e⁺ emittance and energy on target, target material and thickness (multiple scattering), μ production angle] | Preserve e⁺ beam 6D characteristics @ targets. Optimize target thickness and material |
| | **μ bunch intensity** [cross section, material, e⁺ beam energy and charge, target thickness] | Increase N of μ bunches produced/cycle and/or multiple μ production lines. Multivariable optimization of effect of the target (thickness, material, spacing, number) |
| | **μ beam recombination** [recombination scheme, μ lifetime, e⁺ beam charge] | |
| **e⁺ beam** | **Intensity and losses** [interaction with target, ring acceptance, injection, positron source intensity] | Use of "fresh" bunches. Re-use of "spent" bunches. Embedded e⁺ source |
| | **Source** [target, N of sources, injection cycles for e⁺ damping] | Re-use of "spent" bunches. Multiply embedded e⁺ source. Damping Ring |
| | **Emittance at the target** [interaction with target, storage ring and cooling time] | Minimize N of bunch-target interactions per production cycle before cooling. Use "fresh" bunches |
| | **Ring synchrotron power** [very high energy] | Increase ring circumference, reduce beam current or reduce e⁺ ring energy |

**Figure 2.6:** Key issues for the positron based muon collider by LEMMA. The main technical challenges and possible solutions for each of them are presented.

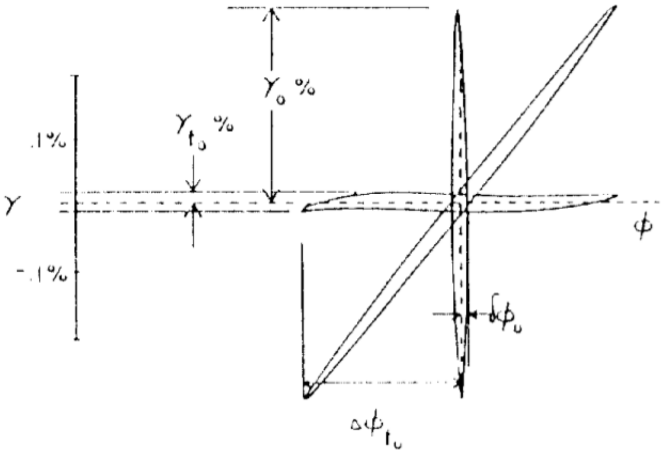

**Figure 2.7:** Longitudinal phase space progression during Energy Compression. The original bunch, with energy spread $y_0$ and phase spread $\delta\phi_0$, is represented by the vertical contours. The beam phase space is rotated after it passes through a magnetic chicane. The horizontal contours show the bunch after energy compression, made by an RF accelerating device.

The positron source can be split in two parts, each contributing to recover the required $e^+$ bunch population in the PR:

- a classical positron source (see Section 3.1), based on amorphous, crystal or hybrid target. It also provides the first slow spill injection in the main ring;
- due to the high gamma flux produced in the muon production target, it is possible to envisage an embedded source based on amorphous target at the end of this line.

The development and optimization of this second option is the aim of this thesis work.

Finally, the $e^+$ re-injection is assured by an high energy superconducting Linac or an Energy Recovery Linac (ERL).

An ERL is a class of electron or positron accelerators, used for generating a high average current and small emittance beam. Its working principle is illustrated in Figure 2.8. In an ERL, the beam is injected and then accelerated by a time-varying RF field stored in a superconducting linear accelerator. Then the beam is transported to a recirculation loop, where can be used for applications (X-ray or $\gamma$-ray source, electron or positron cooling or to provide the beam for a collider). After the recirculation, the spent beam is injected again into the superconducting accelerator so that the electrons are decelerated. In order to obtain this deceleration, the particles are transported back to the entrance of the linac 180° out of phase (see Figure 2.8). Therefore, the energy of the accelerated particles is converted back into the RF energy and recycled to accelerate the succeeding particles [19].

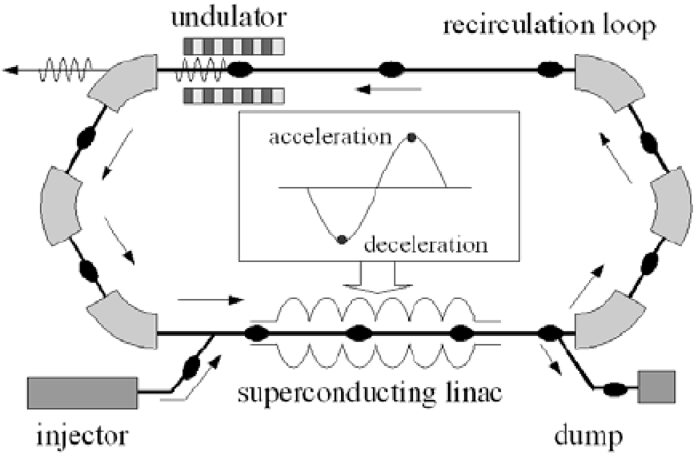

**Figure 2.8:** Principle of working of an energy-recovery linac. The electron or positron beam is accelerated in the superconducting linac and utilized for applications. The spent beam is decelerated in the same linac (after a phase-inversion) to recycle the beam energy. Finally, the beam is dumped at an energy close to its injection energy.

A layout of the complex for Scheme I is shown in Figure 2.9(a).

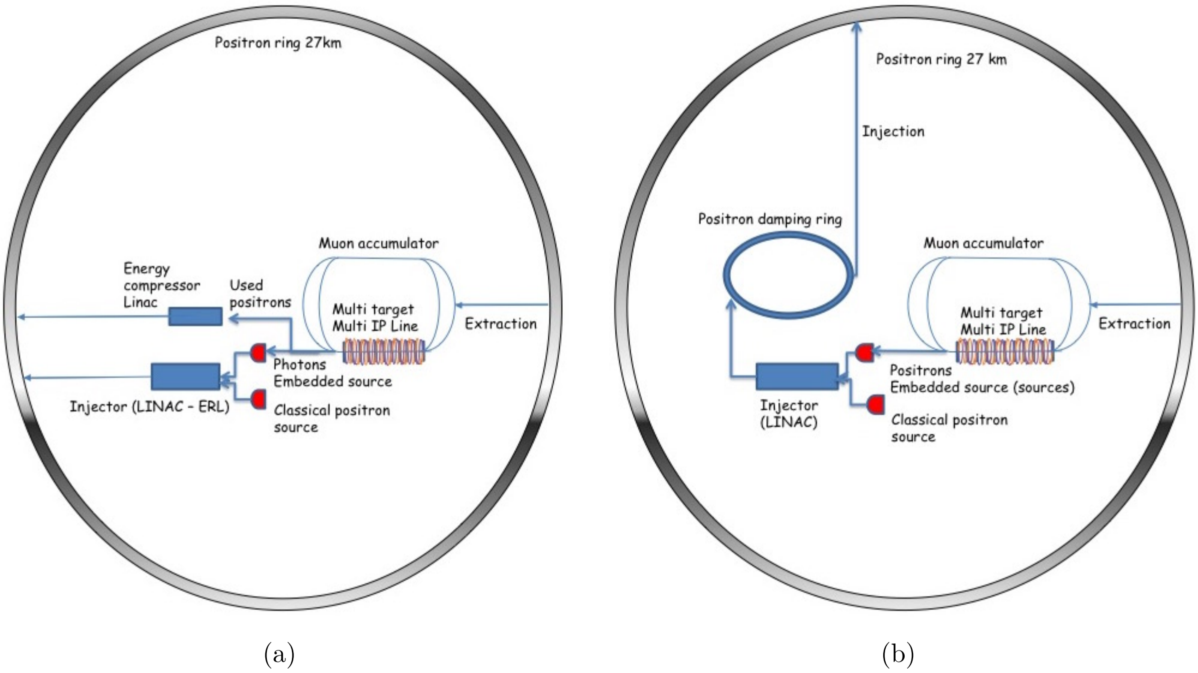

**Figure 2.9:** (a) Layout of Scheme I accelerator complex. (b) Layout of Scheme II accelerator complex.

The timeline of the schemes must take into account the time for storing and cooling of positron beam, for positron extraction and muon production, and also for target cooling, both for the main multi-target complex and the embedded source. For the sake of simplicity, only the timeline of this scheme is presented in details. The timeline of the other schemes is similar.

The full muon production cycle, illustrated in Figure 2.10, can be divided in different phases, each identified by the action of each of the systems and by their duration [14].

- Phase 0: during this phase, the positron source and the injection Linac have to produce, accelerate to 45 GeV and inject 1000 bunches of $5 \cdot 10^{11}\, e^+$. This can be done with a positron source of $10^{12}\, e^+$/s and a 800 nA average current beam. To reduce the average current on the $e^+$ source and the injection Linac, this action can be fulfilled in a long period, for instance 100 s. All other systems are in stand-by in this phase.

- Phase 1: this phase consists in the cooling of the beam in the main PR for two damping times, corresponding to 80 ms. In this phase the PR is filled with a 0.88 A average current beam, emitting $\sim$ 100 MW of synchrotron power.

- Phase 2: in this phase, the muon production happens in 410 $\mu$s. All the 1000 positron bunches are extracted with a delay of 410 ns (delay loops will allow for synchronization with the muon bunches, hence the period in the Muon Accumulator (MA) is also 410 ns) and injected in the targets line. Bunches of $\mu^+$ and $\mu^-$ will be produced at each passage. The muon bunches will circulate synchronously with the positron bunches in a dedicated MA ring $\sim$ 120 m long. Muons are accumulated until a bunch intensity of about $10^9$ muons is reached, and given the period in the MA, the average current is $\sim$ 400 $\mu$A.
  The high energy gamma ray flux, produced by the positrons in the targets line, can be used to produce new positrons in an "embedded source". After the targets, the positron bunches are collected by a magnetic system and then accelerated by an Energy Compressor Linac,

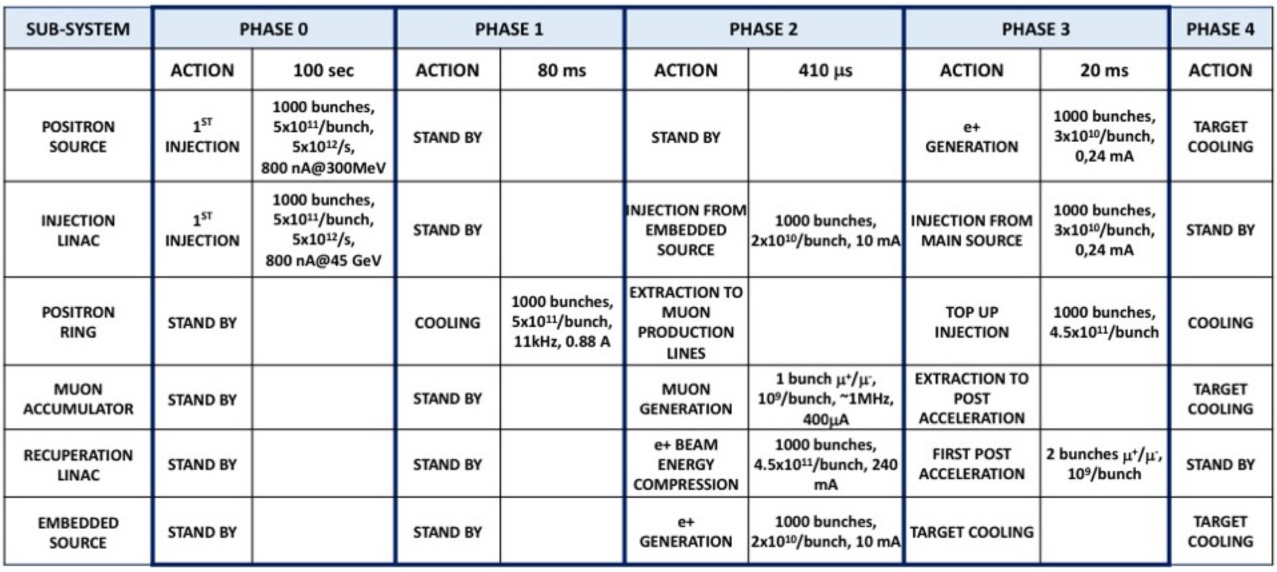

| SUB-SYSTEM | PHASE 0 | | PHASE 1 | | PHASE 2 | | PHASE 3 | | PHASE 4 |
|---|---|---|---|---|---|---|---|---|---|
| | ACTION | 100 sec | ACTION | 80 ms | ACTION | 410 $\mu$s | ACTION | 20 ms | ACTION |
| POSITRON SOURCE | 1$^{ST}$ INJECTION | 1000 bunches,<br>5x$10^{11}$/bunch,<br>5x$10^{12}$/s,<br>800 nA@300MeV | STAND BY | | STAND BY | | e+ GENERATION | 1000 bunches,<br>3x$10^{10}$/bunch,<br>0,24 mA | TARGET COOLING |
| INJECTION LINAC | 1$^{ST}$ INJECTION | 1000 bunches,<br>5x$10^{11}$/bunch,<br>5x$10^{12}$/s,<br>800 nA@45 GeV | STAND BY | | INJECTION FROM EMBEDDED SOURCE | 1000 bunches,<br>2x$10^{10}$/bunch, 10 mA | INJECTION FROM MAIN SOURCE | 1000 bunches,<br>3x$10^{10}$/bunch,<br>0,24 mA | STAND BY |
| POSITRON RING | STAND BY | | COOLING | 1000 bunches,<br>5x$10^{11}$/bunch,<br>11kHz, 0.88 A | EXTRACTION TO MUON PRODUCTION LINES | | TOP UP INJECTION | 1000 bunches,<br>4.5x$10^{11}$/bunch | COOLING |
| MUON ACCUMULATOR | STAND BY | | STAND BY | | MUON GENERATION | 1 bunch $\mu^+/\mu^-$,<br>$10^9$/bunch, ~1MHz,<br>400$\mu$A | EXTRACTION TO POST ACCELERATION | | TARGET COOLING |
| RECUPERATION LINAC | STAND BY | | STAND BY | | e+ BEAM ENERGY COMPRESSION | 1000 bunches,<br>4.5x$10^{11}$/bunch, 240 mA | FIRST POST ACCELERATION | 2 bunches $\mu^+/\mu^-$,<br>$10^9$/bunch | STAND BY |
| EMBEDDED SOURCE | STAND BY | | STAND BY | | e+ GENERATION | 1000 bunches,<br>2x$10^{10}$/bunch, 10 mA | TARGET COOLING | | TARGET COOLING |

**Figure 2.10:** Timeline of Scheme I.

to be injected back in the PR. Assuming that $\sim 90\%$ of the initial positrons are recovered, the compressor Linac has 240 mA of pulsed current and 720 $\mu$A average current (1000 bunches of $4.5 \cdot 10^{11}$ $e^+$ at 10 Hz). To restore completely the beam, at the same time the embedded source should provide $2.5 \cdot 10^{10}$ $e^+$ (depending on embedded source efficiency), for a pulsed current of 13 mA in the injection Linac.

- Phase 3: the main positron source produces and provides to the injection Linac the missing 1000 bunches with $2.5 \cdot 10^{10}$ $e^+$ (if needed), that are injected in the PR in $\sim 20$ ms. The muon bunches are extracted and sent to fast acceleration. The PR is filled with the nominal bunch charge of $5 \cdot 10^{11} e^+$ per bunch. In the embedded source the target cools down.
- Phase 4: end of the cycle, restarts from Phase 1 and continues at 10 Hz ($\sim$ 80 ms of phase 1 plus 20 ms of phase 3). In this phase, the main targets-line and the embedded source cool down.

### 2.2.2 Scheme II

The second scheme aims to take into account some of the critical points and parameters of the first one. One is the high synchrotron power emitted by the 45 GeV positron beam, which from (1.12) is about 100 MW. A way to reduce it is to substitute the 45 GeV injector Linac with a system composed by a 5 GeV injector Linac and a 5 GeV, 27 km long, Damping Ring (DR) in the same PR tunnel. In this way the synchrotron power is reduced by a factor of about 6500. The PR energy is ramped up to 45 GeV only in a second moment (at muon production time) and for a short time.

The $e^+$ source is again constituted by a classical and an embedded source, however the embedded source uses as driven beam the positron beam exiting the multi target line, and not the emitted photons. This possibility is also subject of this study. The newly produced positrons are then cooled in a DR before the injection in the PR.

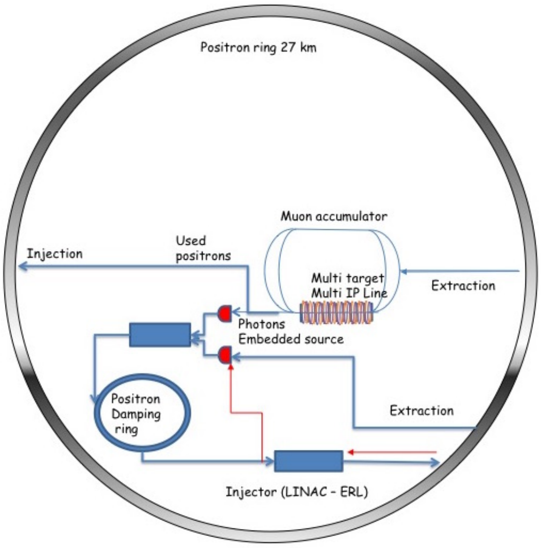

**Figure 2.11:** Layout of Scheme III accelerator complex.

In this case the “spent” positron bunches, after the target interactions, are sent to the embedded positron source to provide the regeneration of all the positron bunch population, hence a 100% efficiency ($e^+$ captured / $e^+$ on the target) is needed.

Figure 2.9(b) shows the layout of the complex for Scheme II.

### 2.2.3 Scheme III

In the third scheme, as in the previous one, a DR is again used to cool down positrons produced from the $e^+$ source. However, a design for a partial recovery of the “spent” $e^+$ bunches is included, even if only a $\sim 70\%$ efficiency can be reached, due to the high energy spread generated in the targets interactions and the limited PR energy acceptance.

The main advantage is that this allows to have a slow extraction (20 ms) of the $e^+$ for the following $e^+$ production, and consequently a slow injection in the DR, so the current in the Linac system in not too high. In the other schemes, the positrons have to be injected in the main ring during the muon production cycle, that takes about 410 $\mu$s (less than muon decay time), with a consequent extremely high value of the pulse current. The solution of scheme III avoids to operate the Linac system in this short time (in fact the positron beam is injected without a Linac system), so it operates with a lower current.

The possibility of a deceleration phase in the injection Linac is also taken into account, since the energy acceptance of the $e^+$ source increases for a lower energy beam. No beam will circulate in the PR during the DR cooling phase, so the synchrotron radiation emission is reduced with respect to scheme I. Figure 2.11 shows the layout of the complex for Scheme III.

# Chapter 3

# Geant4 simulation of embedded source

In this chapter, a brief introduction of positron sources and of the Geant4 simulation software are given. Then, results of several simulations performed using the geometry described in Section 3.2.2 are shown. The parameters of the embedded source are changed in order to maximize the final positron yield, taking into account the deposited power and the Peak Energy Density Deposition (PEDD). The PEDD is the maximum value of the energy density deposited in the target, after a division in smaller volumes, and it is measured in J/g or in MeV/cm$^3$. Positrons and secondary particles distributions are analysed at different positions of the target line.

## 3.1 Positron sources

Classical positron sources are based on gamma pair production. A basic scheme is shown in Figure 3.1. A first linear accelerator produces an electron beam, with an energy depending on the flux requirements (starting from few GeV). The beam impinges on a converter target producing gamma rays by bremsstrahlung, subsequently converted into $e^-e^+$ pairs in the nuclear potential of the atoms. The produced pairs contributes to gamma rays and pair production, thereby originating the development of an e.m. shower. All the primary beam characteristics "memory" is lost in positron production [20].

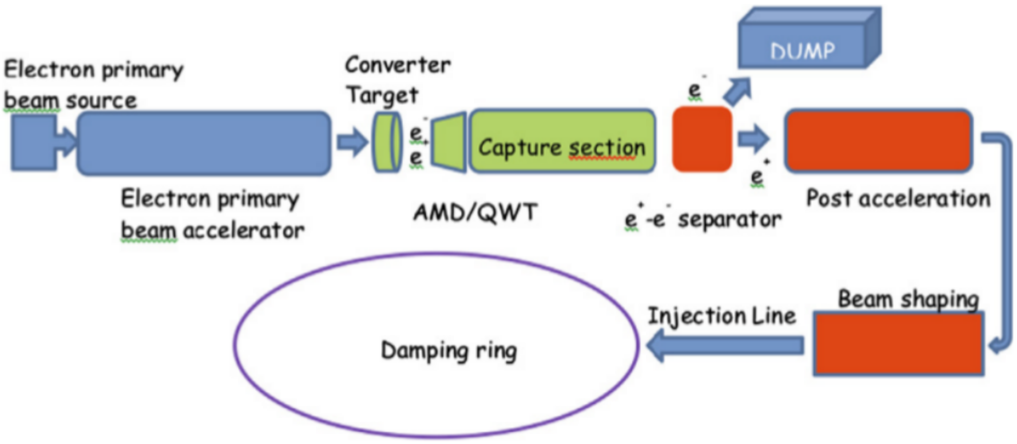

**Figure 3.1:** Basic scheme of the positron sources, which shows the different systems involved.

Some very challenging constraints in positron sources are:

- The Peak energy deposition density (PEDD) on the converter: it introduces a high thermo-mechanical stress and a related target failure threshold, limiting the positron production per bunch.
- The thermal property of the material, in particular its melting point (e.g. 3695° for tungsten [20]): it constraints the average current.

After the production, the positron beam has a strong angular divergence and energy spread, resulting from the shower processes and from the multiple scattering. So a focusing system (as AMD or QWT, see Chapter 4) is needed to reduce the angular spread. After the transverse shaping, a reduction of the longitudinal phase space spread and a first acceleration is done by means of a capture section, i.e. a series of RF sections enclosed by solenoids (see Section 3.6). Also these systems influence the positron current.

After the transverse and longitudinal shaping, it is possible to separate the positrons from the electron beam with a dipole magnet, reduce the 6D emittance in beam shapers and then inject the positrons in a damping ring.

To overcome the constraints imposed by the PEDD threshold and the thermo-mechanical stresses on the target, the positron sources of some modern projects, as the International Linear Collider (ILC) and the Compact LInear Collider (CLIC), are based on innovative designs all based on one concept: the separation of the produced photon from the primary beam [20]. In this way, only the high-energy gamma rays impinge on the converter target, excluding the heating and the thermal gradient given by the primary beam energy losses.

For instance, the project for the International Linear Collider (ILC) Positron Source (see Figure 3.2) will use photoproduction to generate positrons in the following way. The main linac produces a high energy electron beam passes through a long helical undulator to generate a multi-MeV photon beam which then strikes a thin metal target to generate positrons in an electromagnetic shower. The positrons are captured using an optical matching device (OMD) and normal conducting (NC) L-band RF with solenoidal focusing, accelerated to 125 MeV and then transported to the Damping Ring. Electrons and remaining photons are separated from the positrons and dumped [21].

The positron source must perform three critical functions: generate a high power multi-MeV photon production drive beam in a suitable short period, with high $K$-value (defined in Section 2.2) helical undulator; produce the needed positron bunches in a metal target that can reliably deal with the beam power and induced radioactivity; capture and transport the positron bunch to the Damping Rings with minimal beam losses.

In the '90s, the SLC $e^+$ source (best) performances were around $5 \cdot 10^{12}$ $e^+$/s. Nowadays, $e^+$ sources like the ILC [22] or CLIC [23] ones are designed to produce $10^{14}$ $e^+$/s. Hence the initial injection in LEMMA, which has to provide 1000 bunches of $5 \cdot 10^{11}$ $e^+$/s, is not a problem, since there are no time constraints, and the injection can last 5 seconds.

However, the source needed to replace the $e^+$ lost in the muon production process is very challenging, since the time to produce, damp and accelerate the positrons is very short.

For instance, considering scheme III, $\sim$ 30% of the initial positrons must be produced, damped and accelerated in a time cycle of 50 ms, corresponding to a 20 Hz repetition rate.

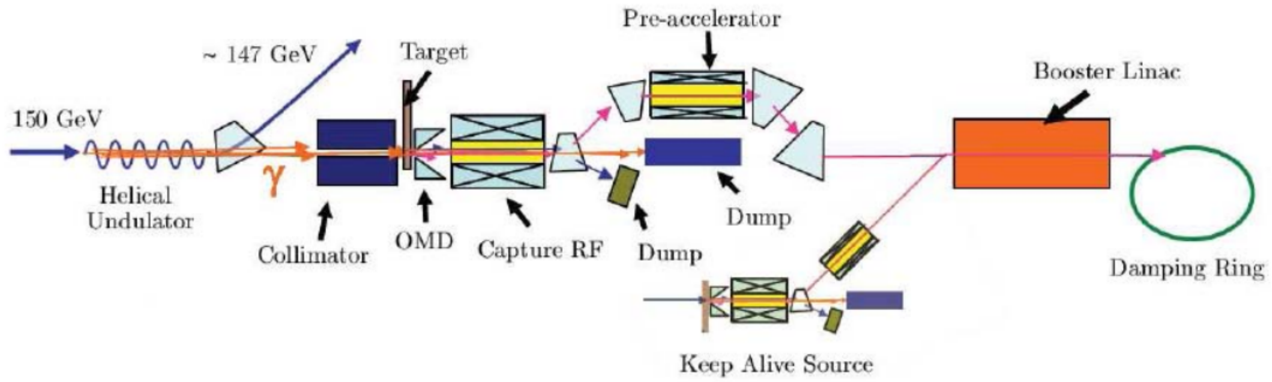

**Figure 3.2:** Schematic layout of the ILC positron source. The electron 150 GeV beam (generated by the main linac) passes through a long helical undulator to generate a multi-MeV photon beam which then strikes a thin metal target to generate positrons in an electromagnetic shower. Positrons are then captured, accelerated and transported to a Damping Ring.

The required production rate is then $0.3 \cdot 1000$ bunch $\cdot\, 10^{11} e^+$/bunch $\cdot\, 20\ \mathrm{s}^{-1} = 3 \cdot 10^{15} e^+$/s. This bunches must be injected in the damping ring during 20 ms and then stored to damp the emittance in the remaining 30 ms.

To develop such a target, an R&D program on new targets (that could be hybrid targets and rotating targets [14]) is needed. Another possibility is reducing the requested positron rate by increasing the energy acceptance of the positron ring, that is estimated to be between ±2% and ±8%, depending on the lattice optics and the emittances [14]. In this way, the fraction of positrons lost during injection in the main ring would be reduced. Alternatively, more than one source can be used to achieve such a high rate.

## 3.2 Geant4 simulation

Geant4 is a toolkit for the simulation of the passage of particles through matter using Monte Carlo methods. It uses object oriented programming (C++).

It includes libraries to develop high level aspects of the simulation, such as geometry, tracking, run management and so on.

Its areas of application include high energy, nuclear and accelerator physics, as well as studies in medical and space science.

### 3.2.1 Geant4 features

There are three mandatory C++ classes in Geant4:

- Detector Construction: this class allows to construct the geometry of the experiment, defining shapes, materials (both by default materials and by defining them) and positions in the main volume. Moreover, it may be used to define regions (collection of volumes that may have unique features, for instance concerning the production of particles) and electromagnetic fields. Both geometry and fields can be given as external files.
- Physics List: this class allows to define the physics models one wants to use in the simulation, which can depend on the energies involved, computation speed, particle types

and so on. First the particles are defined, then for each one the relevant physics processes are assigned. The processes describe how particles interact with matter. Then, range cuts for secondary production must be set. To avoid extremely long calculations, particles unable to travel for at least a minimal range are not produced.

- The Primary Generator Action class controls the generation of primary particles, including particle type, energy, direction, starting point and time. The interactions of one particle at a time are simulated, but a realistic beam can be introduced by defining emittances, angular and energy spread of the particles and the number of particles.

Concerning physics processes, there are three kinds of actions: actions that happen at rest (like decays or positron annihilation), along step, that is during the motion (to describe continuous interactions like Cherenkov effect or ionization) and post-step actions, to describe point-like interactions that depends on the cross section of the processes.

When a particle is shot, its first processes is “transportation”. Then, all processes associated to the particle (and defined in the physics list) propose a geometrical step length, which depends on process cross-section and is extracted randomly. The process proposing the shortest step “wins” and the particle is moved to the destination (also the particle final state is extracted). During this action, all processes along the step are executed. Then, the winner post-step process is executed, and new particles are pushed to the stack. Finally, if the kinetic energy is zero, all at rest processes are executed. If particle is stable, it is killed, else new step starts, and sequence repeats.

In Geant4 language, the *track* is a snapshot of the particle, and keeps all current information of the particles. An event is a collection of tracks. The track is updated after every step. A track is deleted when it goes outside the world volume, it disappears in an interaction, it looses all the kinetic energy or it is manually killed by the user.

Several other classes allow to gain control of the simulations at various stages: run, event, tracking and stepping action. Each of them contains functions that describe actions to be done at the beginning and end of each stage.

The run covers the entire simulation, until the last particle in the beam is shot. It is a collection of events, and each event consists of the interaction of one particle of the beam with the material. At the beginning of the event, primary tracks are generated and pushed into a stack. Tracks are popped up from the stack one-by-one and tracked. Secondary tracks are also pushed into the stack, and when the stack gets empty, the event is fully processed.

The stepping action functions controls the step in the particle propagation, which is updated each time a process is invoked, since particle properties change after a step. Informations can be extracted from a step after it is completed. Output histograms can be filled in this functions, retrieving information from a step, such as the particle type, the particle energy at some point of the detector, its momentum and position, the energy deposited in the detector, and so on.

The output of the simulation can be organized in files of different formats, like csv, ASCII and ROOT. In our case the ROOT file has been chosen.

Another way to retrieve physical informations is using command-based scoring. A useful functionality of this method is the possibility of defining a mesh in a material. The material is hence divided in small segments or portions of different shapes, and different scorers, such as dose, flux, deposited energy, can be calculated for each portion. The mesh geometry can be

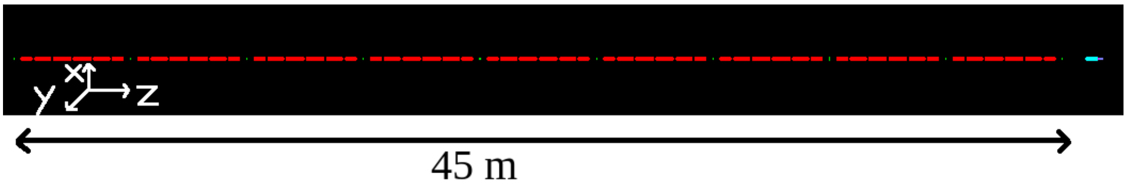

**Figure 3.3:** Scheme of geometry of the simulation. Green: Berillyum targets; yellow: Tungsten target; red: quadrupoles. The full line is about 45 m long.

completely independent from the real material geometry, and is useful for example to analyse the thermo-mechanical response of the material, which is related to the power density in the material.

### 3.2.2 Geometry of the simulation

In Figure 3.3 a scheme of the geometry is shown. The positron beam comes from the left side, and impinges in a Target Line. The Target Line is situated outside the main Positron Ring, so that the beam has to be extracted from the ring. In this configuration, the target line consists of ten Be targets (the green ones). The Be targets are cylindrical, with a radius of 5 cm and a depth of 3 mm. Each Be target is separated from a distance of about 5 m, and in this space there is a transport line, where magnets are common to the three beams ($e^+$, $\mu^-$ and $\mu^+$). This transport line (a detail is shown in Figure 3.4(a)) is made of quadruples (in red) with alternate gradients of about 170 T/m (positive and negative) and drift spaces. It should focus the beam at each interaction point (IP) to achieve the production of new muons reducing the growth of the final beam emittance [14]. This scheme has been called “multiple IPs, multiple targets”, in order to distinguish it from a similar scheme in which the beryllium target is split in the same way but there is no transport line, and the separation distance is much smaller (“single IP, ten targets”).

Corrections for the chromatic effect (see Section 1.2.6), which are introduced by dipoles and sextupoles, are not implemented, because this would split the three beams.

After the target line, at a distance of about 45 meters from the first Be target, the tungsten positron regenerator is shown in yellow (a detail is shown in Figure 3.4(b)). Its dimensions and its distance from the last Be target are variable, to be optimized.

This is only one of the possible target and optics lines, but the simulation is very flexible, since it is enough to change the input file (which is a *.gdml* file) to change the whole target line geometry.

After the study of the embedded source, a capture system is also introduced. It consists of an Adiabatic Matching Device, and a box to count the number of positrons at the AMD exit (see Figure 3.4(c)). This option is described in detail in Section 4.3.

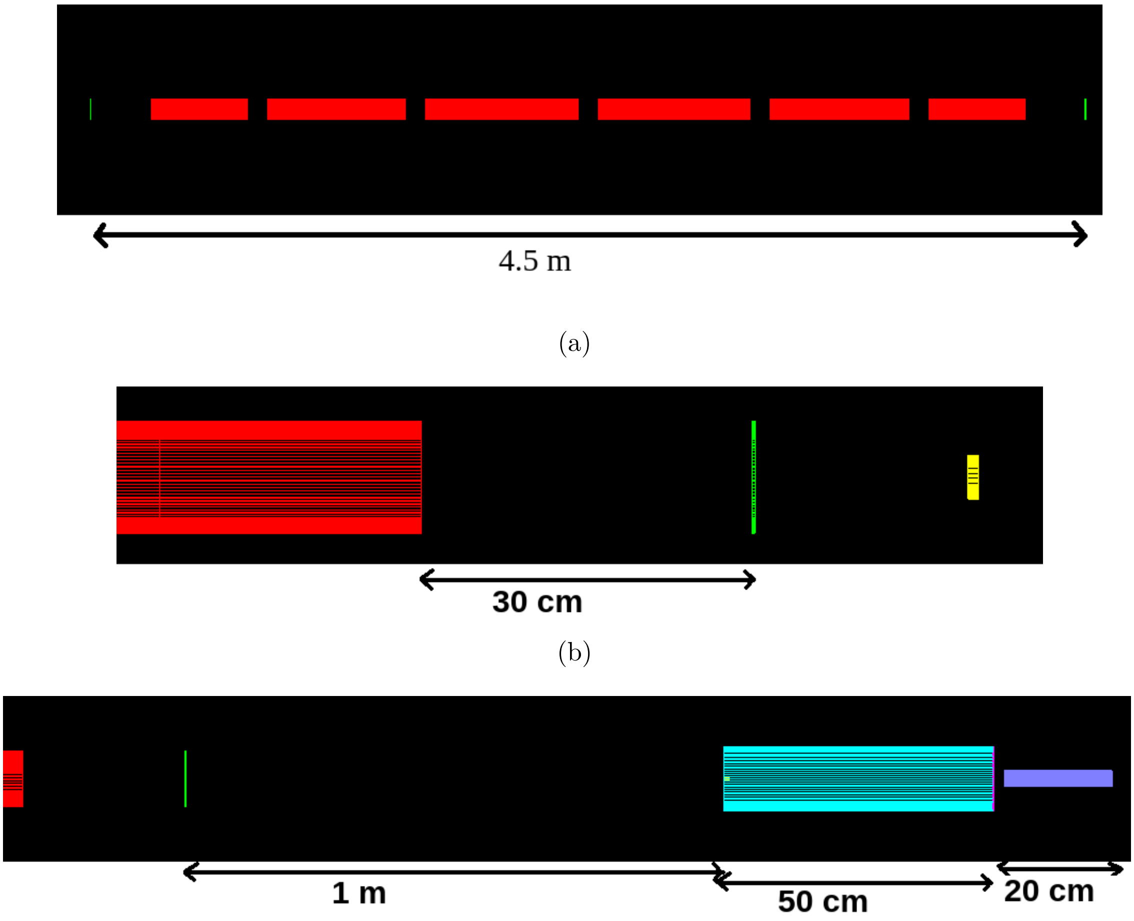

(a)

(b)

(c)

**Figure 3.4:** (a) Detail of the transport line. Two Beryllium targets (in green) are separated by six quadruples (in red) and drift spaces, in black. (b) After the last Beryllium target, a tungsten target, 1 cm long (2.8 $X_0$), in yellow, is positioned for positron regeneration. (c) A capture system is put after the tungsten target. It is made by an Adiabatic Matching Device, 50 cm long, with a decreasing magnetic field along $z$, and an RF box, which is not simulated but is introduced to count the number of positrons with the right angles and positions. The tungsten target is positioned around the peak of the magnetic field (5 T). The magnetic field is decreased adiabatically to 0.5 T in order to couple with the solenoidal field of the accelerating sections.

### 3.2.3 Physics List of the simulation

Another important aspect in the simulation is the Physics List. The particles included are leptons (electrons, muons and neutrinos), photons, proton and antiproton, pions and kaons. These are the processes included in the simulation for photons, electrons and positrons:

- photons can interact via photoelectric effect, Compton scattering, Rayleigh scattering and pair production.
- electrons can interact via electromagnetic interactions in single and multiple scattering processes, ionization, bremsstrahlung and synchrotron radiation; the same for positrons with the addition of positron annihilation and positron annihilation into a pair of muons.

Also the minimal range of energy for secondary particles production are set for each material in the physics list. The range of Beryllium and tungsten targets have been set at 1 mm.

Converting this threshold in energy, this means that photons of energy below $\sim$ 100 keV are not produced, as well as positrons and electrons of about 2 MeV (1). This is not a problem, since the positrons that can be collected by the optics after the regenerator have usually energies above 5 MeV. Notice that even if this particles are not produced, the energy deposition of the parent particles takes into account for them.

## 3.3 Positron beam

The positron energy has been set at 45 GeV. LEMMA collaboration found that the efficiency, that is the number of muons produced per incident positron, of a 0.3 $X_0$ Beryllium target is $1.3 \cdot 10^{-6} \mu/e^+$ (see Figure 1.10). The total length of the used Beryllium targets is about 0.1 $X_0$ ($X_0$(Be) = 35.28 cm), and the efficiency in this case is $6.8 \cdot 10^{-7} \mu/e^+$ (this number has been reproduced as described in Section 2.1). This non-linearity is due to the fact that the number of positrons above threshold for muon production is reduced after the interactions in a muon target, because of bremsstrahlung. Hence, in the second target the degraded $e^+$ beam will produce a lower number of positrons, and so on. To reduce this effect, the possibility of a 48 GeV beam has been considered. In this case the total Be length after which the muon production does not happen is increased, however the energy spread of the muon beam increases. So the option of a 45 GeV beam is preferred.

The positron beam sizes and divergences in the $x$ and $y$ directions have been set at:

$$\sigma_x = \sigma_y = 7.6 \cdot 10^{-5}\,\mathrm{m} = 76\,\mu\mathrm{m}\ ;\ \sigma_{x'} = \sigma_{y'} = 7.6 \cdot 10^{-5} \tag{3.1}$$

Hence, following the definition given in section 1.2.4, the emittances and $\beta$ are:

$$\epsilon_x = \pi \sigma_x \sigma_{x'} = 18.2\,\mathrm{nm} = \epsilon_y\ ;\ \beta_x^* = 1\,\mathrm{m} = \beta_y^* \tag{3.2}$$

The beam size in the $z$ direction (along the ring) is set at zero, while the energy spread is $\frac{\sigma(E)}{E} = 0.1\%$ (that is $\sigma(E) = 45$ MeV), according to the LEMMA designs.

The distributions in position (x and y, the transverse coordinates) and angle (the polar angle in cylindrical coordinates) are shown in Figure 3.5(b) and Figure 3.5(c) for the primary beam. In Figure 3.5(a) is shown the energy distribution with the energy spread.

---

(1) This number must be a compromise between accuracy (going low enough in energy to get the interesting physics) and machine time of calculations (not too low because some processes, as bremsstrahlung, have infrared divergence, causing huge CPU time).

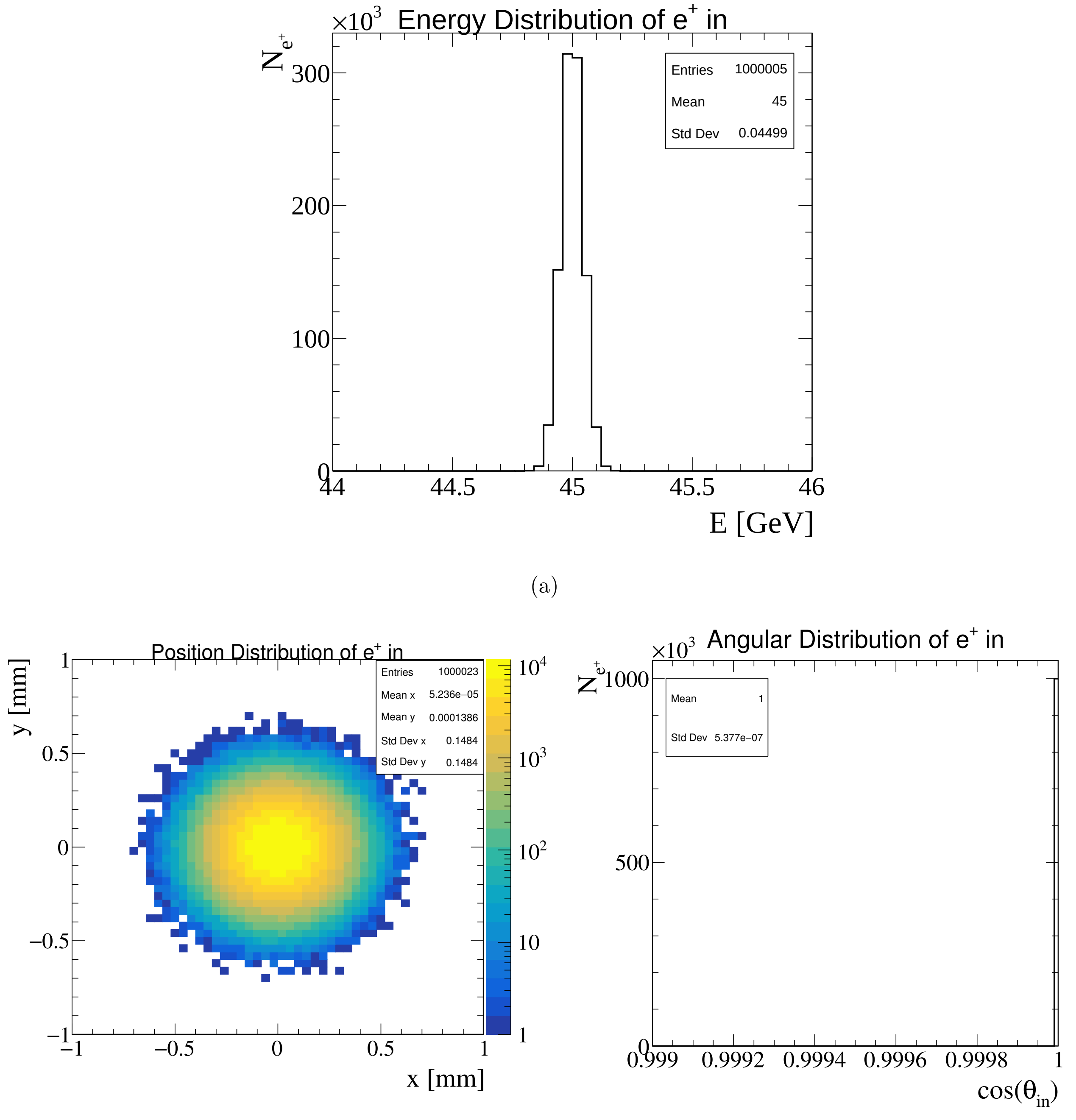

(a)

(b)

(c)

**Figure 3.5:** (a) Energy distribution of the primary beam with an energy spread of 0.1%. (b) Position distribution of the primary positron beam. (c) Angular distribution of the primary positron beam.

How do the beam parameters at different points in the target line change? To answer this question, the following informations have been saved:

- The properties of all particles belonging to the same event (the shot of a 45 GeV positron) are stored. Every time a new particle is produced, or a particle traverses the entrance or the exit of a target (both Be and W), a new instance of the particle is recorded.
- In each instance, the relevant parameters of the particle are recorded at that point: energy, position and momentum, particle type, number of the target, vertex position, time of crossing with respect to a photon going straight, type of process and the parent

ID of the particle (2).

In this way, all distributions at different points can be obtained.

The positrons distributions after the Be target line are shown in Figure 3.6(a), Figure 3.7(a) and Figure 3.7(b).

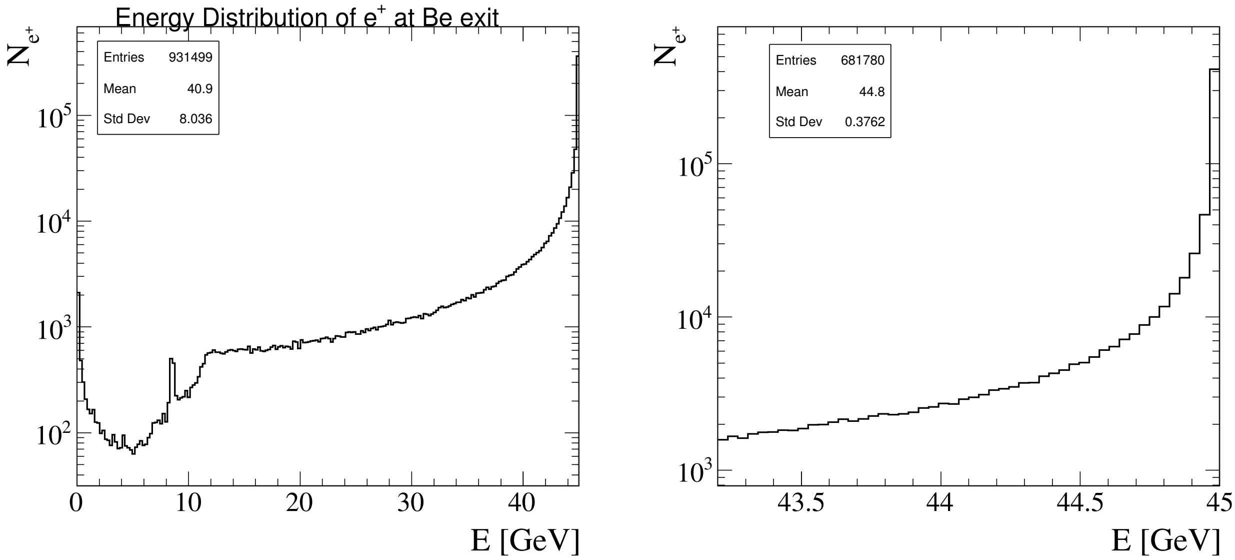

(a)

(b)

**Figure 3.6:** (a) Energy distribution of positrons after the Be target line. (b) Energy distribution of positrons after the Be target line, with the application of an energy cut (E>43.2 GeV, that is 4% of 45 GeV). The number of entries, with respect to that of Figure 3.5(a), allows to evaluate the percentage of positrons that can be recovered in the Positron Ring.

As we have seen considering the muon source schemes, there is the possibility to partially recover the positron beam after the interactions in the beryllium targets. One of the main limitations to this is the energy acceptance of the positron ring. In [14] the parameters of the PR for different emittances have been calculated. In this study, an intermediate energy acceptance of 4% has been considered. To evaluate the number of positrons that can actually be recovered, a selection in energy is applied to the energy distribution, obtaining the result shown in Figure 3.6(b). The number of entries, with respect to that of Figure 3.5(a), allows to evaluate the percentage of positrons that can be recovered in the PR: about 68.2% of initial positrons. This number has been verified also with the introduction of the energy spread, and does not change significantly.

This means that, in order to fully recover the beam, about 30% of the initial positrons have to be produced by the embedded source, or by a combination of the embedded source and the main positron source.

---

(2) In Geant4, each track (which is a snapshot of a particle) has its proper track ID. For instance, the track ID of the primary particle is 1, the track ID of its secondary is 2. The parent ID is the track ID of the parent, therefore it is 0 for the primary particle (which has no parents) and 1 for its secondary (whose parent is the primary). In the case of many secondary tracks, the numeration of the track ID follows the rule of "last in first out". That is, the last produced particle gets the smallest possible track ID.

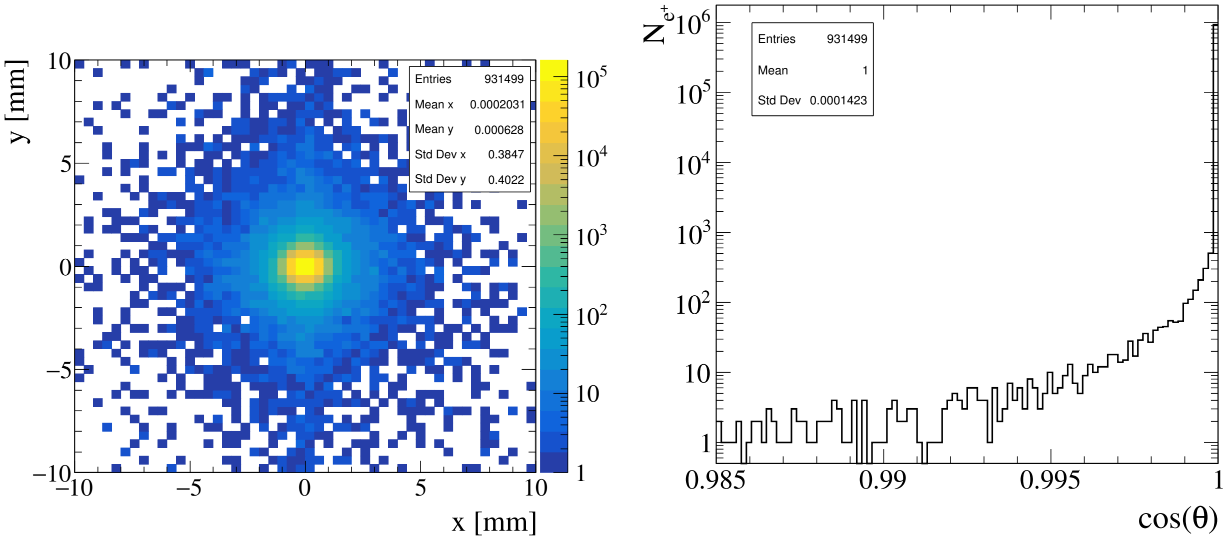

(a)

(b)

**Figure 3.7:** (a) Position distribution of the positron beam after the Be target line. (b) Angular distribution of positrons after the Be target line.

The spread in position and angle of the “used” positron beam can be better understood by considering the comparison of the histograms before and after the beryllium target line. In the case of position, a 1D histogram in the $x$ direction is considered. The difference between position distributions is shown in Figure 3.8(a), while the difference between angular distributions is shown in Figure 3.8(b). The beam spot size (the standard deviation of the position distribution) increases from $\sigma_{\text{spot}} = 0.15$ mm to $\sigma_{\text{spot}} = 0.40$ mm.

At the end of the muon target line, a fraction of the positron beam is composed also by secondary positrons, produced by photon conversion in the Beryllium targets ($\gamma \to e^+e^-$), or by Bhabha scattering ($e^+e^- \to e^+e^-$) with the electrons of the targets.

The contribution of each process to the energy spectrum is shown in Figure 3.9, to be compared with the inclusive energy spectrum, shown in Figure 3.6(a).

The total number of positrons produced by Bhabha scattering is about 600. Hence the efficiency of this process is $6 \cdot 10^{-4}$. Notice that the factor between this efficiency and the muon production efficiency is in agreement with the factor between Bhabha process and positron annihilation into a muon pair cross sections:

$$\frac{\text{eff}_{\text{Bhabha}}}{\text{eff}_{\mu^+\mu^-}} \sim 10^3 \simeq \frac{\sigma_{\text{Bhabha}}}{\sigma_{\mu^+\mu^-}} = \frac{\sim 1\text{ mb}}{\sim 1\ \mu\text{b}} \tag{3.3}$$

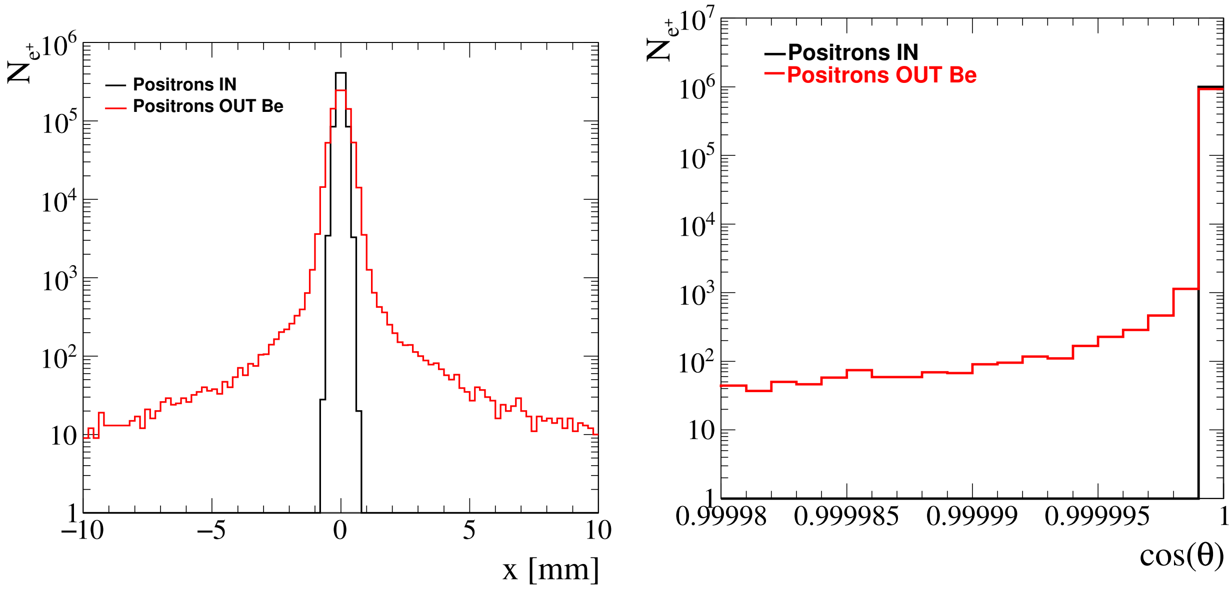

(a) (b)

**Figure 3.8:** (a) Position distribution of the positron beam before (in black) and after (in red) the 0.1 $X_0$ Be target line. The beam spot size (the standard deviation of the position distribution) increases from $\sigma_{\text{spot}} = 0.15$ mm to $\sigma_{\text{spot}} = 0.40$ mm. (c) Angular distribution of positrons before (in black) and after (in red) the Be target line.

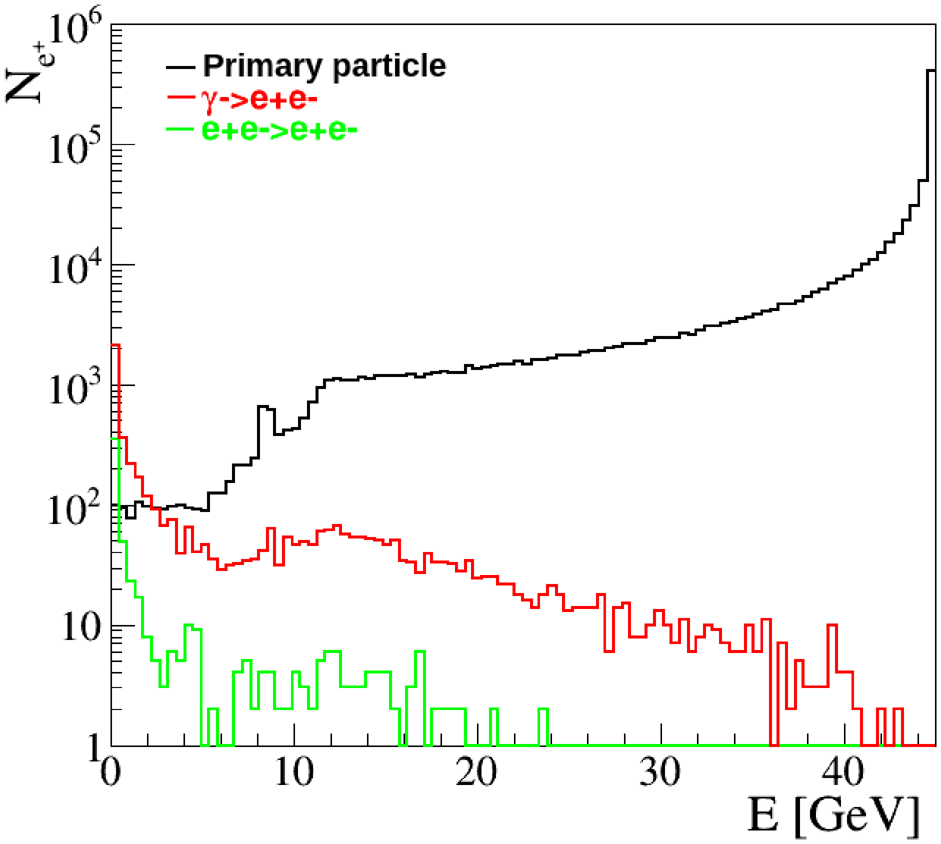

**Figure 3.9:** Energy spectrum of the positron beam at the end of the muon target line. In the legend, the name of the process by which positrons have been created is shown.

## 3.4 Photons

The positron beam produces photons interacting in the Be target line, both by synchrotron radiation in the magnetic quadrupolar field (very low energy photons) and bremsstrahlung in the electromagnetic field of nuclei. Bremsstrahlung photons have the the typical $1/E$ spectrum, and also very energetic photons are produced. In first approximation, the production angle of the first process can be estimated with the formula $\theta_\gamma \simeq \frac{m_e c^2}{p_e c}$ and therefore is very small. Finally, very few photons are produced by positron annihilation with an electron of the target ($e^+e^- \to \gamma\gamma$). The probability of this process is about $10^{-4}$.

The distributions in energy, position and angle of the photon beam at the end of the muon target line are shown in Figure 3.11(a), Figure 3.10(a) and Figure 3.10(b). The beam is highly collimated, and the spot size is of few millimeters. Since the main interest in this study is for the photons able to produce positrons, an energy cut is applied to each distribution to select only the photons above the production threshold (that is 1.2 MeV). In Figure 3.11(b) the distributions of the different processes that create photons are shown. Notice that the cut for $E > 1.2$ MeV, not applied in this case, reduces mainly the synchrotron radiation component of the spectrum.

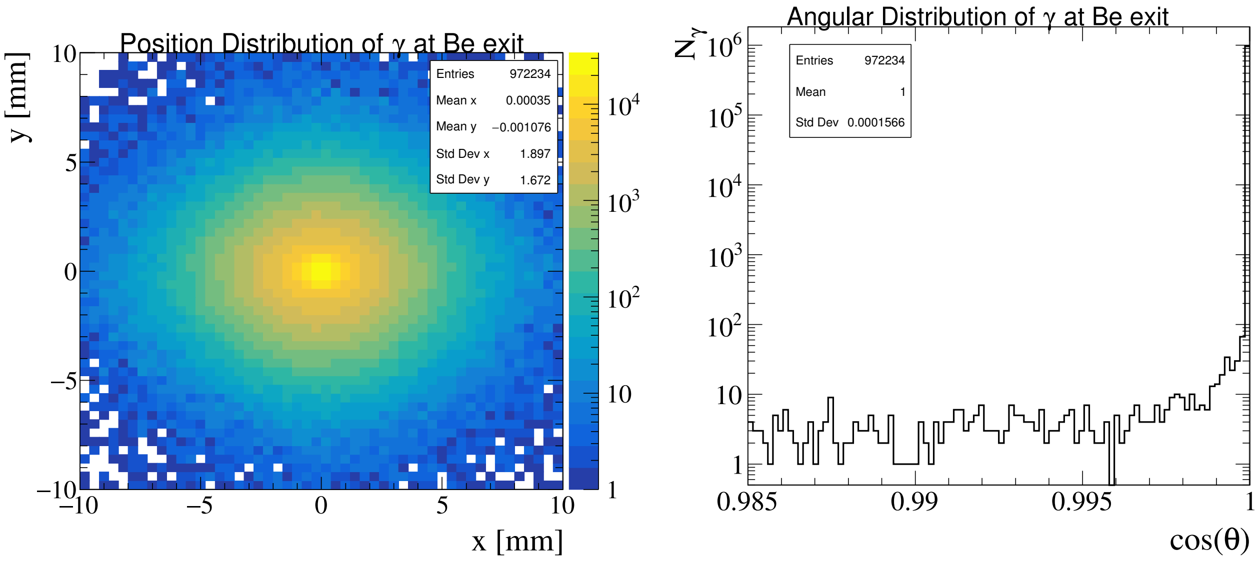

(a) (b)

**Figure 3.10:** (a) Position distribution of the photon beam in the transverse plane, at the end of the muon target line. (b) Angular distribution of the photon beam, at the end of the muon target line. The angle is the one formed between the photon direction and the $z$ axis.

By comparing the number of produced photons with the number of initial positrons, it comes out that about 1 photon above $e^+e^-$ pair production threshold is produced for each 45 GeV positrons (see also Table 3.1).

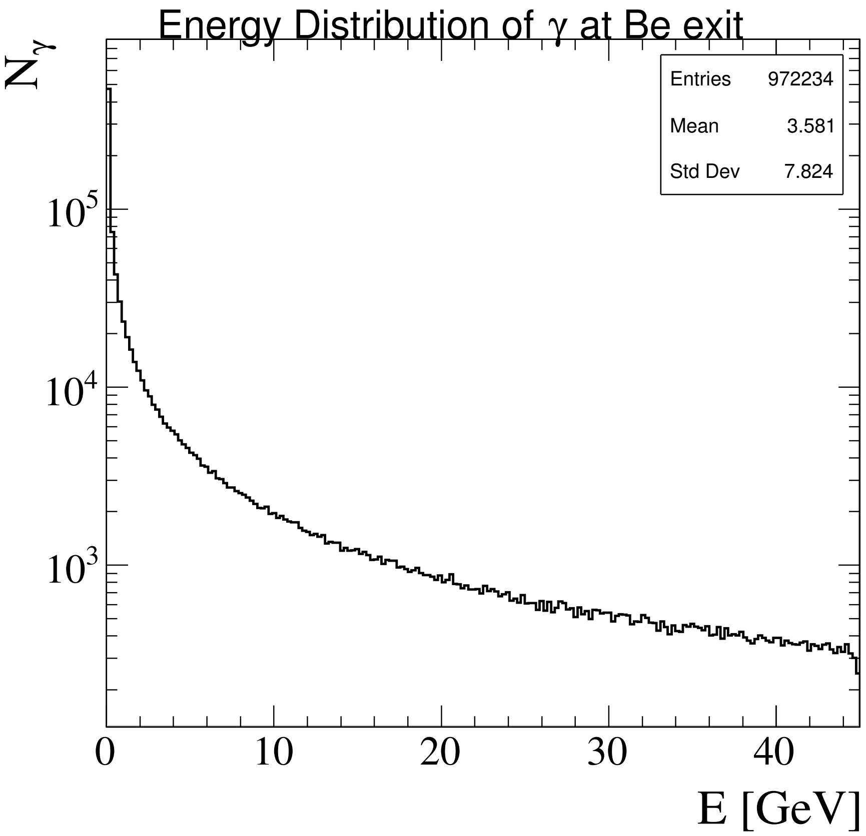

(a)

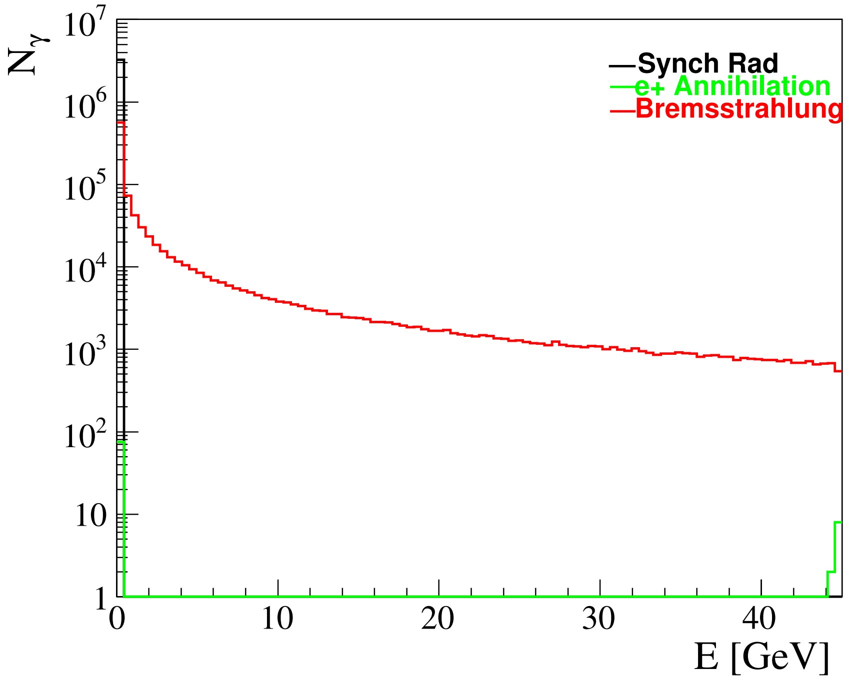

(b)

**Figure 3.11:** (a) Energy distribution of the photon beam exiting the muon target line. A selection for $E > 1.2$ MeV is applied to select only photons above $e^+e^-$ pair production threshold.(b) Energy distribution of the photon beam divided by the process of production of photons.

## 3.5 Electrons

Electrons are also produced by the 45 GeV positron beam. As for the photon beam, electrons of high energy can be used as a positron source, due to the electromagnetic shower they generate in a (heavy) target.

Such high energy electrons can be produced in the muon target line by several processes. The majority of them are produced by ionization of the atoms of the medium (due to the positron energy losses) or, at higher energy, by photon conversion into a $e^+e^-$ pair. Photons can interact also by photoeletric effect or by Compton scattering, releasing energy to the electrons of the target line. Finally, electrons can be produced by Bhabha scattering too.

The distributions in energy, position and angle of the electron beam at the end of the muon target line are shown in Figure 3.13(a), Figure 3.12(a) and Figure 3.12(b). The beam is very collimated, and the spot size is few millimeters wide.

In the energy distribution of Figure 3.13(b), the single processes that produce electrons are shown separately. High energy electrons come mainly from pair production or Bhabha scattering.

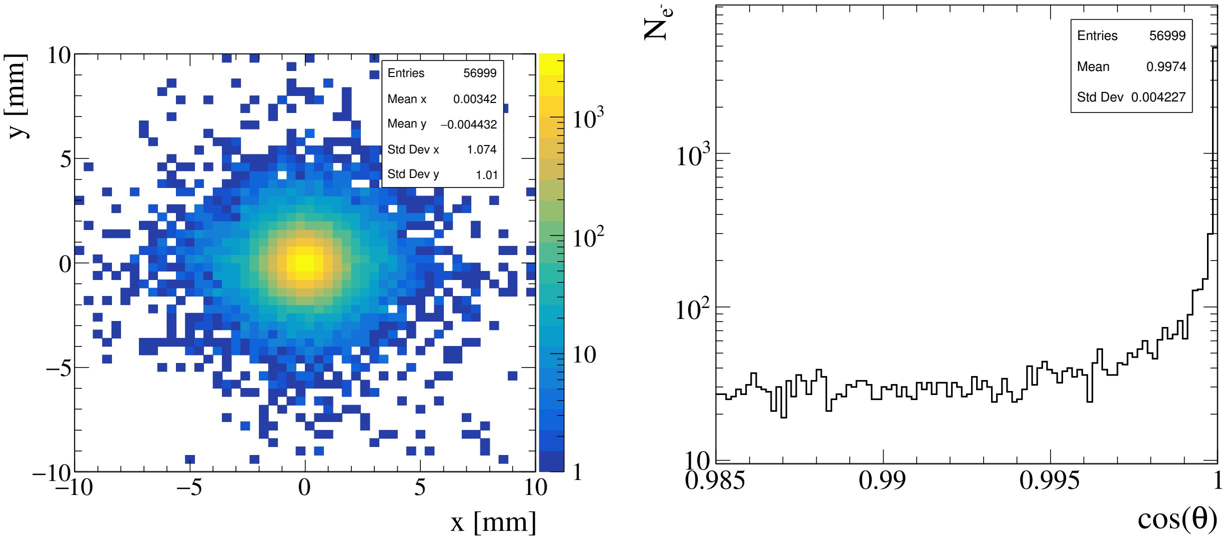

(a)

(b)

**Figure 3.12:** (a) Position distribution of the electron beam in the transverse plane, at the end of the muon target line. (b) Angular distribution of the electron beam, at the end of the muon target line. The angle is the one formed between the electron direction and the $z$ axis.

The number of high energy electrons produced after the muon target line is very small with respect to the number of photons or positrons, since one positron produces only 0.06 electrons (3). It is not practical to separate electrons from positrons of the same energy. Hence, in the case in which also charged particles are used to impinge on the embedded source to produce new positrons, this low number of electrons contributes very little to the positron yield.

---

(3) Even if this number is greater at the entrance of the Tungsten target, due to photons that convert in this length. For instance, after 1 m, the number of electrons is 0.17, but not all of them are at high energy.

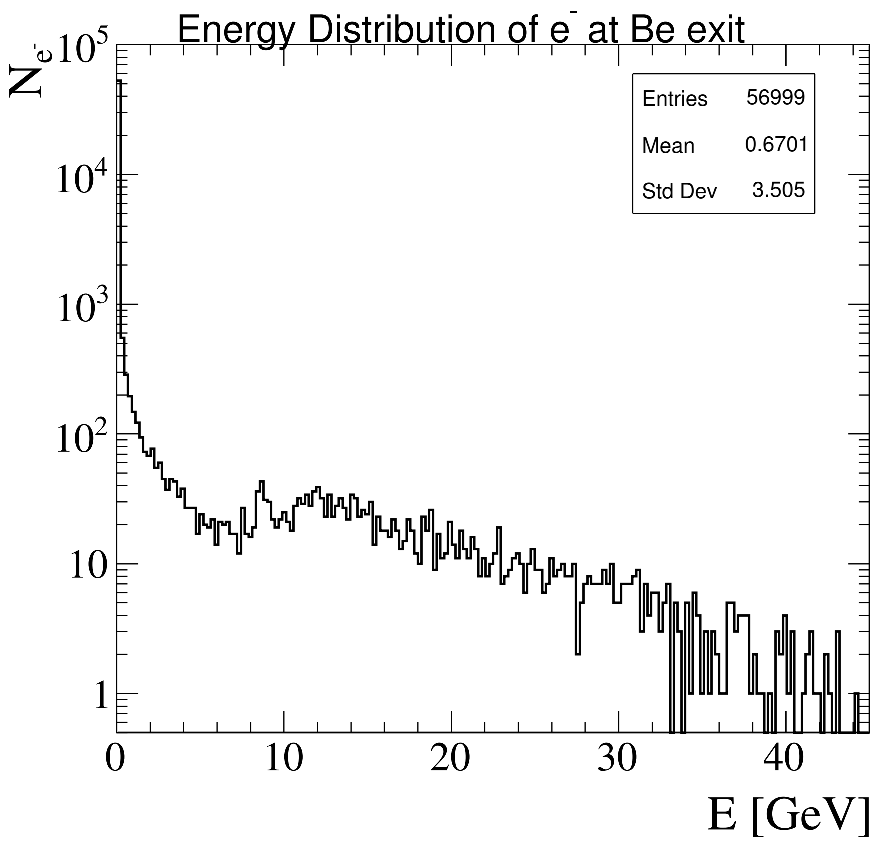

(a)

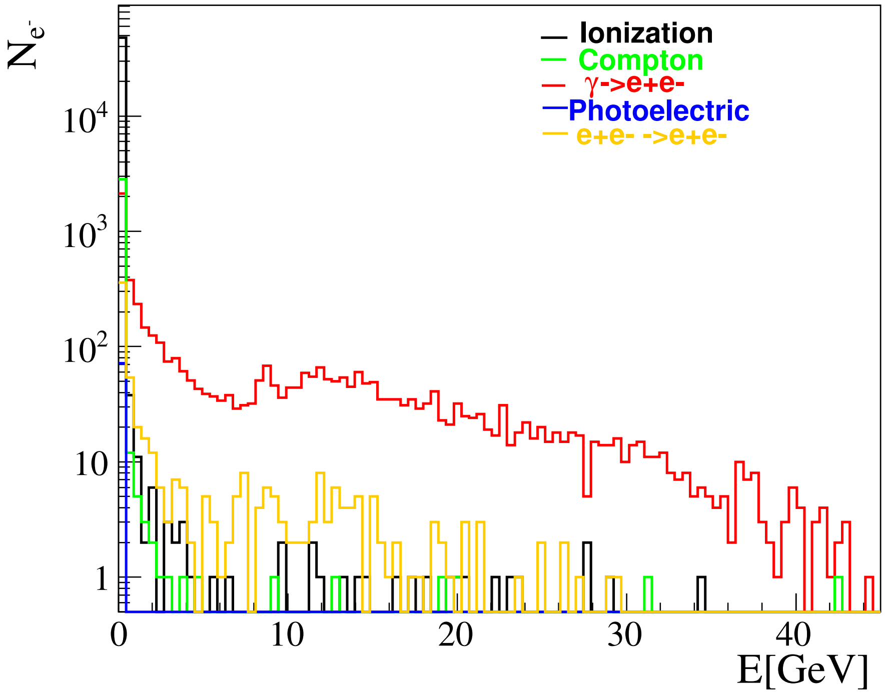

(b)

**Figure 3.13:** (a) Energy distribution of the electrons exiting the muon target line. (b) Energy distribution of the electron beam, where the single processes that produce electrons are shown separately.

## 3.6 Quality of the produced positrons

In the previous section, the number and the characteristics of the particles that reach the regenerator have been presented. In this section, their usefulness regarding the positron regeneration, obtained by the interactions in the tungsten target, will be analysed.

A cylindrical tungsten target has been chosen. The main parameters are the thickness of the tungsten target, measured in multiples of $X_0(\mathrm{W}) = 0.3504\,\mathrm{cm}$, the distance between the end of the target line and the regenerator, namely *zGap*, and the radius of the target. Where not specified, $zGap = 1\,\mathrm{m}$.

The radius must be sufficiently large to intercept all particles in the beam (of photons, positrons or electrons), which distribute in the transverse direction as *zGap* increases. In a preliminary analysis, it has been set at 10 cm, that is large with respect to the beam spot size of few millimeters shown in the previous sections. This is true up to distances of $zGap \sim 100\,\mathrm{m}$, when the size spot is of the order of 1 cm (so the target covers about $10\,\sigma_{\mathrm{spot}}$).

According to the schemes shown in Chapter 2, the number of positrons produced is analysed in two different cases:

- All charged particles are bent away before the tungsten target by a dipole magnet. In the simulation, charged particles are manually killed at tungsten entry (but the operation and the yield with a dipole have been verified, see Section 3.8). The photon beam is not affected, and new positrons are created by photon pair production in the tungsten target. This is the "photons embedded source case".
- There is no bending of charged particles. The photon, electron and positron beams all contribute to the final positron yield by interacting in the tungsten. The great majority of them are produced by high energy positrons, hence this is the "positrons embedded source case".

In both cases, the final yield is obtained by the number of positrons that can be recovered by the collection system. This system can be composed by an AMD (Adiabatic Matching Device), described in Chapter 4, put at the end of the tungsten target, and an accelerating capture section (RF sections immersed in the solenoidal field of the AMD).

The AMD system provides a manipulation in the transverse phase space that consists in a reduction of the angular amplitude (or transverse momentum, since the angle is $\tan^{-1}\frac{p_x}{p_z}$) of the beam, and an increment of the beam spot size, in order to better match the acceptance requirements of the accelerating capture sections, which have a relatively large radial extent but smaller transverse momentum acceptance.

The main role of the RF accelerating section would be to preserve the time structure of the initial positron bunches by accelerating the new positrons to relativistic velocities (say 30-45 MeV) as quickly as possible. In this way, the difference in velocity between different positrons of the bunch are negligible, and the longitudinal phase space spread of the beam is "freezed". Then the beam is ready for the high energy acceleration.

However, after the AMD, the lower longitudinal momentum particles lag in phase because of their smaller longitudinal velocities and their longer (spiral) pathlengths in the AMD [24]. Hence a fast acceleration is not the most convenient thing to do. To understand why, consider Figure 3.14, which represents the longitudinal phase space trajectories of positrons (which can be evaluated as reported in [24]). The horizontal axis is the phase with respect to the accelerating field phase null. The vertical axis is the longitudinal momentum in $m_0c$ units.

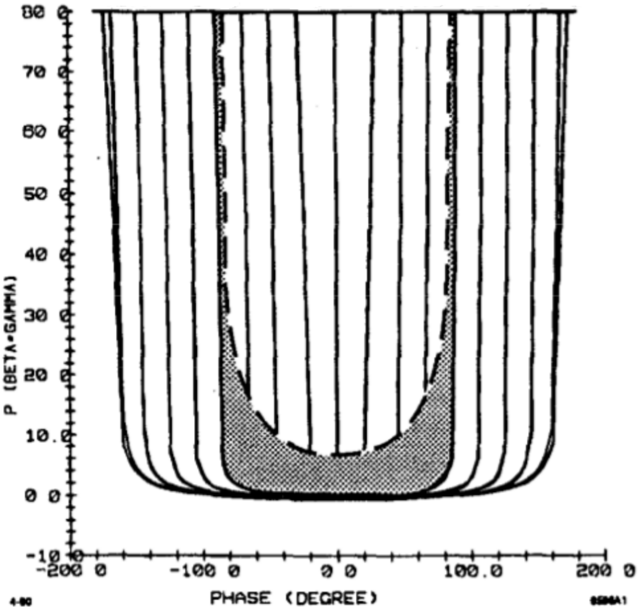

**Figure 3.14:** Longitudinal phase space trajectories of positrons. The horizontal axis is the phase with respect to the accelerating field phase null. The vertical axis is the longitudinal momentum in $m_0c$ units. The shaded area represents the phase space trajectories of positrons with transverse momenta between 0 and $2m_0c$.

Positrons whose positions in phase space are on the right side of the figure (positive phase) are in advance with respect to the wave and are decelerated until they lag in phase enough to drop in the negative phase region, and then are accelerated. In practice, they follow the plotted trajectories clockwise.

Hence, if positrons at AMD exit are accelerated immediately, the resulting final phase space spread is very large, due to the lag in phase of the low longitudinal momentum positrons.

In order to avoid this, the beam is injected in a back-phased, low-gradient accelerating field, that puts the higher energy positrons in a decelerating phase, and the lower energy positrons almost in phase with the electric field (in the null phase region). So most of the high energy positrons are initially decelerated [24]. In this way the beam is “compacted” in the longitudinal phase space. Then, the sinusoidal electric field conduces the beam into an accelerating phase region with a lower phase space spread with respect to a fast acceleration of the whole beam. Finally, the acceleration to relativistic velocities can be performed with lower losses.

The AMD system has been implemented in the simulation only after the embedded source study. Initially the effect of the capture system has been approximated by the following acceptance requirements in the positron phase space, that are typically valid:

- $r < 0.5$ cm. All positrons whose distance from the $z$-axis is greater than 0.5 cm are lost.
- $\theta < 0.5$ rad. If the angle between the positron direction and the $z$-axis is larger than 0.5 rad, the positron is not collected.
- 5 MeV $< E <$ 20 MeV. Only the positron with an energy between 5 and 20 MeV can be collected.

All these requirements select the final positron yield, that is the number of positrons that can actually be recollected and re-injected in the main Positron Ring.

### 3.6.1 Photons embedded source

At the end of the tungsten target, positrons come out with a huge angular spread and a larger spot size. The distributions in energy, angle and position of positrons, with a 2.8 $X_0$ (this number is one of the best compromises between positron yield and deposited power) tungsten target, are shown in Figure 3.15(a), Figure 3.15(b) and Figure 3.16(a). In Figure 3.16(b), the distribution of the transverse momentum components is shown. As expected, the beam is completely symmetric in the $\phi$ direction.

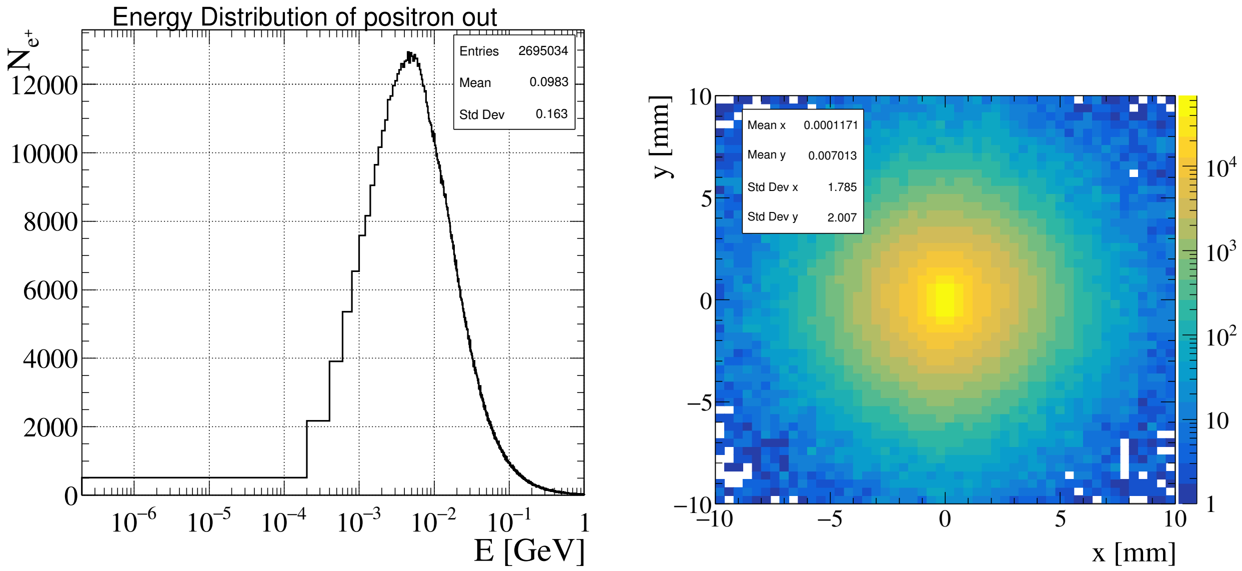

(a) (b)

**Figure 3.15:** (a) Energy distribution of the positrons at the end of the 2.8 $X_0$ tungsten target. (b) Position distribution of the positrons at the end of the 2.8 $X_0$ tungsten target.

The spot size is about four times larger with respect to the positron beam after the target line (see Figure 3.7(a)), and there is a significant fraction of positrons emitted at $\sim 90°$.

The momentum components are normalized to unity, and most of the positrons are emitted with high $p_z \simeq 1$.

The positron yield as a function of the tungsten thickness is reported in Figure 3.17(a), where the effect of each cut (energy, angle and position) on the whole distribution is shown, and in Figure 3.17(b), where the AND of all cuts is reported.

While the requirement on the position seems quite irrelevant, the cuts in angle and in energy reduce considerably the number of final positrons. A maximum is present around $\sim 6\,X_0$.

As has been pointed out in Section 3.3, about 30% of initial positrons have to be recovered in order to fully restore the beam in Positron Ring. This means that the tungsten target thickness has to be greater than $\sim 3\,X_0$, if no other positron source is used (see Figure 3.17(b)). A thickness of 2.8 $X_0$, with a yield of 0.34, satisfies this condition, while a bigger thickness is not an optimal choice because of the high value of the deposited power on the target (see Section 3.7).

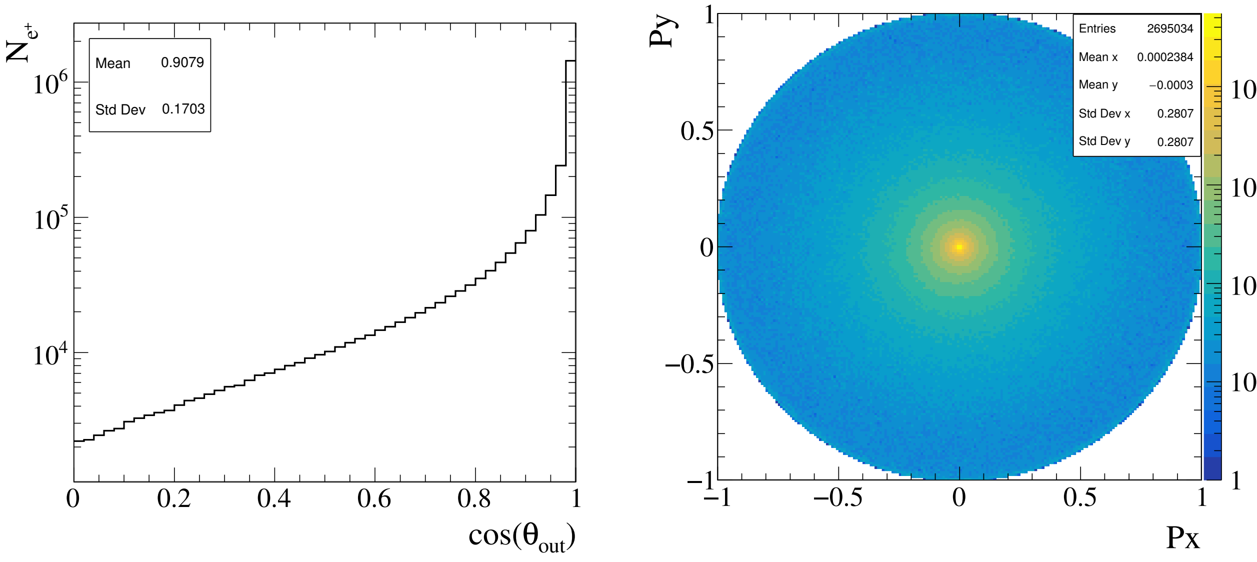

(a)

(b)

**Figure 3.16:** (a) Angular distribution of the positrons at the end of the 2.8 $X_0$ tungsten target. (b) Distribution of the momentum transverse components is shown.

In the previous results, the target has been set at a distance from the target line $zGap = 1\,\mathrm{m}$. In Figure 3.18(a), an analysis of the positron yield as a function of the distance, with a fixed tungsten target of 2.8 $X_0$, is shown. As $zGap$ increases, the beam spot size (of the photon beam in this case) increases as well. Even if the tungsten target is large enough to intercept all the photons, the spread in angle, position and energy of the photon beam increases, and the same happens to the positron beam after the tungsten. However, the capture system is always the same, hence the positron yield decreases. This happens at a distance of about 20 meters. Before this distance, the positron yield is quite constant.

The dominant effect is the increase of the position spread of the produced positrons, due to the growth of the beam spot size of the photons. This is clear in Figure 3.18(b), where the effect of each requirement is shown. The requirement on the position becomes the most relevant one. This is important in the PEDD analysis (Section 3.7). To increase the positron yield without increasing the tungsten thickness (this will result also in an increment of deposited power and PEDD), it would be very important to improve the requirement on the position. To do this with an AMD, as explained in Chapter 4, one could increase the iris of the accelerating system, or the value $B_S/B_0$, where $B_S$ is the constant field of the solenoid where the AMD is immersed, and $B_0$ the peak field of the AMD.

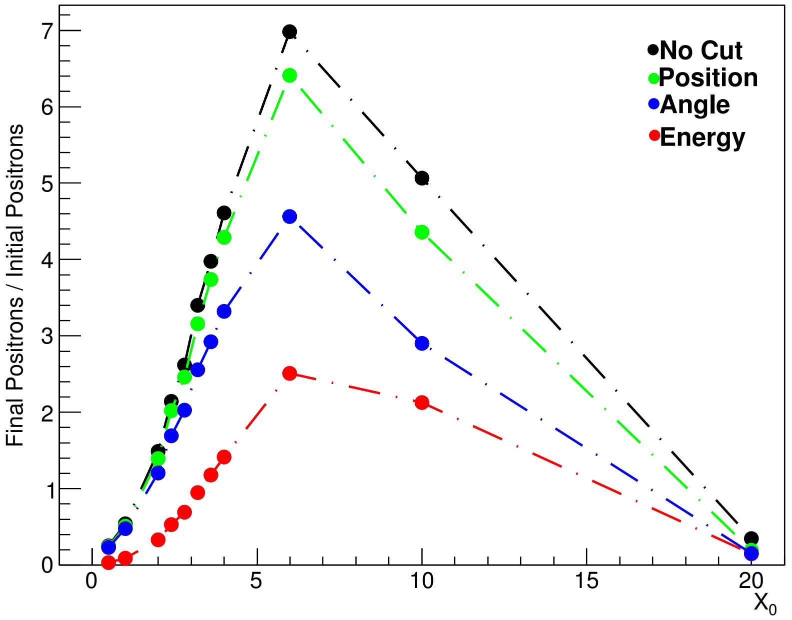

(a)

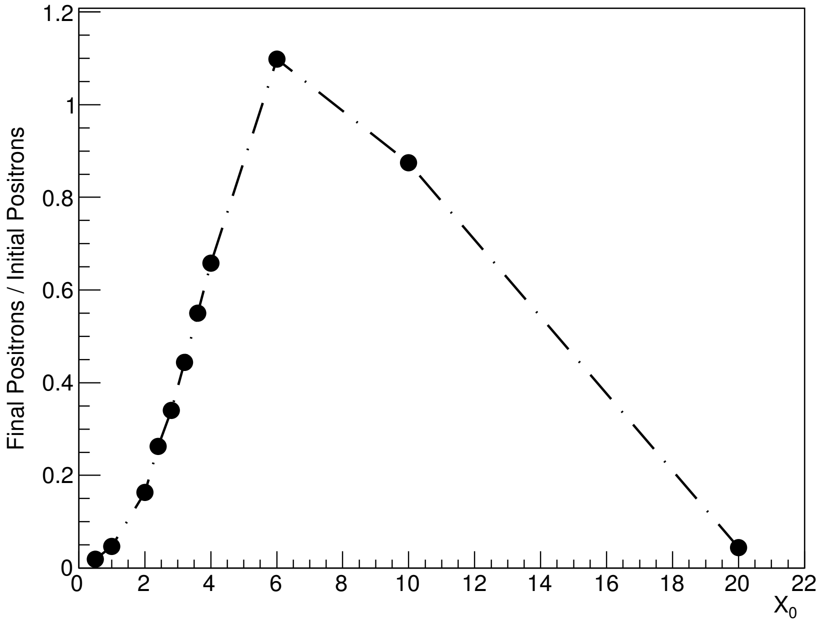

(b)

**Figure 3.17:** (a) Positron yield (fraction of final positrons with respect to the initial positrons) as a function of the tungsten thickness, measured in $X_0$. The effect of each cut on the whole distribution is shown. (b) Positron yield (fraction of final positrons with respect to the initial positrons) as a function of the tungsten thickness, measured in $X_0$. The AND of all cuts is shown.

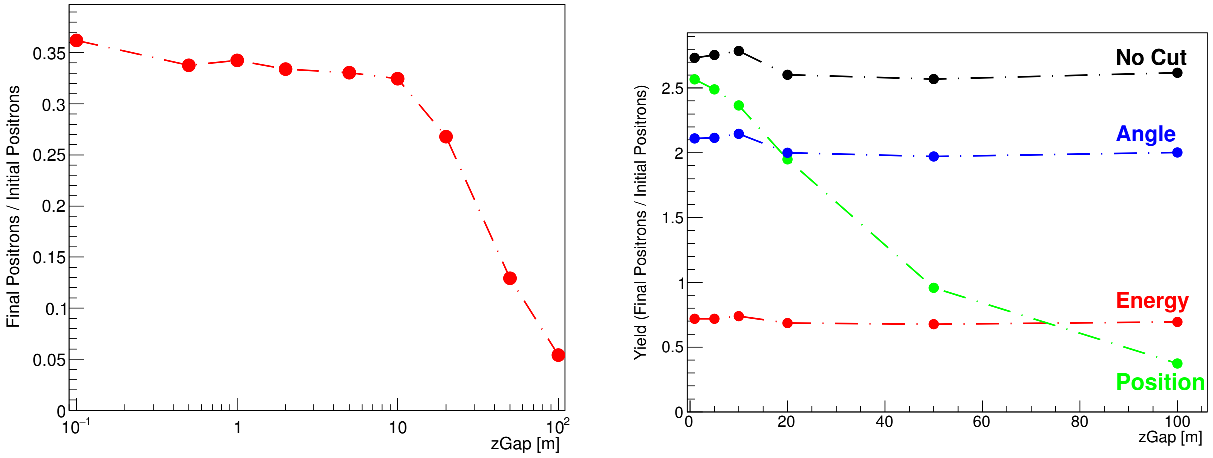

(a) (b)

**Figure 3.18:** (a) Positron yield as a function of *zGap*, the distance between the Be target line and the tungsten target. The tungsten thickness is 2.8 $X_0$. The AND of all cuts is shown. (b) The effect of each cut on the yield is shown. As the distance increases, the main effect is the growth of the beam spot size, hence of the position spread of the final positron beam. So the position cut becomes the most relevant one.

A summary table, normalized to 100 initial positrons, is shown in Table 3.1. The values are referred to a tungsten target of 2.8 $X_0$ at a distance $zGap = 1$ m.

**Table 3.1:** Summary table for the positron yield of the photons embedded source, normalized to 100 initial positrons.

| **Photons embedded source** | | |
|---|---|---|
| Yield (2.8 $X_0$) | Particle | # |
| Primary particles | $e^+$ | 100 |
| Primary lost after Be target line | $e^+$ | 31.8 |
| Entering Tungsten | $\gamma$ ($E > 1.2$ MeV) | 97.1 |
| Exiting Tungsten | $e^+$ | 270 |
| Exiting Tungsten (All Cuts) | $e^+$ | 33.9 |

### 3.6.2 Positrons embedded source

In the scheme shown in Figure 2.9(b), the possibility of avoiding the recovery of initial positrons is taken into account. In this case, all these positrons can be used to impinge on the tungsten target and produce new positrons, giving to a positrons embedded source. Also electrons and photons contribute to generate new positrons by interacting in the material. Hence more positrons are produced with respect to the photons embedded source. However, in order to fully recover the initial positron beam with the embedded source only, 100% of initial positrons must be collected after the tungsten target.

The distributions in energy, angle and position of positrons, with a 1.8 $X_0$ (this number is one of the best compromises between positron yield and deposited power) tungsten target, are shown in Figure 3.19(a), Figure 3.19(b) and Figure 3.19(c). In Figure 3.19(d), the distribution of the transverse components of the momentum of positrons is shown. As expected, the beam is completely symmetric in the $\phi$ direction.

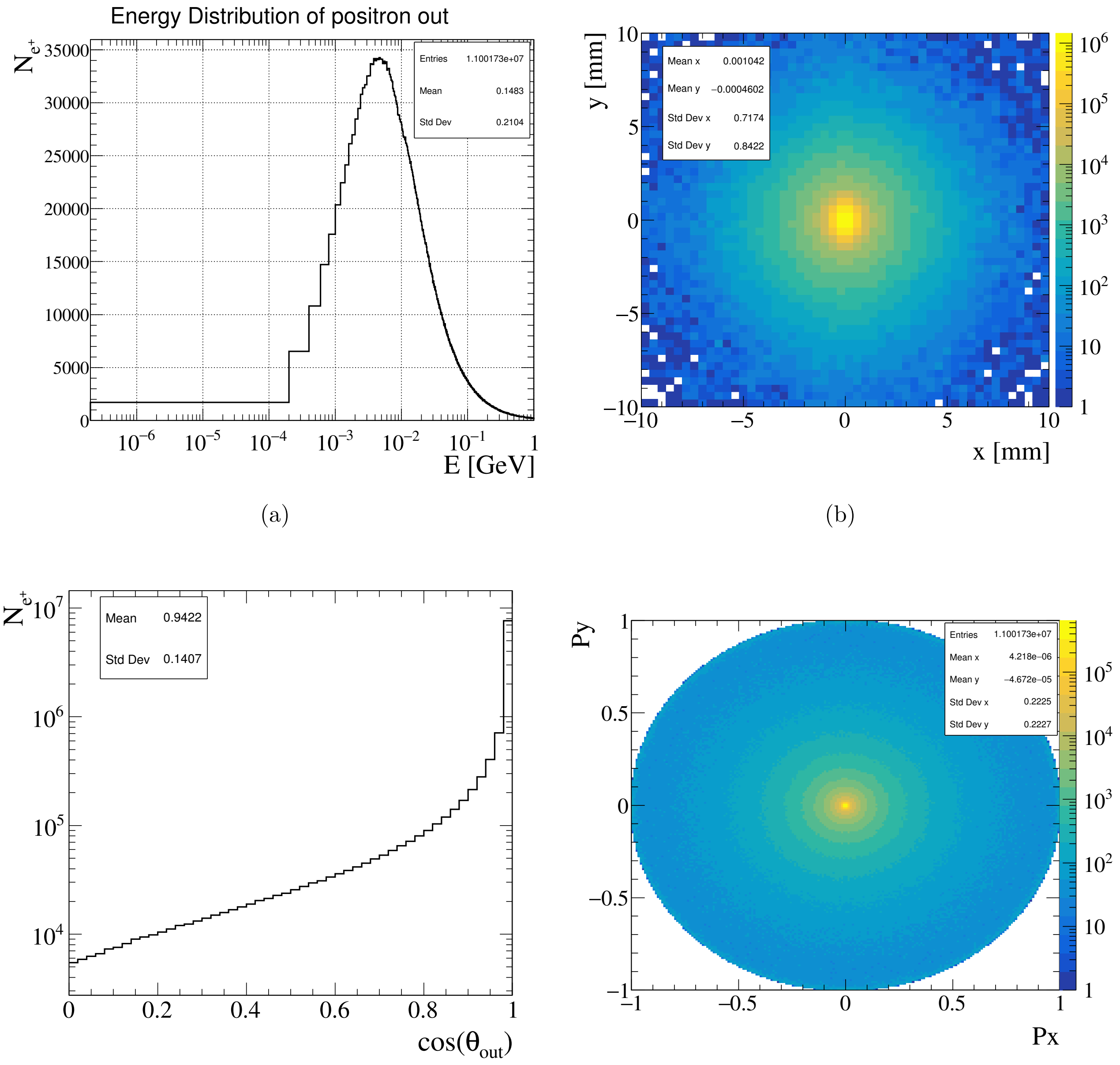

(a)

(b)

(c)

(d)

**Figure 3.19:** (a) Energy distribution of the positrons at the end of the 1.8 $X_0$ tungsten target, for a positrons embedded source. (b) Position distribution of the positrons at the end of the 1.8 $X_0$ tungsten target, for a positrons embedded source. (c) Angular distribution of the positrons at the end of the 1.8 $X_0$ tungsten target, for a positrons embedded source. (d) Distribution of the transverse component of the positron momentum.

Here the spot size is about two times smaller than in the photon case, since positrons start in a collimated beam. Also the angular spread is a bit smaller.

The positron yield as a function of the tungsten thickness is reported in Figure 3.20(a), where the effect of each requirement (energy, angle and position) on the whole distribution is shown, and in Figure 3.20(b), where the AND of all cuts is shown.

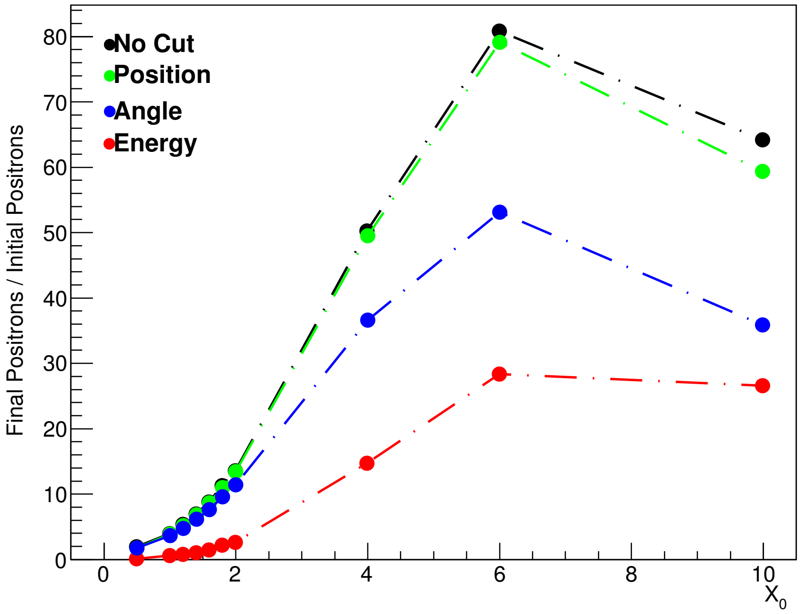

(a)

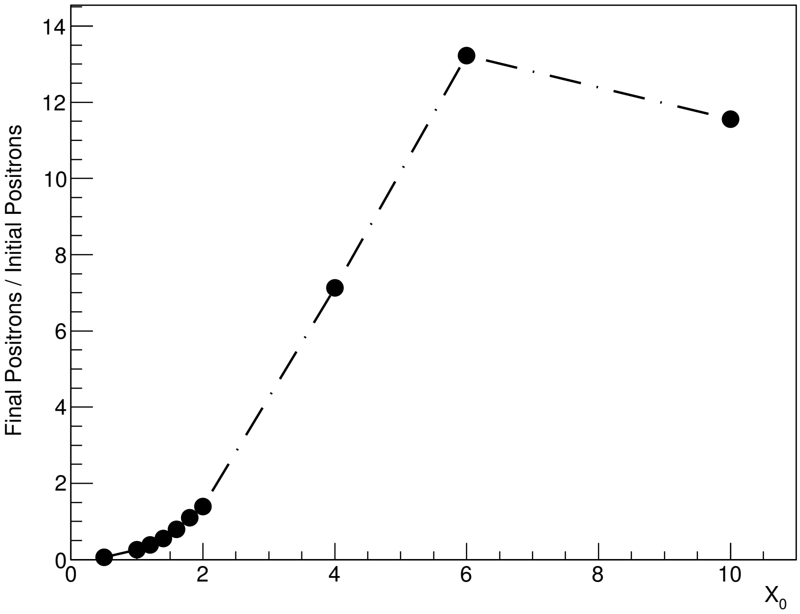

(b)

**Figure 3.20:** (a) Positron yield (fraction of the positrons at tungsten's exit that satisfy the given selection with respect to the initial positrons) as a function of the tungsten thickness, measured in $X_0$, for a positrons embedded source. The effect of each selection on the whole distribution is shown. (b) Positron yield (fraction of the positrons at tungsten's exit that satisfy all selections with respect to the initial positrons) as a function of the tungsten thickness, measured in $X_0$, for a positrons embedded source. The AND of all selection is shown.

As in the photon case, a maximum is reached around $\sim 6\,X_0$.

Since the initial positron beam is totally lost in this case, in order to fully recover the positrons (and to have the positrons yield $> 1$), the tungsten target thickness has to be greater than $\sim 2\,X_0$, if no other positron source is used. A thickness of 1.8 $X_0$, with a yield of 1.09 positrons for each incident positron, satisfies this condition.

A summary table for the positron yield in the positrons embedded source case is shown in Table 3.2. Concerning electrons, in first approximation only those able to produce above-threshold photons can produce positrons. According to Rossi model [25], in 1 $X_0$ an electron of 2.4 MeV can produce by bremsstrahlung a photon of 1.2 MeV, above threshold. Hence the number of electrons above 2.4 MeV, that in first approximation is the number of electrons that can produce positrons, is reported in the table. As mentioned before, only very few electrons have these energy. Values are referred to a tungsten target of 1.8 $X_0$ at a distance $zGap = 1\,\text{m}$.

**Table 3.2:** Summary table for the positron yield of the positrons embedded source, normalized to 100 initial positrons.

**Positrons embedded source**

| Yield (1.8 $X_0$) | Particle | # |
|---|---|---|
| Primary particles | $e^+$ | 100 |
| Primary lost after Be target line | $e^+$ | 100 |
| Entering Tungsten | $e^-$ | 17.6 |
| Entering Tungsten | $e^-$ ($E > 2.4\,\text{MeV}$) | 0.67 |
| Entering Tungsten | $e^+$ | 103 |
| Entering Tungsten | $\gamma$ ($E > 1.2\,\text{MeV}$) | 97.1 |
| Exiting Tungsten | $e^+$ | 1100 |
| Exiting Tungsten (All Cuts) | $e^+$ | 107 |

## 3.7 Deposited power in the embedded source

Tungsten is an high-$Z$ material ($Z = 74$), hence the electromagnetic interactions in the field of the nuclei, as bremsstrahlung and pair production and multiple Coulomb scattering, being proportional to $Z^2$, are enhanced. Moreover, electrons and positrons have an average energy much above the critical energy (see Figure 3.13(a) and Figure 3.6(a)), that for tungsten is $E_c \sim 8$ MeV, so they interact mainly via bremsstrahlung. Photons have an average energy $\sim 4$ GeV (Figure 3.11(a)). At this energy, the fraction of pair production cross section above the Compton cross section is around $10^3$ [26], hence they interact mainly via pair production.

An electromagnetic shower develops in the material, and energy is released by secondary particles. The energy release in the target depends on the containment (lateral and longitudinal) of the material, and it is calculated by Geant in two ways:

- Recording the release of energy in the whole target step by step. For each event (shot of one 45 GeV positron), the sum of the energy released in each step is recorded. Then the energy deposited in each event is summed up during the run. The average value of the deposited energy per incident positron is then obtained by dividing the energy deposited in the run by the number of initial positrons.

- Dividing the target in slices, using Geant4 mesh scoring option. The energy deposited in each slice in the full run is recorded, it can be summed up and geometrical considerations on energy deposition are possible. Two different types of mesh, a cubic mesh and a cylindrical mesh, are used.

Then, the deposited power can be evaluated by considering the timing informations of the positron bunches. As reported in Section 2.2, a possible set of values considered by LEMMA is 1000 bunches of $5 \cdot 10^{11}$ $e^+$/bunch, at a 10 Hz repetition rate. This means an average rate of initial positrons of $5 \cdot 10^{15}$ $e^+$/s. By multiplying this number by the energy deposited by the produced photons per initial positron (provided by the simulation through the methods described above), the deposited power can be evaluated.

The deposited power is important to understand if the target can sustain the amount of energy deposited. However, the target destruction is mostly caused by the thermal gradient difference due to the pulsed irradiation of this intense source of positrons. Such kind of target damage has been experienced at SLAC [27]. After a series of experiments, the Peak Energy Deposition Density (PEDD) has been described as the parameter to evaluate the safety regions in the parameter space of the target, and to determine the incident beam spot size to avoid the target damage (in fact, as will be clear later, the PEDD is directly related to the spot size of the incident beam). The threshold value of the PEDD for tungsten is about 35 J/g [28].

The PEDD is evaluated by dividing the target in a cylindrical mesh, coaxial with the incident beams. Following the observation made in [29], the mesh covers a radius $R = 4\sigma$, where $\sigma$ is the spot size of the incident beam. In this way, more than 99.9% of the particles impinge directly on the mesh. The cylinder is sliced into disks of thickness $dz = 0.25\,X_0$ (since a typical thickness is 1 cm, this corresponds to about 12 divisions in $z$-direction). Each disk is divided in circles of uniformly increasing radii into 50 parts - one internal disk (altogether, such disks form the internal cylinder in the $z$-direction) and 49 rings. Hence the radial step is $dr = 0.02R$. No division is applied in the $\phi$ direction. A graphical representation is given in Figure 3.21.

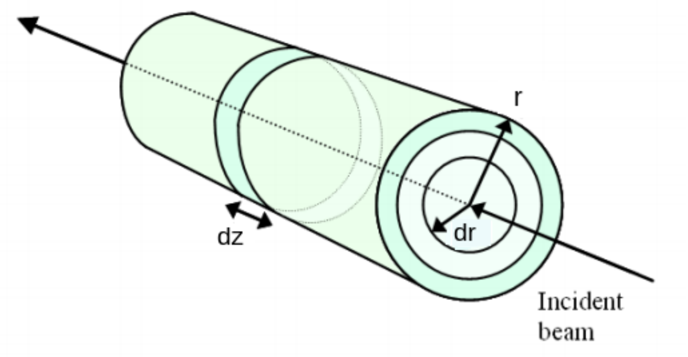

**Figure 3.21:** Graphical representation of the mesh division in the cylinder.

The number of initial positrons has been chosen in order to avoid under-populated bins in the mesh. In particular, assuming Poisson fluctuations of the number of particles that release energy in the bin, the number of entries in each bin must be greater that $\sim 100$. In this way, this number would never fluctuate to 0 by poisson fluctuations, since 100 is at $10\sigma$ from 0.

The EDD (Energy Density Deposition) is obtained by:

$$\mathrm{EDD}(n) = \frac{E_{\mathrm{dep}}}{V(n)\rho_{\mathrm{W}}} \tag{3.4}$$

where $E_{\mathrm{dep}}$ is the energy deposited in the volume $n$, $\rho_{\mathrm{W}} = 19.30$ g/cm$^3$ is the tungsten density, and $V(n) = \pi dz dr^2(2n+1)$ is the volume of the $n$-th cylindrical crown, starting from the center. The first volume, with $n = 0$, is the cylinder in the middle, and the last one, with $n = 49$ is the cylindrical ring at the perimeter of the mesh.

The PEDD corresponds to the maximum EDD value. Usually, this happens in the cylinder at the center and the end of the target, where the shower development reaches its maximum [29].

The beam spot size is one of the key parameters that determine the PEDD [30]. When it increases, the beam is more “diffused”, hence also the density of energy deposited in the target is reduced, and it is spread over a wider region of the target. An easy way to increment the beam spot size is by increasing the distance *zGap*. The farther the tungsten target is positioned, the more the beam spot size increases, because of the initial momentum spread. When this happens, also the number of entries in each bin of the mesh is reduced, so the number of events is increased in order to have enough statistics.

A check for PEDD variation has been done by increasing the statistics and the number of bins. The results that are shown farther are obtained with $N_{e^+} = 10^4$ (that is $10^4$ initial positrons) and with the mesh division described earlier (50 bins in $r$-direction, 12 in $z$-direction). By increasing the statistics to $10^5$ (with the same division) or $10^6$ (with 100 bins in $r$-direction and 24 in $z$-direction), the maximum variations from the configuration $10^4$, (50,12) are $\sim 2\%$. Hence the chosen configuration is a good compromise between accuracy and computation time.

The deposited power and the PEDD are analysed in the photons and positrons embedded source cases.

### 3.7.1 Photons embedded source

The deposited power as a function of $X_0$, for a photons embedded source is shown in Figure 3.22(a). Values are obtained introducing a cubic mesh in the target and evaluating the cumulative along $z$. So, the value at 1 $X_0$ is the sum of the power deposited in the target from $z = 0$ to $z = 1\,X_0$. The tungsten target is positioned at a distance of 1 m from the Beryllium target line. A primary positron beam with a rate of $5 \cdot 10^{15}$ $e^+/s$ is considered. The rate of photons is almost the same, due to the number of photons produced per initial positron (see Table 3.1). Reasonable values for the total deposited power are around 35 kW, however the key factor in order to avoid target destruction is the PEDD.

In Figure 3.22(b), the positron yield (given by the AND of all selections) as a function of the deposited power, for different tungsten thickness (from 0.5 to 4 $X_0$), is figured. In order to satisfy the 0.3 yield requirement, one can use a 2.8 $X_0$ tungsten target with a deposited power around 70 kW.

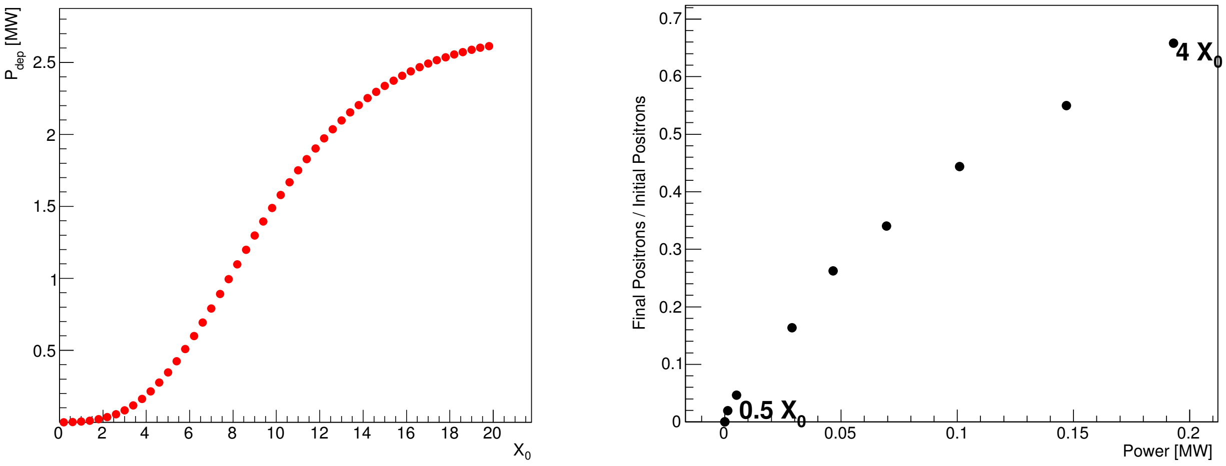

(a) (b)

**Figure 3.22:** (a) Deposited power in tungsten, as a function of the thickness, when the source is the photon beam. (b) Positron Yield (given by the AND of all selections) as a function of the deposited power, in the photon embedded source case.

The energy is not deposited homogeneously along the target. To locate the regions in which the deposit is larger, the energy deposited in each bin has been recorded as an entry of a 3D histogram. In order to better understand the result, a projection of this histogram in the $x - z$ plane has been done. The result is shown in Figure 3.23.

Obviously, the energy deposit is larger in the central region of the target, and increases in the $z$-direction due to the shower development. After a certain length, that in this case is around 4 cm (11.4 $X_0$), the shower development stops, because the energy of the particles in the shower, in average, is around the critical energy, and the deposited energy decreases. According to the simplest model of the electromagnetic shower, the average energy of the secondary particles is around $E(x/X_0) = E_0/2^{x/X_0}$. Starting with an average energy of the photon beam $\sim 4$ GeV, after $11\,X_0$ the average energy of the secondary particles is $\sim 2$ MeV, that is below the critical energy. Hence the multiplication process is statistically terminated after this radiation length.

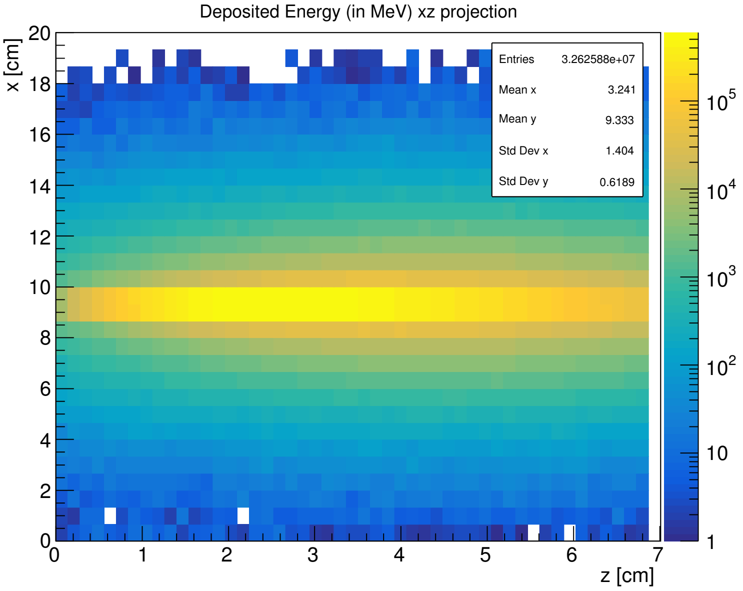

**Figure 3.23:** Projection in the $x - z$ plane of the histogram in which the deposit of energy is recorded. The beam comes from the left.

The PEDD and the positron yield (given by the AND of all selections) as a function of the beam spot size is shown in Figure 3.24. The values of PEDD are normalized to one incident positron. To obtain the final number, this value has to be multiplied by the number of positrons per pulse. Notice that as a result of the growth of the beam spot size, while the PEDD decreases, the total power deposited in the tungsten remains quite constant. This is shown in Figure 3.25.

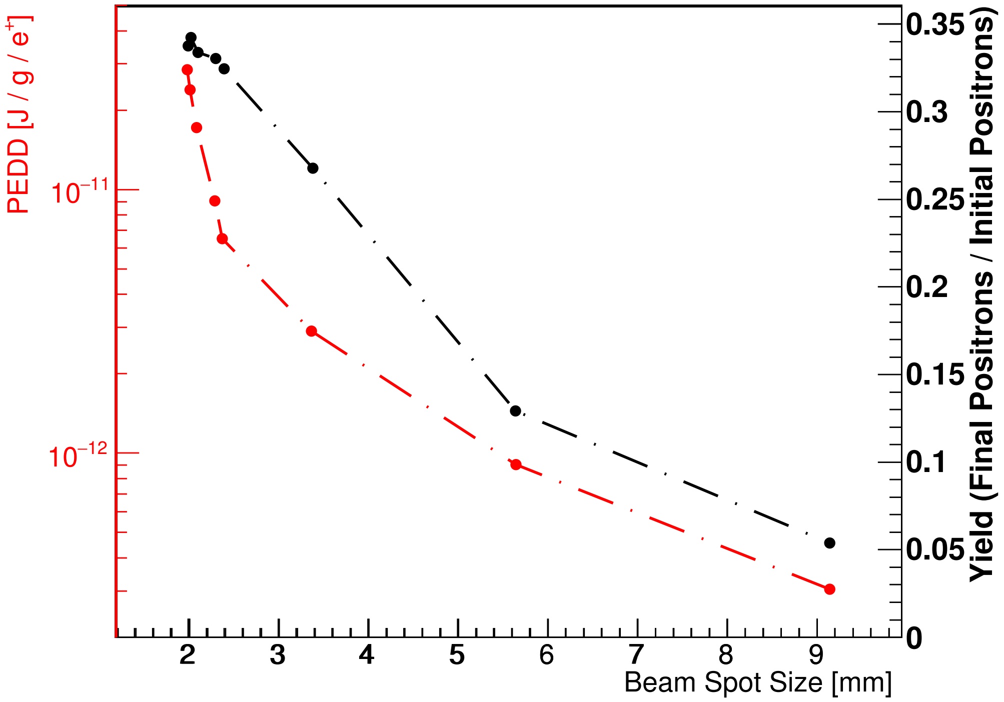

**Figure 3.24:** PEDD (Peak Energy Deposition Density) and positron yield (given by the AND of all selections) as a function of the beam spot size, in the photon embedded source case, for a 2.8 $X_0$ tungsten target.

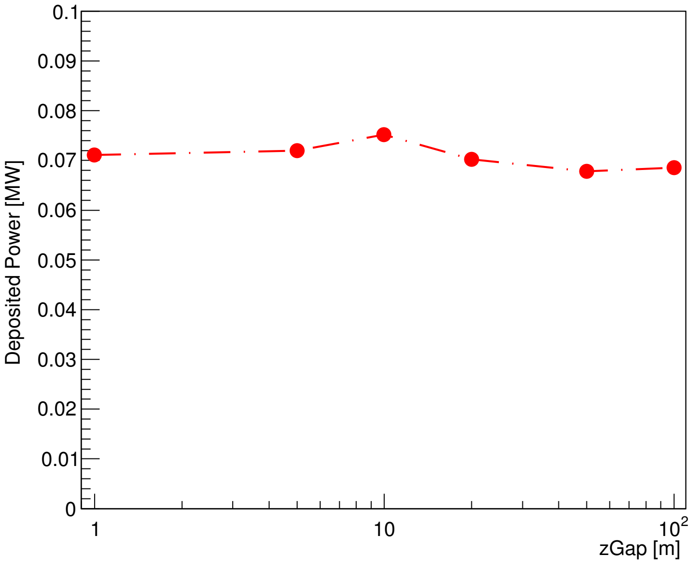

**Figure 3.25:** Power deposited in the whole target as a function of the distance. While the PEDD decreases, the total deposited power stays quite constant.

As the beam spot size increases, the energy density decreases, since energy is distributed in a larger region. To show this, the projection of the histogram of energies in the plane $x - z$ is shown for different beam spot size. In Figure 3.26(a) the beam spot size is 2.016 mm, and in Figure 3.26(b) it is 3.373 mm (4), while the distance *zGap* increments from 1 m to 20 m.

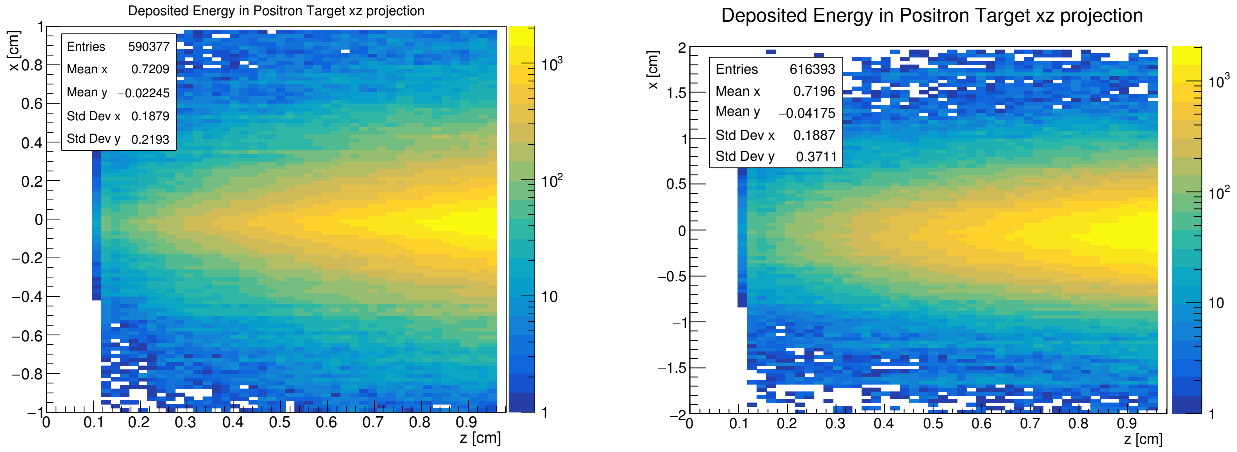

(a)

(b)

**Figure 3.26:** (a) Deposited energy in the $x-z$ plane (projection of a 3D histo). The distance between the target line and the tungsten is 1 m, and the spot size of the photon beam 2.016 mm. (b) Deposited energy in the $x-z$ plane (projection of a 3D histo). The distance between the target line and the tungsten is 20 m, and the spot size of the photon beam 3.373 mm.

Values are in MeV for $10^4$ positrons in the primary beam. Notice that the region of highest energy deposition spreads on a larger distance in the second case (see the standard deviation on $y$). Moreover, the $y$ standard deviation is of the order of the beam spot size. Then, the highest values are reached at the target's end point in both cases.

In the following figures, some "geometric" considerations about the energy density deposition are given. In Figure 3.27, the EDD of the last $z$-slice of the mesh is shown for $\sigma_{\text{spot}} = 3.373\,\text{mm}$. In this case, a box mesh has been used. The EDD distribution in the radial direction follows a gaussian with a standard deviation of the order of the beam spot size.

Projections along $r$ for $zGap = 1\text{m}$ and $zGap = 20\text{m}$, are shown respectively in Figure 3.28(a) and Figure 3.28(b) (in this case the cylindrical mesh is used). It can be seen clearly how in the second plot the energy density is distributed in a larger region, with a maximum value that is about ten times lower. The EDD is maximum along the $z$-axis (near the center of the cylinder), and goes to zero at $\sim 4\sigma_{\text{spot}}$ from the center.

In Figure 3.29(a) and Figure 3.29(b) the EDD as a function of the $z$ depth, measured in $X_0$, is shown, for the cylinders at the center of the mesh (in this case the cylindrical mesh is used). As before, the comparison between $zGap = 1$ m and $zGap = 20$ m is shown. The EDD along z increases until the maximum value is reached at end of the target. This value is smaller for a larger beam spot size, as expected, and is in agreement with the maximum values of the previous plots.

---

(4) Values of the beam spot size are obtained by the average value of the beam spot sizes on $x$ and $y$ directions.

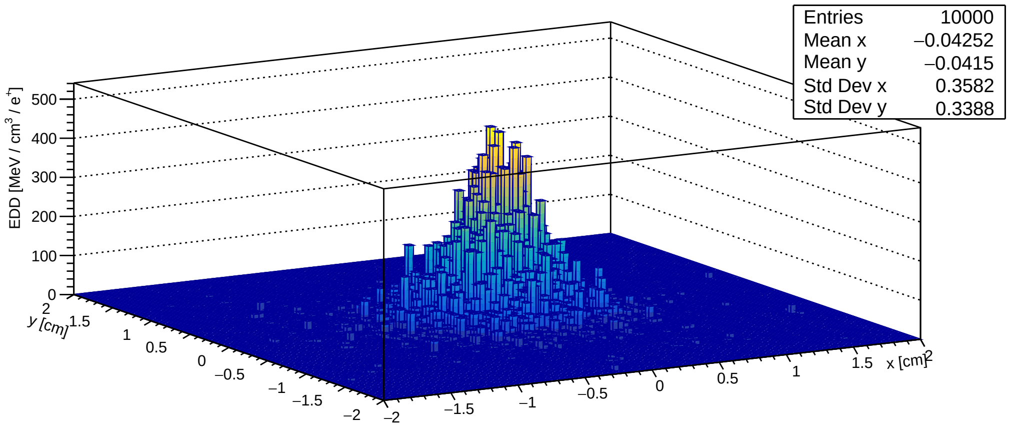

**Figure 3.27:** Histogram of the EDD (Energy Deposition Density) for the slice of the mesh at the end of the tungsten target. The maximum value is around 500 $\mathrm{MeV/cm^3/e^+}$. $\sigma_{\text{spot}} = 3.373\,\mathrm{mm}$.

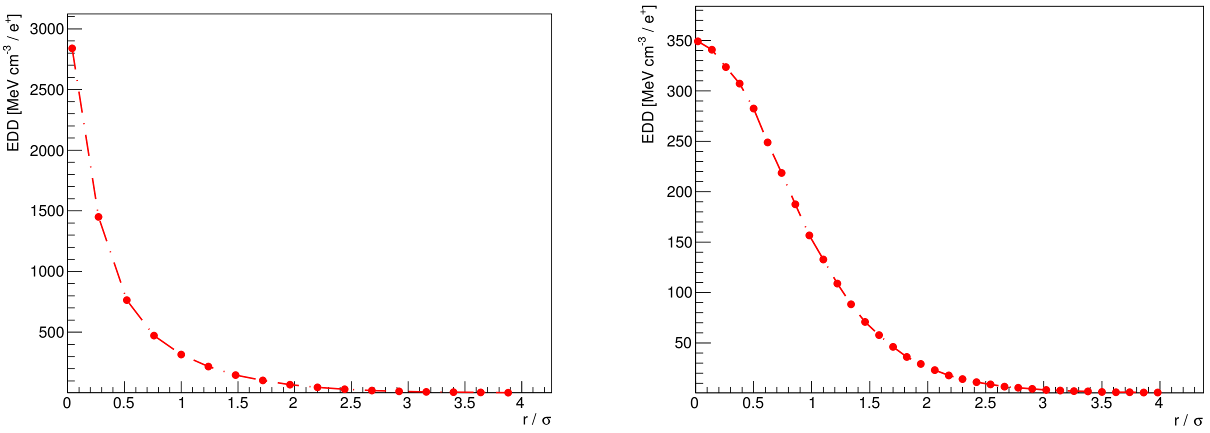

(a) (b)

**Figure 3.28:** Comparison between the EDD along $r$-direction ($z$ is fixed on the last slice of the mesh) for two different spot sizes of the photon beam, $\sigma = 2.016$ mm (a) and $\sigma = 3.373$ mm (b). On the abscissa, the distance from the center normalized to the beam spot size is plotted.

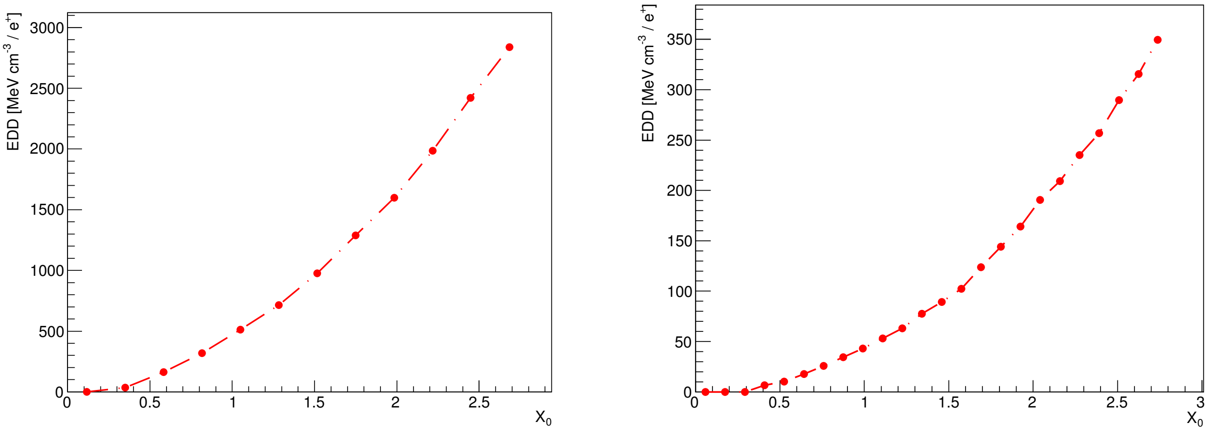

(a)

(b)

**Figure 3.29:** Comparison of the EDD is the $z$-direction for two different spot sizes of the photon beam, 2.016 mm (a) and 3.373 mm (b). Only the cylinders at the center of the mesh are considered, hence the radial position is fixed.

### 3.7.2 Positrons embedded source

The deposited power as a function of $X_0$, for a positrons embedded source is shown in Figure 3.30(a). Values are obtained as in the previous case by introducing a mesh in the target and evaluating the cumulative along z. The tungsten target is positioned at a distance of 1 m from the Beryllium target line. A positron beam with a rate of $5 \cdot 10^{15}\,\mathrm{e}^{+}/\mathrm{s}$ is considered. Here the deposited power is almost ten times larger than in the photon case, as expected, since the full 45 GeV positron beam impinges on the target.

In Figure 3.30(b), the positron yield as a function of the deposited power, for different tungsten thickness (from 0.5 to 2 $X_0$), is figured. In order to recover 100% of the initial beam, one can use a 1.8 $X_0$ tungsten target (with a yield of 1.09 positrons per initial positron). In this case, the deposited power is around 140 kW, hence more power is distributed on a thinner target with respect to the previous case. Consequently, this possibility is technologically more challenging.

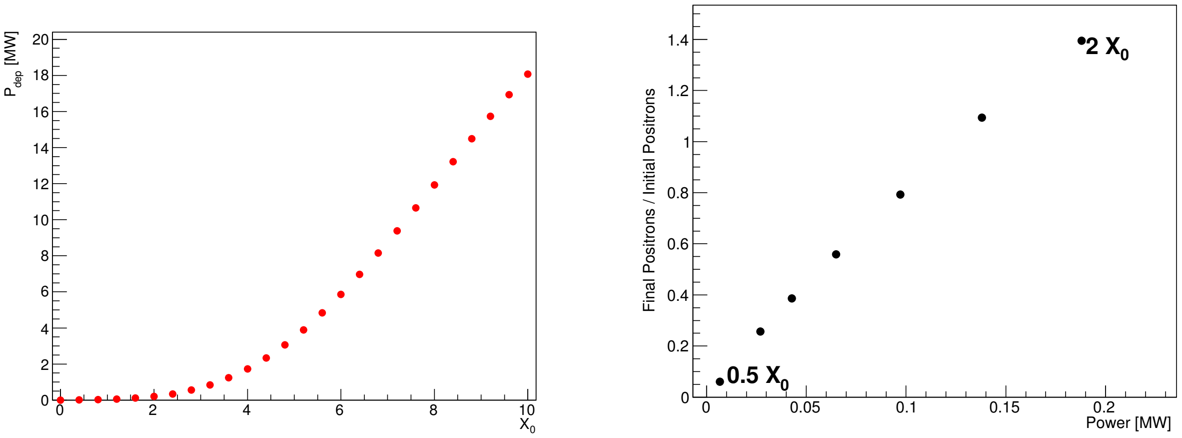

(a) (b)

**Figure 3.30:** (a) Deposited power in tungsten, as a function of the thickness, when the sources are the photon, electron and positron beams. (b) Positron Yield as a function of the deposited power, in the positrons embedded source case.

To locate the regions in which the deposit is larger, the energy deposited in each bin has been recorded as an entry of a 3D histogram. In order to better understand the result, a projection of this histogram in the $x - z$ plane has been done. The result is shown in Figure 3.31.

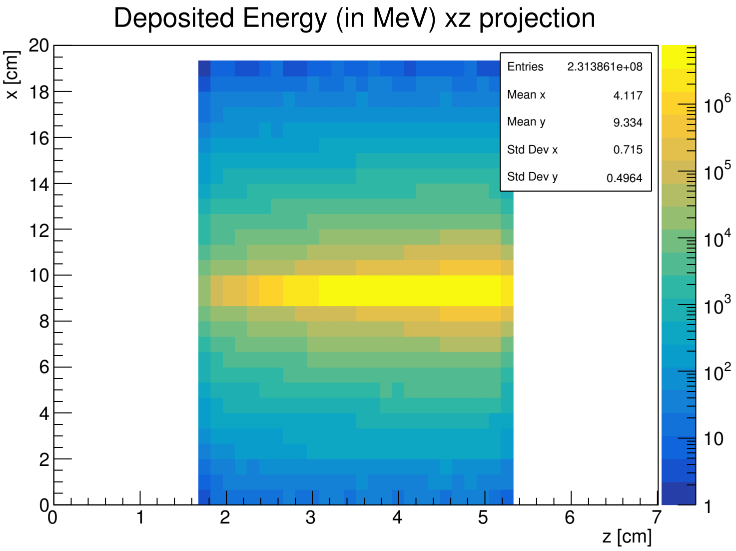

**Figure 3.31:** Projection in the $x - z$ plane of the histogram in which the deposit of energy is recorded. The beam comes from the left.

The increment in energy along the $z$-direction is similar to the previous case.

The PEDD and the positron yield (given by the AND of all selections) as a function of the beam spot size is shown in Figure 3.32. The values of PEDD are normalized to one incident positron. To obtain the final number, this value has to be multiplied by the number of positrons per pulse.

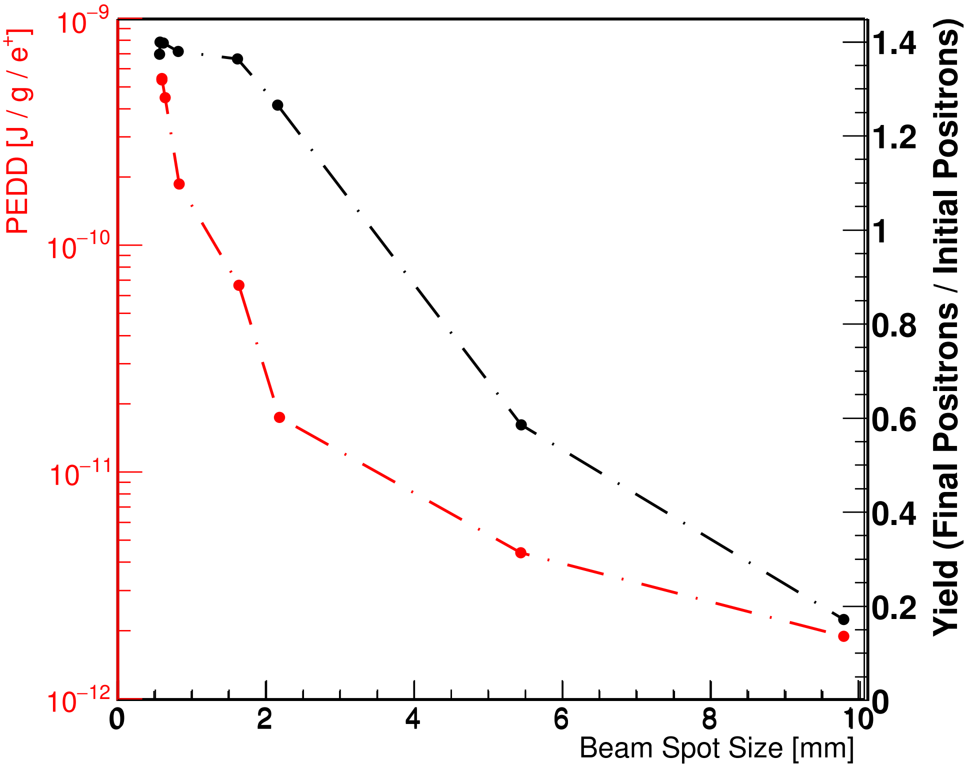

**Figure 3.32:** PEDD and positron yield (given by the AND of all selections) as a function of the beam spot size, in the positron embedded source case, for a 2 $X_0$ tungsten target.

If the number of positrons per pulse is around $10^{12}$, the critical value of 35 J/g is reached for a beam spot size of about 5 mm, and the positron yield is around 0.6. An additional positron source would be necessary in this case.

## 3.8 Bending Dipole

In the previous section, in order to obtain a photons embedded source, positrons and electrons have been manually killed. Here, the operation of a dipole magnet, used to bend away the charged particles before the tungsten target, has been verified.

Of course, this kind of dipoles require some distance to operate. The goal is to introduce a displacement in the primary positron beam greater than 10 cm, that is the radius of the tungsten target (even if smaller radius are also possible). However, similar arguments can be repeated to any displacement.

A representation of this magnet dipole is shown in Figure 3.33. A 1.5 T magnet with a length of 8 m and a lateral dimension (distance between the coils) of 40 cm has been considered. In this case, the distance between the end of the target line and the tungsten is 10 m.

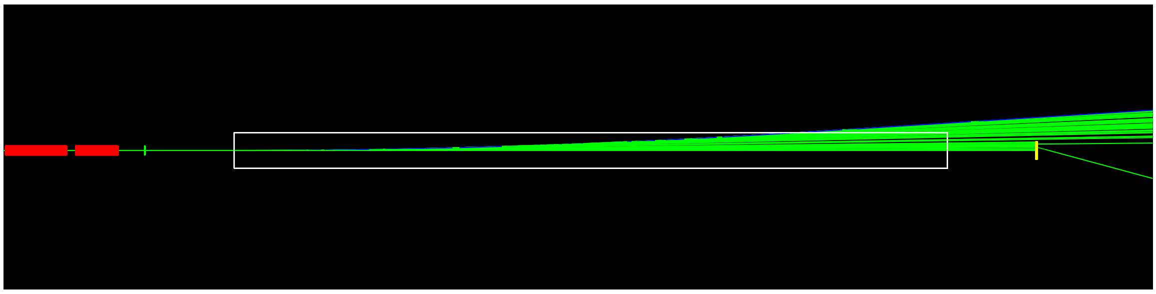

**Figure 3.33:** Magnet dipole in the simulation. In this case, a 8 m long dipole of 1.5 T is introduced. The lateral dimensions are 40 cm x 40 cm.

The positron beam is bent away and does not impinge on the tungsten target. As a result, a great amount of synchrotron radiation is emitted in the forward direction.

The displacement introduced by a dipole is:

$$\Delta x = R(1 - \cos\theta) \simeq R\frac{\theta^2}{2} \tag{3.5}$$

where $R$ is the radius of curvature, $\theta$ is the angle of the curved positron beam with respect to the initial direction, and the approximation is done for small angles.

Then, if $L$ is the length of the dipole, one can write the radius of curvature as:

$$R = \frac{L}{\sin\theta} \simeq \frac{L}{\theta} \tag{3.6}$$

The angle $\theta$ (so the radius of curvature) can be found by the momentum equation:

$$p[\mathrm{GeV}] = 0.3B[\mathrm{T}]R[\mathrm{m}] \rightarrow \sin\theta = \frac{0.3B[\mathrm{T}]L[\mathrm{m}]}{p[\mathrm{GeV}]} \tag{3.7}$$

Numerically, with the values given previously, the displacement after $L$ is:

$$\Delta x = \frac{L}{\sin\theta}(1 - \cos\theta) \simeq 0.32\ \mathrm{m} \tag{3.8}$$

that is large enough.

In order to show that results are similar to those obtained with the killing option (photons embedded source), the analysis of the positron yield has been performed. In 3.34(a), the effect of each cut on the positron yield is shown, while in 3.34(b), the AND of all cuts is figured.

The result is in agreement with the killing option case.

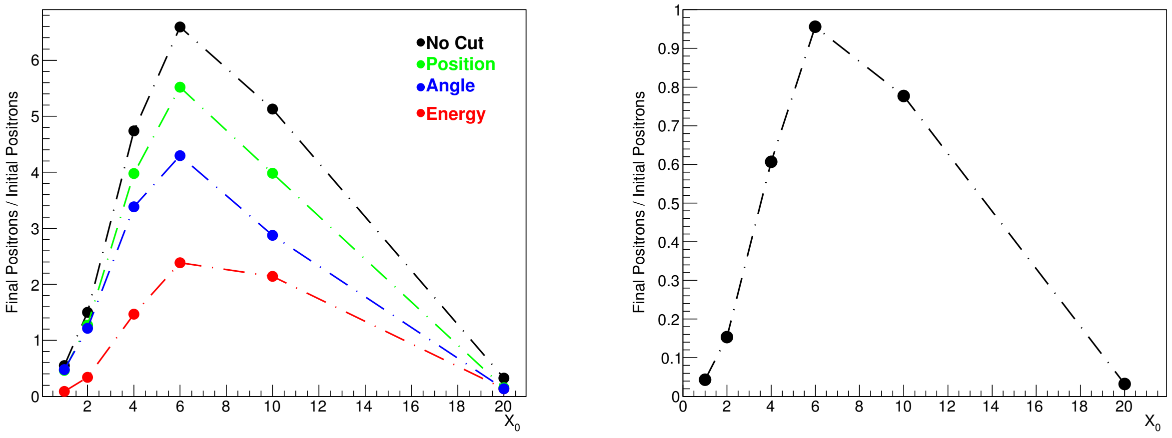

(a) (b)

**Figure 3.34:** Positron yield as a function of the tungsten thickness with a bending dipole to curve charged particles and obtain a photons embedded source. (a) The effect of each cut is shown. (b) The AND of all cuts is shown.

# Chapter 4

# AMD for positron recollection

Solenoids are widely used in capture systems associated with positron sources [31]. In this chapter a short theoretical introduction of this systems, in particular the AMD, is given. Then, in 4.3, results of the introduction of the AMD in the simulation are presented.

Two solutions can be considered: the Quarter Wave Transformer (QWT) and the Adiabatic Matching Device (AMD). The first one is characterized by a magnetic field law as the one presented in Figure 4.1(a). The magnetic field is constant, with a larger value upstream with respect to the beam.

The acceptance of this device depends on the energy of emission of positrons. By varying the magnetic field, the acceptance of the optical system can be made independent from energy, therefore the acceptance increases. This is the aim of systems characterized by an adiabatic magnetic field law, as the one presented in Figure 4.1(b).

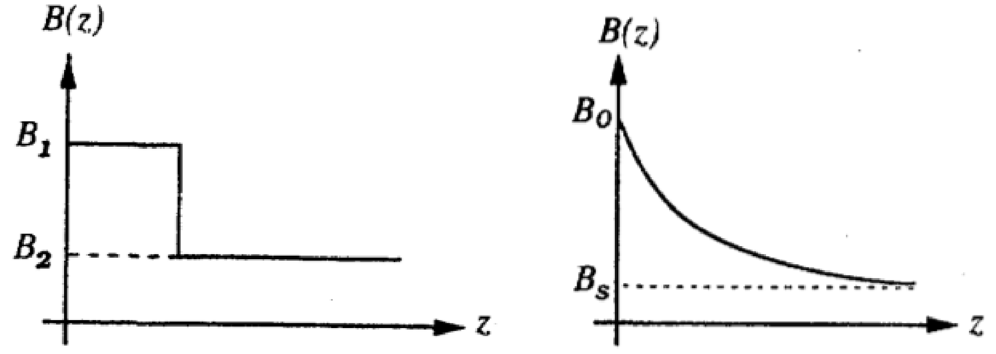

(a) (b)

**Figure 4.1:** (a) Magnetic field law of the quarter wave transformer. (b) Magnetic field law of the adiabatic matching lens.

In practice, an AMD lens is represented in Figure 4.2 on the left. Two ferromagnetic magnets with decreasing thickness are surrounded by coils. The currents circulating in the coils induce a magnetic field with an higher (lower) field density where the distance between the magnets is smaller (larger). In this way a decreasing magnetic field in the $z$ direction is obtained. The final value of the magnetic field matches the value of the solenoid that surrounds the accelerating sections (typically $\sim 0.5$ T).

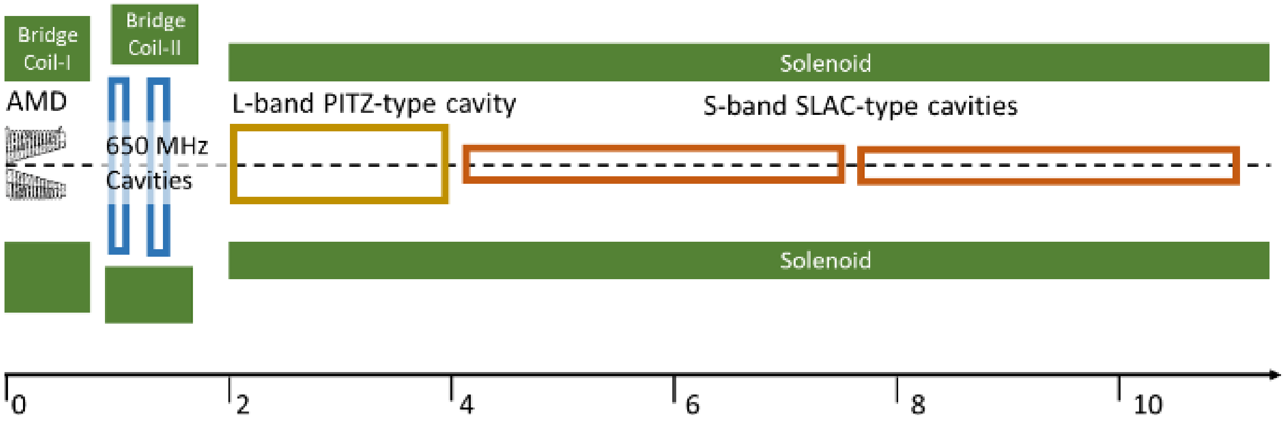

**Figure 4.2:** Representation of a typical capture system. The AMD is the first device on the left.

## 4.1 Dynamics of a particle in a solenoid

Let's consider a reference frame where z is the direction of the electric and magnetic fields in the solenoid. Considering that $\mathbf{B} = \nabla \times \mathbf{A}$, and a uniform magnetic field, the components of the vector potential are: $\mathbf{A} = (-yB/2, xB/2, 0)$.

The Lagrangian of a particle is:

$$L = -m_0c^2\sqrt{1-\frac{v^2}{c^2}} - e(V - \mathbf{A}\cdot\mathbf{v}) \tag{4.1}$$

From Lagrangian equation it follows:

$$\begin{aligned} \frac{d}{dz}p_x &= \frac{eB}{2}\frac{dy}{dz} \\ \frac{d}{dz}p_y &= -\frac{eB}{2}\frac{dx}{dz} \end{aligned} \tag{4.2}$$

where $dz = cdt$.

It is more convenient to handle these equations in a rotating frame having the Larmor frequency, normalized to $c$, equal to $eB/2P$, where P is the scalar momentum. The new variables are then $(\xi, p_\xi; \eta, p_\eta)$. This frame forms with the original one an angle of:

$$\chi(z) = \int_0^z \frac{eB}{2P}dz \tag{4.3}$$

In this new frame, the equations of motion are decoupled and we have with this new system of variables:

$$\begin{aligned} p'_\xi &= \frac{d}{dz}(P\xi') = -\left(\frac{eB}{2}\right)^2\frac{\xi}{P} \\ p'_\eta &= \frac{d}{dz}(P\eta') = -\left(\frac{eB}{2}\right)^2\frac{\eta}{P} \end{aligned} \tag{4.4}$$

For uniform $B$, these equations are those of a simple harmonic oscillator of frequency $eB/2P$.

## 4.2 Acceptance of the AMD system

The Adiabatic Machine Device uses a slowly varying magnetic field followed by a long solenoidal magnetic field extending over some accelerator sections. Between the maximum field ($B_0$) and the minimum ($B_s$) the magnetic field tapers adiabatically. This means that the adiabatic invariant:

$$\oint \sum_i p_i dq_i = \frac{\pi p_\perp^2}{eB} \tag{4.5}$$

where $p_i$ and $q_i$ are the canonical variables and $p_\perp$ the transverse momentum, is conserved.

The equation of motion in the rotating frame are integrated using the WKBJ approximation, where the small parameter is, in absence of an accelerating electric field:

$$\epsilon = \frac{P_0}{eB^2}\frac{dB}{dz} \tag{4.6}$$

which must be much smaller than unity to ensure adiabaticity. The magnetic field law is given by:

$$B = \frac{B_0}{1+\alpha z} \tag{4.7}$$

where $\alpha = \frac{eB_0}{P_0}$ and $P_0$ is the central momentum value.

The maximum accepted source radius, or the radial acceptance, can be obtained by requiring that the integration in the full volume phase space makes sense [32], and it is:

$$R_0 = \sqrt{\frac{B_s}{B_0}}a \tag{4.8}$$

where a is the radius of the iris of the accelerating sections.

The maximum transverse momentum is:

$$p_{\perp,\max} = e\sqrt{B_0 B_s}a \tag{4.9}$$

and hence the angular acceptance is given by:

$$\theta_{\max} = \frac{p_{\perp,\max}}{P_0} = e\frac{\sqrt{B_0 B_s}}{P_0}a \tag{4.10}$$

The acceptance volume (in the 4D transverse phase space) of the adiabatic system is given by [32]:

$$\theta = \frac{2\pi^2}{3}\left(\frac{eB_s a^2}{2}\right)^2 \tag{4.11}$$

and it is independent from the particle momentum. However, the energy acceptance is limited inferiorly by the phase displacement introduced by the solenoid, that is:

$$\delta\phi = \frac{2\pi}{\lambda}\delta L \tag{4.12}$$

where $\lambda$ is the RF wave length and $\delta L$ the path displacement introduced by the solenoid, which is proportional to the maximum angle at the solenoid entrance [32]. This limits the initial momentum, and hence the energy, to be greater than abut 5 MeV. The energy acceptance is also limited superiorly by the violation of the adiabaticity. Generally, the parameter of smallness should not exceed 0.5. This leads to a maximum energy of about 20 MeV.

## 4.3 Positrons Capture System

In this section, the results of the introduction of a simple positrons capture system in the simulation are described. The tungsten target is inserted around the peak field of a solenoid with an adiabatic magnetic field law (see Chapter 4) reconstructed in Figure 4.3 and described analitically by (4.7). The magnetic field is decreased adiabatically from $B_0 = 5T$ (peak field) to $B_S = 0.5$ T (field of the solenoid of the accelerating sections that follow the AMD). The geometry is shown in Figure 3.4(c) and in Figure 4.4. The parameter of the tungsten target, in this section, are the following: thickness $= 2.8\, X_0$, $zGap = 1$ m (distance from the target line), $R = 0.4$ cm (radius of the target), and the photons embedded source case is considered. The expected positron yield (given by the AND of all selections) is 0.32 in this case.

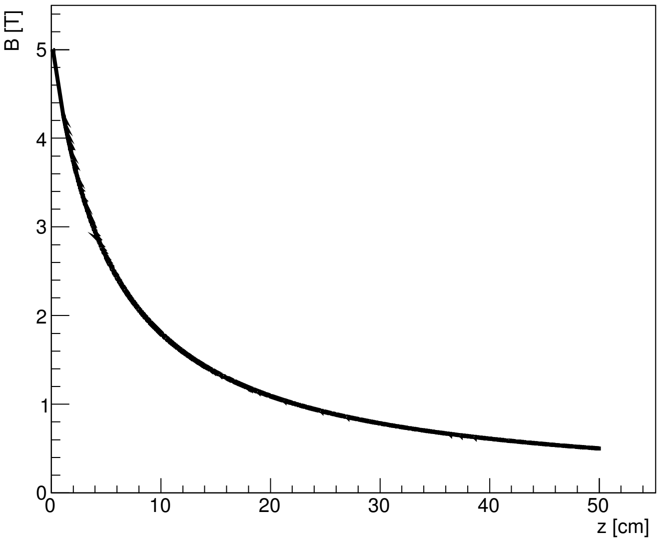

**Figure 4.3:** (a) Magnetic field law of the AMD used in the simulation.

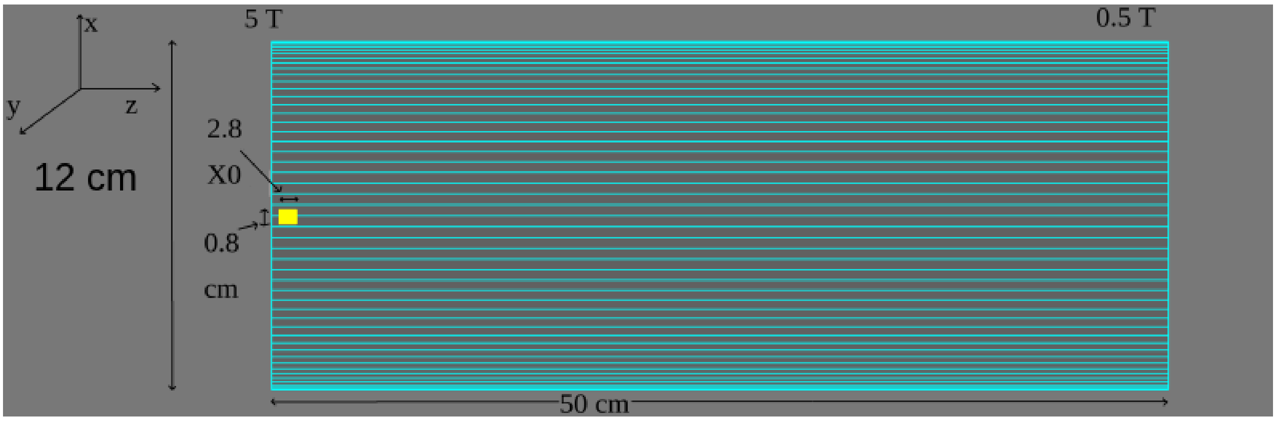

**Figure 4.4:** Geometry of the AMD solenoid with dimensions.

The main goal of this device, as explained in Section 3.6, is to apply a transformation in the transverse phase space ($x$, $p_x$) (and the same in the $y$ direction), in order to better match the acceptance requirements of the accelerating capture sections, which have a relatively large radial extent but smaller transverse momentum acceptance.

So the radial extent of the beam is increased after the AMD, while its angular amplitude (or the transverse momentum) is decreased.

Let us start by considering the phase space transformation in the case with no magnetic field. At the beginning of the solenoid the phase space position-angle (with $\theta_x = \tan^{-1}(p_x/p_z)$) is the one presented in Figure 4.5(a). Positrons are emitted at any angle, while the radial dimension of the phase space is determined by the radial extent of the tungsten target (in the figure, 4 mm).

In the case of “free transport”, the positrons with a large and positive emission angle will have, after 50 cm (the length of the “switched-off” solenoid), the same angle (because are not deviated in vacuum) but a larger distance from the $z$-axis. The same happens for negative emission angle positrons in the opposite direction, while the positrons with a low emission angle remains around the $z$-axis. This result is well described in Figure 4.5(b), which represents the phase space of the beam that intercepts the end of the solenoid after 50 cm. More than one half of the produced positrons are lost in the lateral directions for angular and position acceptance.

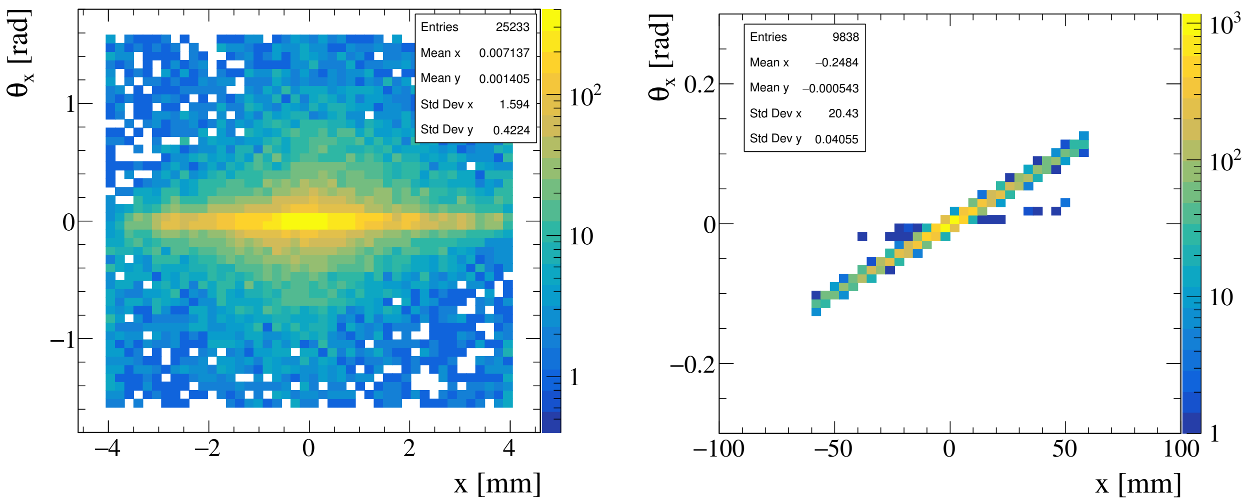

(a)

(b)

**Figure 4.5:** (a) Position-angle phase space of the positron beam at the solenoid entry, with no magnetic field ($B_0 = 0$). (b) Position-angle phase space of the positron beam at the solenoid exit, with no magnetic field ($B_0 = 0$). The phase space transformation from the previous figure is the result of a “free transport”.

The phase space represented in Figure 4.5(b) is, of course, not well matched with the acceptance of an accelerating section.

With the presence of the magnetic field, the output phase space is transformed as presented in Figure 4.6(a) and Figure 4.6(b), respectively with a peak field $B_0$ equal to 5 T or 8 T (same $B_S = 0.5$ T in both cases). The transformation is more convenient, since much more positrons reach the end of the solenoid, and the population in the center of the phase space is higher. This leads to better emittance and better performances in positrons capture. The “free transport” effect is mitigated, since positrons are obliged to spiralize around the $z$-axis. As a result of the phase space transformation, the angular spread is lower with respect to the solenoid entry (see Figure 4.5(a)), while the position spread is larger. The difference between $B_0 = 5$ T and

$B_0 = 8$ T is minimal.

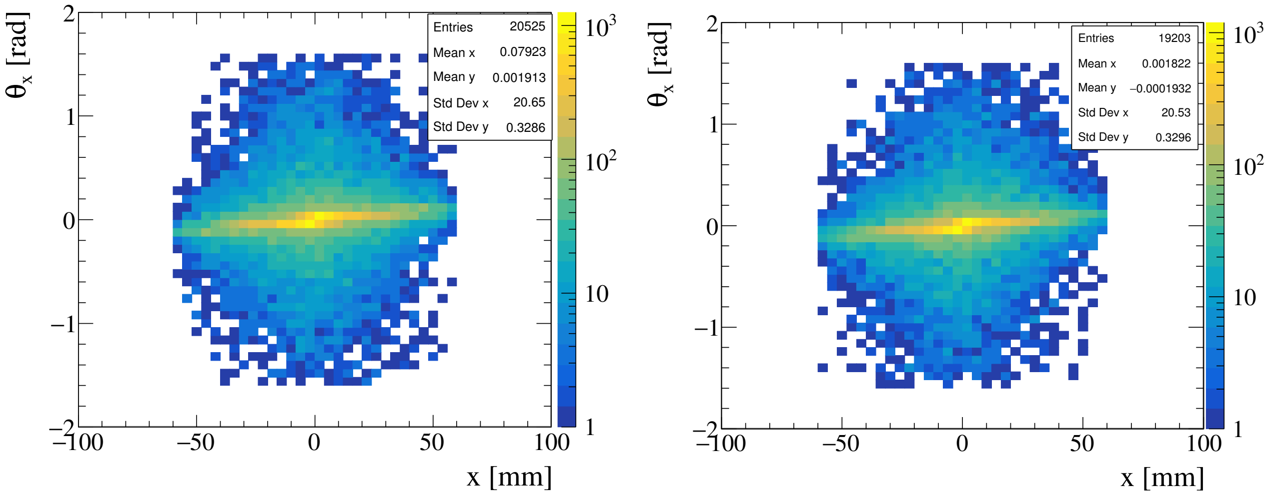

(a) (b)

**Figure 4.6:** (a)Position-angle phase space of the positron beam at the solenoid exit, with $B_0 = 5$ T. (b)Position-angle phase space of the positron beam at the solenoid's exit, with $B_0 = 8$ T. The solenoid length is $l = 50$ cm. As a result of the phase space transformation, the angular spread is lower with respect to the solenoid entry, while the position spread is larger.

Different geometric configurations have been tested. The output phase space for a solenoid with $l = 30$ cm (longitudinal length) is shown in Figure 4.7(a). The number of positrons is a little smaller with respect to Figure 4.6(b), but also the emittance is lower (both position and angular spread). In Figure 4.7(b), the trajectory of a positron with initial energy $\sim 16$ MeV is shown. By geometric construction, the radius of curvature at a given position and magnetic field can be evaluated, in order to obtain a measurement of the transverse momentum (by (1.23)) and to verify the magnet operation. This has be done in an approximated way (since the magnetic field varies along $z$, average values have been considered), and the transverse momentum at solenoid's entry and exit are, for the positron in Figure 4.7(b), respectively, 2.73 MeV and 2.70 MeV. The two numbers are quite in agreement, confirming the fact that the magnetic field varies only the direction of the transverse momentum, not the module. Moreover, the radius of curvature increases from the tungsten target to the solenoid exit, due to the reduction of the magnetic field.

After the solenoid, a cylindrical box is used to simulate the geometrical acceptance of the RF accelerating section (the electromagnetic field inside is not simulated). The radius has been set at 1.5 cm (a typical value of an S-band accelerating cavity [14]).

The position-angle phase space at the entrance of this "RF box" are shown in Figure 4.8(a) and Figure 4.8(b), respectively for $B_0 = 5$ T and $B_0 = 8$ T ($B_S = 0.5$).

Two different geometric configurations are presented in Figure 4.9(a) and Figure 4.9(b). In the first one, the length of the solenoid is decreased ($B_0 = 8$ T, $B_S = 0.5$ T and $l = 30$ cm). In the second one, the magnetic field of the solenoid is increased ($B_0 = 8$ T, $B_S = 0.8$ T and $l = 50$ cm). The positron yield increases in both situations, in fact the number of entries (normalized to $10^4$ initial positrons) is higher than in the previous cases.

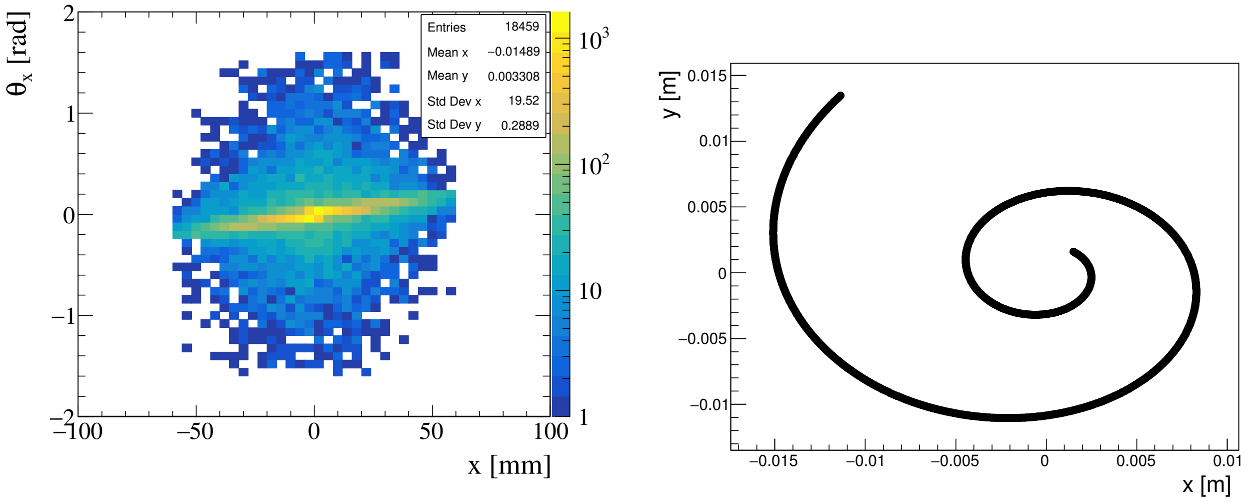

(a) (b)

**Figure 4.7:** (a)Position-angle phase space of the positron beam at the solenoid exit, with $B_0 = 8$ T and $l = 30$ cm. (b) Trajectory of a positron with initial energy of about 16 MeV (x-y projection). The radius of curvature increases from the tungsten target to the solenoid exit (the positron follows a clockwise rotation in the transverse plane), due to the decrease of the magnetic field along $z$.

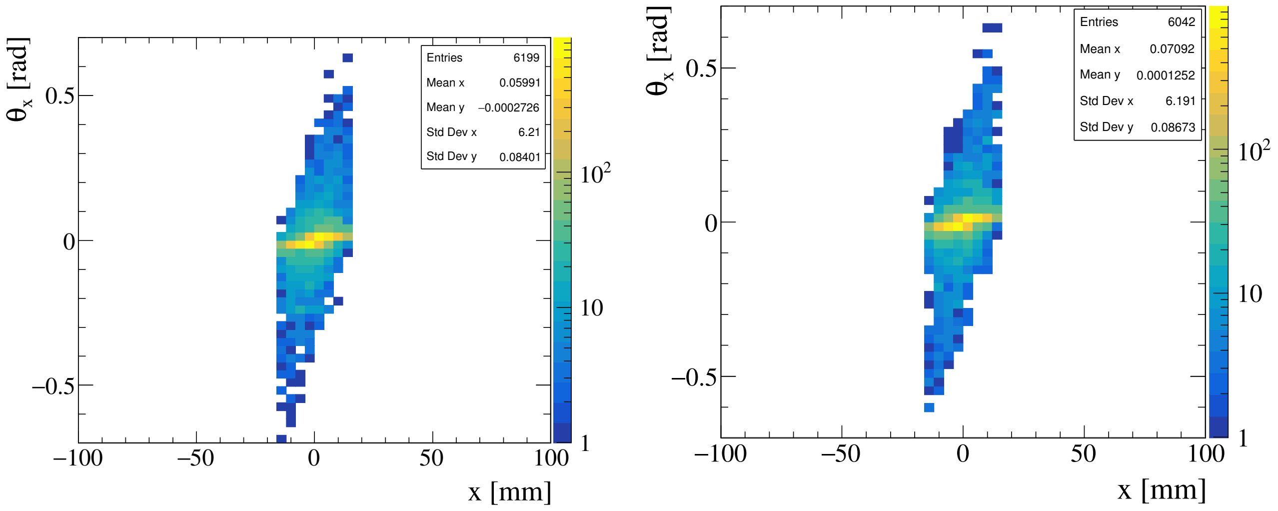

(a) (b)

**Figure 4.8:** (a)Position-angle phase space of the positron beam at the entrance of the RF box, with $B_0 = 5$ T, $B_S = 0.5$ T and $l = 50$ cm. (b)Position-angle phase space of the positron beam at the entrance of the RF box, with $B_0 = 8$ T, $B_S = 0.5$ T and $l = 50$ cm.

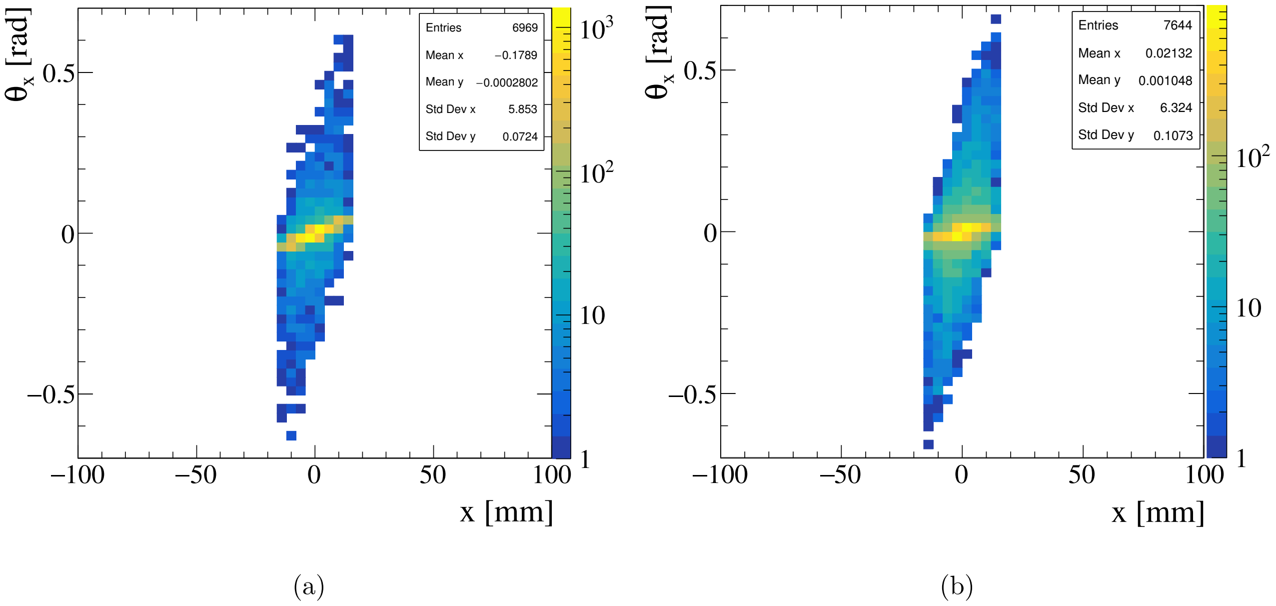

**Figure 4.9:** (a)Position-angle phase space of the positron beam at the entrance of the RF box, with $B_0 = 8$ T, $B_S = 0.5$ T and $l = 30$ cm. (b)Position-angle phase space of the positron beam at the entrance of the RF box, with $B_0 = 8$ T, $B_S = 0.8$ T and $l = 50$ cm.

In order to compare the results given in the previous chapter for the positron yield, when the selections on energy, angle and position have been used, with the number of positrons captured by the AMD and entering in the RF box, a selection on energy is needed (the geometric selection is given by the iris of the accelerating section, i.e. the RF box itself). Typically, as discussed in Section 4.2, positrons with energy between 5 and 20 MeV can be collected by accelerating capture system (consisting of RF sections immersed in a solenoid with a constant magnetic field equal to $B_S$ of the AMD). However, with a convenient synchronization of the accelerating field to reduce the phase spread (see Section 3.6) the maximum energy of the captured positrons can be increased, for instance up to 30 MeV.

Therefore a result for the positron yield can be given by the energy distribution of positrons entering in the RF box in a given range of energy. Figure 4.10(a) and Figure 4.10(b) present the results for $B_0 = 5$ T, $B_S = 0.5$ T and $l = 50$ cm. The positron yield, normalized to the initial number of positrons ($10^4$) is respectively 0.09 and 0.12, that is about 30-40 % with respect to the “theoretical” value (without capture system in the simulation) of 0.32. With the best configuration, that is $B_0 = 8$ T, $B_S = 0.8$ T and $l = 50$ cm, the yield of positrons between 5 and 20 MeV is increased to 0.15, while between 5 and 30 MeV it is 0.2 (captured positrons per initial positron).

Hence, in a future study, an optimization of the AMD parameters, as well as an improvement of the technical parameters of the capture system (e.g. the solenoidal field $B_S$), can be done to further increase the positron yield.

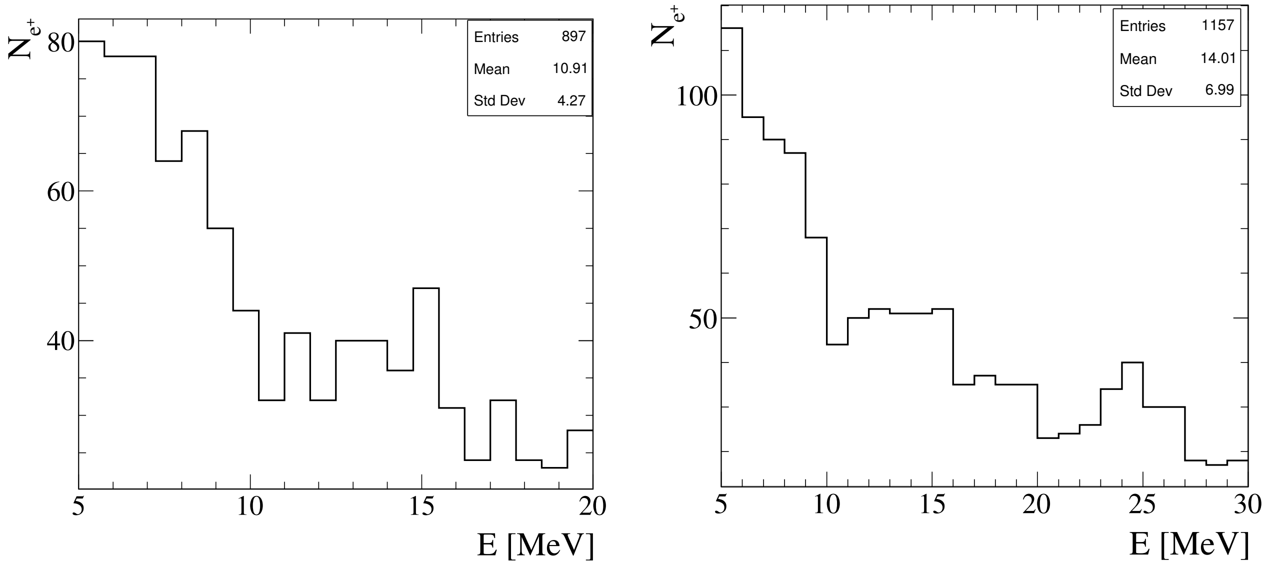

(a) (b)

**Figure 4.10:** (a) Energy distribution of positrons between 5 and 20 MeV entering in the RF box. (b) Energy distribution of positrons between 5 and 30 MeV entering in the RF box. The positron yield, that is the number of positrons collected by the capture system, is given by normalizing the entries of the histograms to the number of initial positrons ($10^4$). This number can be compared to the results discussed in Section 3.6.

# Chapter 5

# Conclusions

A muon collider is one of the promising possibilities for a future circular collider for the next decades. Its characteristics (in particular the point-like nature of muons and their significant mass) make it interesting in addition or in substitution to the classical scheme $e^+e^-$ and $pp$ colliders, mainly operated at CERN in the last half century. This project is just at the beginning, and this study must also be seen, together with many others, as an effort to sustain and enhance the interest in muon colliders, in particular for the positron based scheme.

The main aspects discussed in this study, the positron production, the use of a muon target line to produce low-emittance muons, the possibility of regenerating and sustaining the positron beam for its full operation cycle through an heavy target and a capture system, represent some of the principal aspects to work on in order to realize a positron based muon collider.

The main results of this study concern the characteristics of the tungsten target used to regenerate the positron beam with a convenient positron yield and a sustainable deposited power, and can be useful for any following study in this field.

After the analysis of the tungsten parameters (see Chapter 3), an optimal configuration has been found, and it is presented in this conclusive chapter. Also the tungsten radius has been considered as a parameter, after the optimization of all the others. The reason is the following. At very small radii high-energy charged particles and photons escape from the sides of the wire, precluding the development of a substantial electromagnetic cascade and hence a large positron yield. At large radii the shower reaches maximum development, but many of the low-energy positrons are reabsorbed before reaching the downstream edge of the target. Also in this case the positron yield is reduced [24]. Hence an optimal radius exists. This behaviour is summarized in Figure 5.1(a) and Figure 5.1(b), which show respectively the positron yield and the deposited power as a function of the radius of the tungsten target.

The procedure to find this optimal configuration has been the following:

1. First of all, a 10 cm radius (much larger than the beam spot size) of the tungsten target is considered. In order to reduce the total deposited power, the minimal thickness which satisfies the requested yield is found (see Section 3.6).
2. The distance between the final Beryllium target and the Tungsten target is increased in order to reduce the PEDD (see Section 3.7). The deposited power and the positron yield are not strongly affected by this variation (the positron yield up to a distance of the order of 10 m).

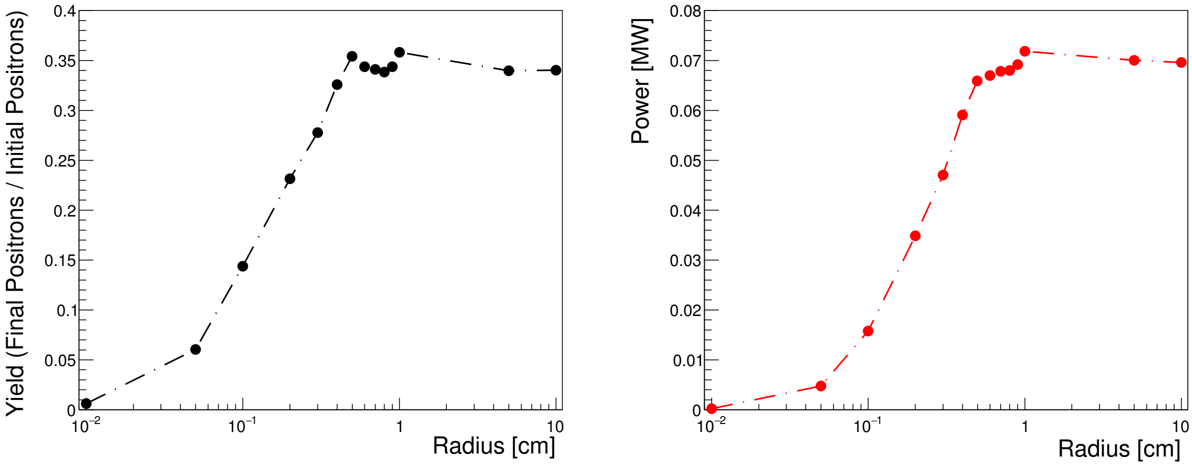

(a) (b)

**Figure 5.1:** Positron yield (a) and deposited power (b) as a function of the radius of the tungsten target, for fixed distance (1 m) and thickness (2.8 $X_0$). At very small wire radii high-energy charged particles and photons escape from the sides of the wire, precluding the development of a substantial electromagnetic cascade and hence a large positron yield. At large wire radii the shower reaches maximum development, but many of the low-energy positrons are reabsorbed before reaching the downstream edge of the target, causing a reduction of the yield.

3. The radius is decreased until an optimal yield is reached. A small reduction of the total deposited power is also obtained. The PEDD is evaluated in the same way (see Section 3.7) and it is not strongly affected by this variation.

Two optimal configurations, respectively for the photons and positrons embedded source, are proposed and summarized in Table 5.1.

**Table 5.1:** Summary table that shows two optimal configurations for the photons and positrons embedded source, obtained with the process described in the text.

| | Thickness [$X_0$] | Radius [cm] | zGap [m] | Yield | Power [kW] | PEDD [ J/g/e$^+$] |
|---|---|---|---|---|---|---|
| Photons | 3 | 0.5 | 20 | 0.30 | 58.6 | 3.06 e-12 |
| Positrons | 2 | 0.35 | 20 | 1.06 | 129.4 | 1.75 e-11 |

Concerning PEDD, due to the critical energy density of about 35 J/g (see Section 3.7), the values presented in the table put a limit on the number of positrons per pulse ($\sim 10^{12}$ e$^+$ in the photons case and $\sim 2 \cdot 10^{11}$ e$^+$ in the positrons case).

In the event that these values represent an excessive load on the target, and the number of positrons cannot be decreased without reducing the luminosity constraints, the simplest option could be to reduce the tungsten thickness and satisfy the yield constraint with a second positron source.

In this thesis work, the Geant4 simulation of the target line that LEMMA experiment has proposed has been updated and extended. The possibility of considering and managing different target lines (that can be imported starting directly from the optics file via a *.gdml* file), the positron regeneration option (with the possibility of introducing a scoring mesh) and a basic capture system make it very flexible and suitable for many future studies.

In particular, the following proposals can be the "next step":

- Experimental test beam on Beryllium targets (1) (in particular to prove the division of the deposited power on different targets).
- Comparison of the AMD results with the positron collection efficiency simulation performed with ASTRA-GIOTTO code (see [14]) or implementation of a full capture system with Geant4.

---

(1) INFN Roma 1 is recently considering this possibility.

# Bibliography

[1] J.P.Delahaye *et al.*, *Muon Colliders*, arXiv:1901.06150v1, 2019.

[2] A. Wulzer, *Obvious physics at the muon collider*, indico.cern.ch/talk_wulzer.pdf, 2019.

[3] J.M.Campbell, J.W.Huston, W.J.Stirling, *Hard Interactions of Quarks and Gluons: a Primer for LHC Physics*, Rept.Prog.Phys. 70 (2007) 89.

[4] Richard Talman, *Scaling Behaviour of circular colliders dominated by synchrotron radiation*, arXiv:1504.01627, 2015.

[5] J.D. Jackson, *Classical Electrodynamics*, Third Edition, Eq. (14.81), John Wiley, 1998.

[6] https://www.lhc-closer.es/taking_a_closer_look_at_lhc/1.physics_at_lhc.

[7] J Rossbach and P Schmüser, *Basic course on accelerator optics*, In: DESY-M-93-02 (Feb. 1993), p. 72, https://cds.cern.ch/record/247501.

[8] E. Segrè, *Nuclei and Particles - An introduction to nuclear and subnuclear physics*, Zanichelli, 1977.

[9] F. Tecker, *Longitudinal beam dynamics in circular accelerators*, CERN, https://cas.web.cern.ch/sites/cas.web.cern.ch/files/lectures/budapest-2016/tecker.pdf, 2016.

[10] C. Biscari, *Transverse Beam Dynamics*, Accelerator Physics UAB, https://indico.cern.ch/event/528094/Transverse_Beam_Dynamics.pdf, 2014

[11] J. Buon, *Beam phase space and emittance*, 1992.

[12] Y.Torun et al., *The US Muon Accelerator Program*, Proceedings of IPAC'10, Kyoto, Japan, hrefhttp://accelconf.web.cern.ch/AccelConf/IPAC10/papers/wepe065.pdfhttp://accelconf.web.cern.c 2010.

[13] The Mice Collaboration, *Design and expected performance of the MICE demonstration of ionization cooling*, arXiv:1701.06403, 2017.

[14] The LEMMA Collaboration, *Positron driven muon source for a muon collider*, arXiv:1905.05747, 2019.

[15] D. Stratakis, D. V. Neuffer, *Compact Muon Production and Collection Scheme for High-Energy Physics Experiments*, https://arxiv.org/pdf/1504.00380.pdf, 2014.

[16] M. Uchida, *The MICE Muon Ionization Cooling Experiment*, http://accelconf.web.cern.ch/AccelConf/cool2017/talks/moa12_talk.pdf, Imperial College London, 2017.

[17] D. M. Kaplan, *Muon cooling, Muon colliders and the MICE experiment*, https://arxiv.org/pdf/1307.3891.pdf, Illinois Institute of Technology, Chicago, USA, 2013.

[18] J.B. Flanz, P.T. Demos, K.D. Jacobs and A. Zolfaghari, *Energy Compression System Design for the MIT-Bates Accelerator Center*, MIT-Bates Accelerator Center, http://accelconf.web.cern.ch/Accelconf/p91/PDF/PAC1991_0601.PDF, 1991.

[19] R. Hajima, *Energy Recovery Linacs for light sources*, https://www.researchgate.net, Reviews of Accelerator Science and Technology, 2010.

[20] A. Variola, *Advanced positron sources*, Nuclear Instruments and Methods in Physics Research A 740, 21–26, 2014.

[21] J.A. Clarke et al., *The design of the positron source for the International Linear Collider*, http://accelconf.web.cern.ch/AccelConf/e08/papers/weobg03.pdf, 2008.

[22] C. Adolphsen et al, *The International Linear Collider, Technical Design Report*, Vol.3.II: Accelerator Baseline Design, ISBN 978-3-935702-77-5, (2013).

[23] M. Aicheler et al , *CLIC Conceptual Design Report: A MultiTeV Linear Collider Based on CLIC Technology*, CERN-2012-007, (2012).

[24] M. James, R. Donahue, R. Miller and W.R. Nelson, *A new target design and capture strategy for high-yield positron production in electron linear colliders*, SLAC PUB 5215, 1990.

[25] B. Rossi, *High Energy Particles*, Prentice-Hall, Inc., Englewood Cliffs, NJ, 1952.

[26] J.H. Hubbel, *Photon cross sections, attenuation coefficients, and energy absorption coefficients from 10 keV to 100 GeV.*, U.S Department of Commerce, 1969.

[27] V. Bharadwaj, Y. Batygin and J. Sheppard et al., *Analysis of Beam-Induced Damage to the SLC Positron Production Target*, SLAC-PUB-9438, 2002.

[28] S. Maloy, et al., *SLC Target Analysis*, LANL LA-UR -01-1913, June 2001.

[29] X.Artru, R.Chehab, M.Chevallier, and V.Strakhovenko, *Advantages of axially aligned crystals used in positron production at future linear colliders*, arxiv.org:0307004v2, 2003.

[30] L. Zang, T. Kamitani, *SuperKEKB positron source target protection scheme*, researchgate.276919799

[31] R. Chehab, *Angular Collection using Solenoids*, 1999.

[32] R. Chehab, *Etude de la production et du confinement d'un faisceau de positrons. Application à l'accélérateur linéaire d'Orsay.*, thesis presented at l'Universite de Paris-Sud, 1975.